

Sea Surface Salinity Variability and Underlying Mechanisms

An analysis and interpretation of satellite data

by
Julia Köhler

Dissertation with the aim of achieving a doctoral degree
at the Faculty of Mathematics, Informatics and Natural Sciences
Department of Earth Science
of the University of Hamburg
November 2015

Dissertation accepted by the
Department of Earth Science, University of Hamburg
under the Exam committee of:
Prof. Dr. Detlef Stammer
Prof. Dr. Detlef Quadfasel

Hamburg, 19 January 2016

Corrected version

Statutory Declaration

I hereby declare that I have written the present thesis on my own without any external unauthorised help. I agree that a copy of this thesis may be made available in the library of the University of Hamburg.

Hamburg, October 29, 2015

Julia Köhler

Zusammenfassung

In dieser Arbeit wird eine detaillierte Analyse des Oberflächensalzgehaltes (Sea Surface Salinity, SSS) der Fernerkundungssatellitenmission SMOS (Soil Moisture and Ocean Salinity) der Europäischen Weltraumagentur ESA vorgestellt. Der Sensor ist das erste passive Mikrowellenradiometer das im L-Band, bei einer Frequenz von 1.4 GHz, misst. Die im L-Band gemessene Strahlung enthält Informationen über den Oberflächensalzgehalt des Ozeans. Die Genauigkeit der Salzgehaltsbestimmung hängt von diversen Faktoren wie beispielsweise der radiometrischen Genauigkeit, der Oberflächenrauigkeit oder auch der Oberflächentemperatur ab.

Satellitenbasierte Oberflächensalzgehalte werden mit *in situ* gemessenen und simulierten Salzgehalten global und regional verglichen. SMOS BEC L4 SSS zeigen einen negativen Bias bis zu -2 für Oberflächentemperaturen (Sea Surface Temperature, SST) unter 5°C. Mittels einer temperaturabhängigen Korrektur kann der Bias stark reduziert werden. Die Variabilität der korrigierten SSS-Daten zeigt ähnliche räumliche Muster wie Modellsimulationen und *in situ* Messungen. In Regionen mit einer höheren Temperatur können die Oberflächensalzgehalte auf Variabilitäten in niedrigen (zwischen den Jahren) bis hin zum hohen (intrasaisonal) Frequenzbereich untersucht werden. Die niederfrequente SSS-Variabilität wird durch die Kombination von Argo Float Daten mit Satelliten-SSS-Daten auf die zugrundeliegenden physikalischen Prozesse untersucht. Diese Untersuchung zeigt, dass während des negativen Indischen Ozean Dipols (N-IOD) horizontale Advektion und vertikaler Auftrieb positive SSS-Anomalien im zentralen Indischen Ozean verursachen. Dagegen bewirkt vermehrter Niederschlag die negativen SSS-Anomalien vor der Küste Sumatras und Javas. Während des positiven Indischen Ozean Dipols (P-IOD) können negative SSS-Anomalien in zentralen Indischen Ozean und positive Anomalien vor Sumatra und Java beobachtet werden, die auf Advektion, aber vor allem auf Verdunstung und Niederschlag zurückzuführen sind. Im Jahr 2012 kann ein ausgeprägter SST-Dipol beobachtet werden, der aber später als normal einsetzt und sich früher auflöst. Dieser Dipol ist weniger deutlich in der SSS-Dynamik ausgeprägt.

Wavelet-Analysen zeigen, dass intrasaisonale Variabilitäten das IOD-Verhalten im zentralen Indischen Ozean modulieren. Die Entwicklung des P-IOD wird durch die Madden-Julian Oszillation (MJO) verzögert. Während N-IOD-Phasen wird die MJO-Aktivität verstärkt.

Neben der erstmaligen Validierung sowie der Entwicklung einer SST-abhängigen Korrektur

von satellitenbasierten SSS-Daten in den hohen nördlichen Breiten, zeigt diese Studie zum ersten Mal die Entwicklung von IOD-Ereignissen unter dem Einfluss von MJO-Aktivitäten unter Verwendung satellitenbasierter SSS-Daten.

Abstract

A detailed assessment of spaceborne sea surface salinity (SSS) data by the European Space Agency's Soil Moisture and Ocean Salinity (SMOS) mission is presented. Satellite-retrieved SSS are compared with *in situ* and model salinities on global and regional scale. In cold waters, SMOS BEC L4 SSS show a sea surface temperature (SST)-dependent negative SSS bias up to -2 for temperatures below 5°C. The bias can be substantially reduced by an SST-dependent bias correction. Retrieved spatial structures of SSS variability after correction are in good agreement with *in situ* observations and model simulations. In warm waters, it is possible to analyze satellite-retrieved SSS variabilities from low- to high-frequencies (year-to-year variabilities to intraseasonal variabilities). The low-frequency SSS variability is examined by combining Argo float data with satellite-retrieved SSS to favor the identification of forcing terms during the Indian Ocean Dipole (IOD) events in 2010 and 2012. Oceanic advection and subsurface processes are important in generating and buoying the positive SSS anomalies in the central Indian Ocean during the strong negative IOD (N-IOD) event in 2010, whereas evaporation minus precipitation patterns contribute most to the negative SSS anomalies close to Sumatra and Java. Contrary conditions are observed during the moderate positive IOD (P-IOD) in 2012. A strong SST-dipole was observed in 2012, but not pronounced in the salinity budget terms. Wavelet analyses show that intraseasonal variabilities modulate the IOD behavior in the central Indian Ocean. The development of the P-IOD is inhibited due to Madden-Julian Oscillation (MJO) activities, whereas the MJO activity is strengthened during the N-IOD, indicating an interaction between both modes.

Beside the first-time validation of satellite-retrieved SSS data obtained in high northern latitudes and the development of a SST-dependent correction method, this study shows for the first time the development of IOD events under the influence of MJO events using satellite-retrieved SSS data.

Contents

Zusammenfassung	i
Abstract	iii
1 Introduction	1
1.1 Background	1
1.2 Motivation	5
1.3 Outline	8
2 Data and methodology	9
2.1 Salinity remote sensing	9
2.1.1 SMOS mission	13
2.1.2 Aquarius mission	17
2.2 Ship-based thermosalinograph data	19
2.3 Argo float data	20
2.4 World Ocean Atlas	21
2.5 General circulation models	22
2.5.1 MITgcm/Eddy-resolving model	22
2.5.2 STORM model	23
2.6 Auxiliary datasets	23
3 Quality assessment of spaceborne sea surface salinity observations	27
3.1 Validation on global scale	27
3.2 Northern North Atlantic Ocean	32
3.2.1 Bias estimation for SMOS salinity retrievals	35
3.2.2 Processes affecting the differences between satellite and <i>in situ</i> salinities	41
3.2.3 Validation of corrected salinity retrievals against TSG observations .	45
3.2.4 Annual cycle of monthly salinity anomalies	48
3.2.5 Concluding remarks	51

3.3	Indian Ocean	53
3.3.1	Spatial salinity distribution	55
3.3.2	Spatial distribution of salinity variability	57
3.3.3	Validation of satellite salinity retrievals	59
4	Driving mechanisms of seasonal and interannual SSS variability in the Indian Ocean	65
4.1	Salinity variability	65
4.1.1	Annual cycle	66
4.1.2	Interannual variability	69
4.2	Salinity budget analyses	77
4.2.1	Salinity flux anomalies	78
4.2.2	Salinity budget in the tropical Indian Ocean during the Indian Ocean Dipole	82
4.3	Influence of the Madden-Julian Oscillation on SSS dynamics	88
4.3.1	Analysis of variabilities using wavelet transform	95
4.4	Barrier layer dynamics	99
4.5	Concluding remarks	101
5	Summary and Outlook	105
A	Frequency analyses	111
A.1	Fourier transform	111
A.2	Wavelet transform	112
B	Salinity budget in the tropical Indian Ocean during the 4-year period 2010 to 2013	115
	References	119
	List of Figures	131
	List of Tables	133
	List of Abbreviations	135
	Software overview	137
	Acknowledgements	139

Chapter 1

Introduction

1.1 Background

The climate of the Earth changes in response to natural variability as well as increasing concentrations of man-made greenhouse gases and aerosols (*Wu et al., 2013*). Global climate change will intensify the hydrological cycle (*Allen and Ingram, 2002*), affecting atmospheric water vapor concentrations, precipitation patterns and stream flow patterns. A warmer atmosphere can hold more water vapor and, therefore, precipitation increases (*Trenberth et al., 2003*). At the same time more water evaporates and transpires through land surfaces which could lead to longer and more intense droughts (*O’Gorman and Schneider, 2009*). Hence, climate change has been attributed with significant intensification of floods and droughts. These changes will provide great potential impacts on society.

Analyses (*IPCC, 2007*) show that shifts in the hydrological cycle occurred during the past century due to natural variations and anthropogenic influences. *Liu and Allan (2013)* showed that regions dominated by precipitation are expected to become wetter whereas regions with evaporation exceeding precipitation will become drier.

Changes in river runoff as well as the increase of salinity in estuaries and groundwater in coastal areas due to sea level rise may influence the freshwater availability. As mentioned by *Liu and Allan (2013)* changes in the availability of freshwater can strongly affect societies and the ecosystems upon which these depend. Areas that are already vulnerable due to their limited groundwater storage capacity are likely to be further aggravated by poor water management, overuse from increasing population and an increase in water demand (*Parry et al., 2007*).

The global hydrological cycle comprises flux interactions between the atmosphere, the ocean, the cryosphere and the terrestrial components of the Earth's climate system (see Fig. 1.1). The ocean plays a major role in the Earth's hydrological cycle covering more than 70% of the Earth's surface and containing 96% of free water (Yu, 2011).

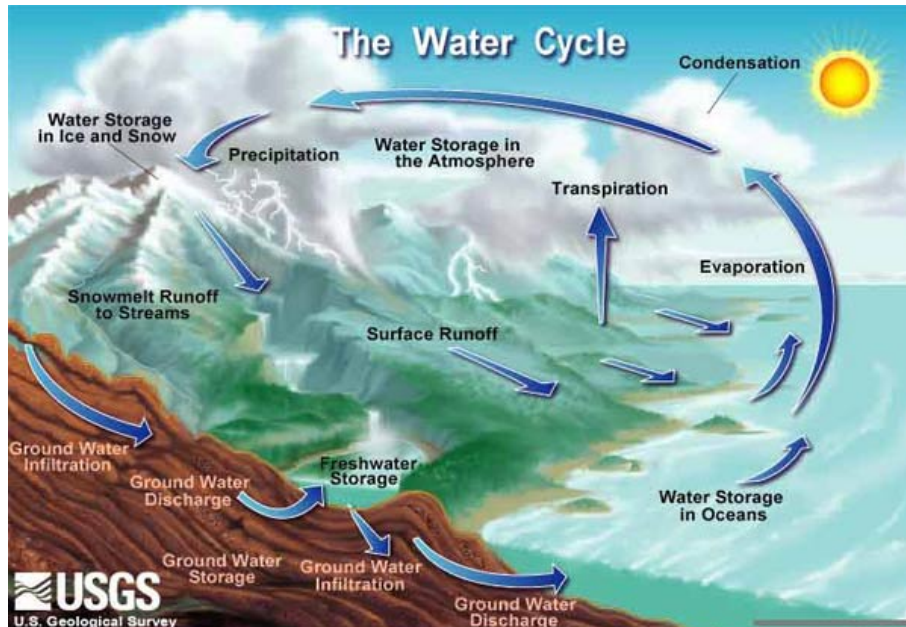


Figure 1.1: Schematic illustration of the global hydrological cycle. Taken from U.S. Geological Survey

Water evaporates from ocean, land and plant surfaces. Moist air is lifted into the atmosphere, it cools and water vapor condenses. Moisture is transported within the atmosphere around the globe and returns to the surface as precipitation. There it can penetrate the surface or flow over the ground as surface runoff, and will be carried to the oceans. 86% of global evaporation and 78% of global precipitation occur over the ocean and, therefore, are the major contributors to the hydrological cycle (Yu, 2011). Solar heating and wind are the main drivers of evaporation from the ocean surface to the atmosphere, increasing salinity in a defined volume of sea water.

As a result, the sea surface salinity (SSS) gives an indication of the hydrological balance between the ocean and the atmosphere and can be used for reducing the uncertainties in surface freshwater flux estimates in the framework of the ocean rain gauge¹ concept (e.g.

¹Improved and continued SSS observations could lead to improved evaporation minus precipitation estimates over the ocean.

Schlundt (2014), Yu (2011), and Font et al. (2004)).

On the one hand, variations of salinity are an expression of varying freshwater transports. Together with temperature, salinity variations have a major influence on the density of seawater and, therefore, the oceanic circulation. On the other hand, variations of salinity can result from a changing ocean circulation due to vertical mixing processes and associated exchanges of freshwater and salt, especially between the surface and sub-surface layers. As mentioned by *Yu (2011)*, at the surface, salinity distributions can also change in response to spatially and temporally varying net surface freshwater fluxes, defined as the sum of evaporation (E) minus precipitation (P) over the ocean plus continental discharge (R), sea ice melting and land ice melting.

The spatial distribution of annually averaged surface salinity shows a close correlation to E-P patterns (e.g. *Yu (2011)*). SSS is high in subtropical regions where evaporation exceeds precipitation (see Fig. 1.2). Surface waters near the equator are less saline than the surface waters in mid-latitudes due to heavy rainfall in the intertropical convergence zone (ITCZ). At higher latitudes precipitation surmounts evaporation under the atmospheric low-pressure gyres resulting in decreasing SSS. The North Atlantic Ocean (until 60°N) is the most saline part of the temperate zone with salinity values >37 (salinities are given in practical salinity scale (PSS-78)), the North Pacific Ocean the freshest with ≈ 32 . As described by *Talley (2002)*, the reason for the salinity difference between the North Atlantic and the North Pacific is the net evaporation. E-P in the North Atlantic is higher and reaches values up to 200 cm per year, caused by the drier trade winds which originate over the African desert. The evaporated freshwater from the North Atlantic subtropics feeds rainfall in the Pacific western tropical regions, where E-P varies between 100 cm per year and 150 cm per year.

High salinities occur in the Mediterranean Sea, the Red Sea and the Gulf of Persia with salinities between 38 and 40. These are regions where the net evaporation is high.

The coastal salinity distribution is locally affected by river runoff from land, but the major river outlets are also important on global scale. Major rivers like the Amazon River, the Congo River, the rivers that empty into the Bay of Bengal (Ganges, Brahmaputra) lower the salinity close to the outlets, which is clearly observable. River runoff from many rivers in the Northeastern Pacific and around the Arctic Ocean lowers the salinities in high northern latitudes *Talley (2002)*.

It is not only the above mentioned processes which influence the global salinity distribution, additionally, horizontal advection by ocean currents has an effect on the salinity

distribution. The North Atlantic salinity maximum is located north of the surface freshwater pattern that is dominated by the excess of evaporation over precipitation (*Qu et al., 2011*). This can be attributed to the poleward advection in the Ekman layer induced by the trade winds (*Qu et al., 2011*).

At high latitudes, freshwater can also originate from melting of land ice and sea ice and changes in freshwater transports by ocean currents. During ice formation, previously dissolved salts are rejected from the ice and collected in pockets in the ice (*Talley, 2002*). These pockets or briny drips penetrate through the ice, mix with the water beneath and increase the salinity. The net increase of salinity depends on the mixed layer below the ice

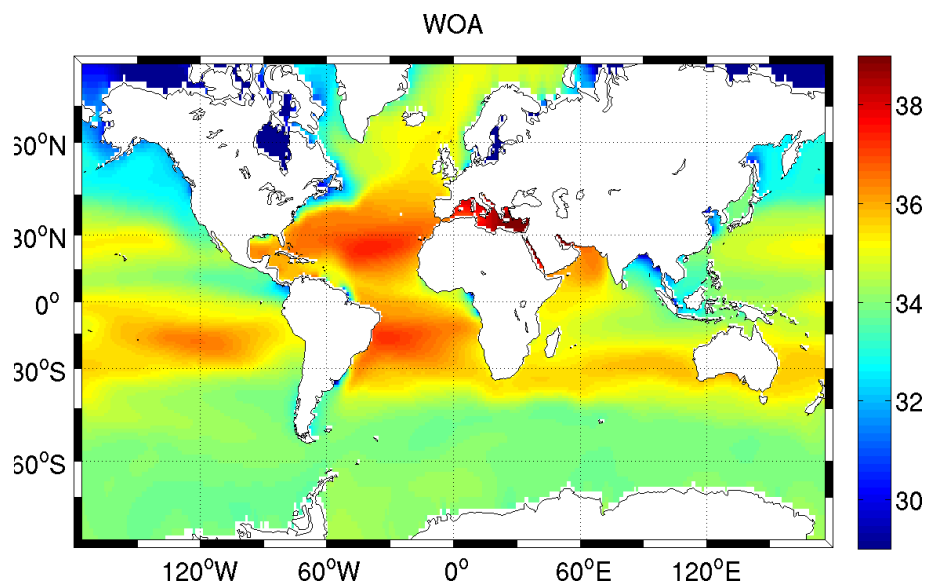


Figure 1.2: Annual average World Ocean Atlas 2009 (WOA09) uppermost salinity (*Seidov et al., 2010*).

(*Talley, 2002*). In shallower areas such as continental shelf's, salinity increases more than in deeper areas where mixing occurs to greater depth. The salinization leads to a density increase and results in the sinking of this denser water until it reaches a depth where it is neutrally buoyant. The salinity of sea ice is much lower than the water it was formed of. Thus, the melting of the sea ice results in a less saline surface layer.

The mixed layer (ML) of the ocean is a quasi-homogeneous region in the upper ocean with only minor variation in temperature or density with depth (*Kara et al., 2000*). The wind-induced input of momentum at the sea surface leads to the mixing of physical properties down to the mixed layer depth (MLD) which depends on the stability of the seawater column and on the incoming energy from the wind (*ESR, 2015*). The less mixing occurs

the shallower is the mixed layer (*ESR, 2015*).

The ML is a dynamical system and affected by physical factors (e.g. direct wind-forcing of the ocean circulation). In addition, important chemical (e.g. dissolution of incoming CO₂ from the atmosphere) and biological (e.g. primary production) processes take place. Entrainment and diffusion occur at the base of the ML (*Qu et al., 2011*).

Understanding the quantities and dynamics in the ML is a main issue in the large context of climate change and still under discussion.

1.2 Motivation

Quantifying salinity variations in the ocean and understanding their underlying processes have to be considered as a fundamental problem of physical oceanography. Salinity is historically one of the consistently under-sampled quantities of the time-varying ocean state, leaving a detailed knowledge about long-term ocean salinity changes still elusive.

Ocean salinity has been measured at sea since the end of the 19th century using buckets to collect samples. The salinity observations were undertaken by various chemical titration techniques for the given seawater sample (*Durack, 2011*). Conductivity-Temperature-Depth (CTD) platforms were developed in the 1950s, providing an increase in data quality, but spatial coverage is limited (*Durack, 2011*).

In the recent past, two technological advances have significantly improved the basis of salinity measurements, finally enabling oceanographers to investigate contemporary salinity variations and their relation to the global hydrological cycle. The first advancement resulted from the advent of the global Argo float array, whose deployment began in 2000. For the first time in history, vertical profiles of salinity observations are provided every 10 days for the top 2000 m with a nominal spatial coverage of 3° globally. Based on these novel data, *Durack and Wijffels (2010)* and *Hosoda et al. (2009)* reported an increase in surface salinity in evaporation-dominated regions and a decrease in precipitation-dominated regions during the period from 1950 to 2008, consistent with an intensification of the global hydrological cycle (*Helm et al., 2010*).

The second major advancement in observing ocean salinity is the launch of two satellite missions designed to retrieve SSS from spaceborne measurements. The first mission is the European Space Agency's (ESA) SMOS ("Soil Moisture and Ocean Salinity", *Font et al. (2004)*), which started retrieving SSS in November 2009, followed by the American National Aeronautical Space Agency's (NASA) "Aquarius/SAC-D" (Satelitte de Aplicaciones Cientificas) mission (*Lagerloef et al., 2008*) two years later. The latter ended on

June 7, 2015 due to an unrecoverable hardware failure. SMOS SSS data are now available on a routine basis, covering the global ocean every 3 days. Aquarius covered the global ocean every 7 days and SSS data are available until June 2015. Significant benefits can be expected from these novel satellite SSS fields for quantitative studies of ocean salinity variations. However, before their full potential can unfold, they need to be tested in a detailed intercomparison of satellite retrievals with *in situ* data.

By now, only few validation studies of SMOS and Aquarius SSS data are available. In addition, most of these studies focus on warm waters with significant salinity variability (spatially and/or temporally), e.g., the Amazon River plume (*Reul et al., 2013*). *Banks et al. (2012)* validated first SMOS SSS retrievals in the Atlantic Ocean between 60°S and 60°N using Argo and model data. More recently, *Boutin et al. (2013)* examined the impact of rainfall on sea surface freshening and compared SMOS and Argo measurements in the high precipitation region of the Pacific Ocean’s ITCZ. *Lee et al. (2012)* studied dynamical SSS features in the eastern equatorial Pacific associated with tropical instability waves, using Aquarius data. Moreover, modern surface drifter measurements of near surface salinity in the top 50 cm and SMOS measurements were compared in high precipitation and tropical regions remote from any land contamination (*Morisset et al., 2012*). All these studies present the capability of satellite-retrieved SSS data in tropical and subtropical ocean regions, where the accuracy of SMOS SSS averaged over 10 days is approximately 0.3 while the accuracy is less than 0.5 in high latitudes (*Boutin et al., 2013*).

First, the quality of satellite-retrieved salinity data differs from one basin to another. Second, data close to coasts are erroneous due to land contamination and are often contaminated due to radio frequency interference (RFI) emanating from sources along coastlines. Third, data in cold ocean regions are less accurate since the sensitivity of the measured brightness temperature – on which SSS data are based – to salinity increases with the sea surface temperature (SST). Given the reduced SMOS sensitivity in cold waters, data are also erroneous in higher latitudes.

Even in warmer ocean regions, where analyses of satellite-retrieved SSS variability on different timescales are possible, the estimation of the mixed layer salinity budget from SSS measurements is challenging. Salinity and E-P patterns are linked through complex upper-ocean dynamics, which complicate estimates of the hydrological cycle from salinity measurements (*Yu, 2011*). SSS anomalies are strongly modified by oceanic advection and mixing (*Yu, 2014*).

This thesis focuses on two unique ocean regions of global importance. The first region

to be investigated in detail is the northern North Atlantic Ocean, where the exchange of water masses has a strong influence on thermohaline conditions. The second region is the Indian Ocean, where ocean-atmosphere interactions affect climate variability across the globe. Both regions are less continuously sampled, and studies requiring salinity data are limited.

In this study I introduce one approach to fill the gap in validation studies by testing SMOS and Aquarius SSS retrievals in comparison with *in situ* salinity observations obtained over regions of cold waters in the subpolar North Atlantic and Nordic Seas. This study aims to show for the first time, that even in cold water, SMOS and Aquarius satellite data are capable of documenting spatial variations in SSS on a seasonal timescale. Aided by model simulations, differences between *in situ* salinity measurements and satellite salinity retrievals will be interpreted in terms of uncertainties in the retrievals (in particular temperature-dependent uncertainties) but also in terms of processes leading to temporal variability and vertical salinity gradients in the ocean.

Another challenging region besides the high northern latitudes is the Indian Ocean, the least sampled among the world's oceans (*Nyadjro and Subrahmanyam, 2014*). In the Indian Ocean, the seasonal reversal of currents and winds affects the budget and influences regional ocean climate processes (*Nyadjro and Subrahmanyam, 2014*). On interannual timescales, the Indian Ocean Dipole (IOD) is an important mode of climate variability which has mostly been examined using east-west SST anomaly differences (*Saji et al., 1999*). The signature of this variability can also be found in SSS anomalies.

In tropical regions various validation studies (e.g. *Reul et al. (2013)*, *Banks et al. (2012)*, *Morisset et al. (2012)*) show that satellite SSS data are less erroneous, and variations on seasonal and interannual timescales are high. Therefore, the high resolution satellite-retrieved SSS can be used to improve estimates of the salinity budget and study freshwater fluxes and surface dynamics responsible for SSS anomalies on various timescales in the Indian Ocean.

Key questions to be addressed in the following chapters are:

1. What is the quality of the satellite-retrieved SSS fields in specific ocean regions?
2. What are the main error sources for differences between satellite-retrieved and *in situ* SSS fields?
3. Do satellite-retrieved salinity fields capture the observed spatial salinity patterns on different timescales?

4. What are the driving mechanisms for SSS variability at different frequencies?
5. To what extent can the salinity budget be closed using satellite-retrieved SSS data?

1.3 Outline

This thesis is structured as follows:

Chapter 2 provides an overview of the data sets used in this study. The measurement principles behind the satellite observations are explained, and the two salinity satellite missions are introduced.

In Chapter 3, a detailed validation of the satellite-retrieved SSS fields is given. There, global and regional results will be presented. The data processing to ameliorate the SMOS SSS data in high northern latitudes is introduced, and the quality of the new SSS product is tested and analyzed with respect to the representation of the processes of the hydrological cycle. The content of this chapter has been published recently in a peer-reviewed journal:

Köhler, J., M. Sena Martins, N. Serra, and D. Stammer (2015), Quality assessment of spaceborne sea surface salinity observations over the northern North Atlantic, J. Geophys. Res. Oceans, 120, 94-112, doi:10.1002/2014JC010067.

SSS dynamics in the Indian Ocean on different timescales are examined in Chapter 4. A detailed description of the computational methods of estimating the salinity budget is given, and the relevant contributions driving these SSS dynamics are discussed by taking the example of the negative Indian Ocean Dipole event in 2010. Further analyzed is the influence of intraseasonal variations on the development of the positive Indian Ocean Dipole in 2012. Therefore, wavelet spectra of outgoing longwave radiation and SSS are investigated in terms of the Madden-Julian Oscillation.

The final Chapter 5 summarizes the results contained in this thesis and provides concluding remarks and recommendations for future work.

Chapter 2

Data and methodology

In this chapter, the principle of salinity remote sensing will be explained. Two satellite missions designed to measure salinity will be summarized and differences between both missions will be explained. The data sets used for comparison, correction and validation as well as the data sets used for the quantification of the different components of the salinity budget are described in detail. In this study, salinities are reported in practical salinity scale (PSS-78).

2.1 Salinity remote sensing

The measurement principle of the passive radiometers on-board of SMOS and Aquarius is based on measuring the intensity of electromagnetic radiation in L-Band (1-2 GHz). The physical basis of microwave remote sensing is the relationship between the radiation emitted by an object or surface and its temperature T . Planck's law expresses the emitted power dependence on the physical temperature and frequency for a black body. A black body is defined as an idealized body that absorbs all incident radiation, regardless of the frequency of the spectrum or the angle of incidence. The intensity I of the black body radiation can be expressed as:

$$I(\nu, T) = \frac{2h\nu^3}{c^2} \cdot \frac{1}{e^{\frac{h\nu}{kT}} - 1} \quad (2.1)$$

where h is the Planck's constant, c the speed of light in vacuum, k the Boltzmann constant and ν the frequency.

At microwave frequencies ($\nu < 117$ GHz), Eq. 2.1 can be simplified using the Rayleigh-Jeans approximation ($h\nu \ll kT$):

$$I(\nu, T) = \frac{2kT\nu^2}{c^2} \quad (2.2)$$

For the physical temperature T it holds:

$$T = \frac{I(\nu, T)c^2}{\nu^2 2k} \quad (2.3)$$

For a black body the physical temperature and the brightness temperature T_B are theoretically the same. In nature, objects do not behave as a perfect emitter or absorber like a black body and have a smaller brightness than a black body at the same physical temperature. The sea surface T_B is a product of the sea surface emissivity ϵ and the SST. ϵ is a complex function of permittivity of seawater, viewing angle, polarization and factors like foam, wind and surface roughness (*Lagerloef et al., 1995*). The more reflective a surface or material is, the lower is the emissivity and vice versa. The emissivity for a flat surface at local thermodynamical equilibrium at incidence angle θ from the vertical is:

$$\epsilon_p = 1 - R_p \quad (2.4)$$

where R_p is the square of the Fresnel reflection coefficient for the horizontal (H) and vertical (V) polarization p (*Lagerloef et al., 1995*):

$$R_H = \left| \frac{\cos \theta - \sqrt{\epsilon - \sin^2 \theta}}{\cos \theta + \sqrt{\epsilon - \sin^2 \theta}} \right|^2 \quad (2.5)$$

$$R_V = \left| \frac{\epsilon \cos \theta - \sqrt{\epsilon - \sin^2 \theta}}{\epsilon \cos \theta + \sqrt{\epsilon - \sin^2 \theta}} \right|^2 \quad (2.6)$$

where ϵ is the permittivity of seawater. The permittivity or dielectric constant can be represented by the Debye formula:

$$\epsilon = \epsilon_\infty + \frac{\epsilon_s - \epsilon_\infty}{1 + i2\pi\nu\tau} - i \frac{\sigma}{2\pi\nu\epsilon_0} \quad (2.7)$$

where ϵ_s and ϵ_∞ are the static and high-frequency permittivity, ϵ_0 is the permittivity of free space, τ is the relaxation time and σ the conductivity of seawater, and i is the

imaginary unit (*Guillou et al., 1998*). As pointed out by *Swift and McIntosh (1983)*, lower frequencies have a better sensitivity of the brightness temperature due to salinity changes than higher frequencies. SMOS and Aquarius measure at 1.43 GHz and 1.413 GHz. In

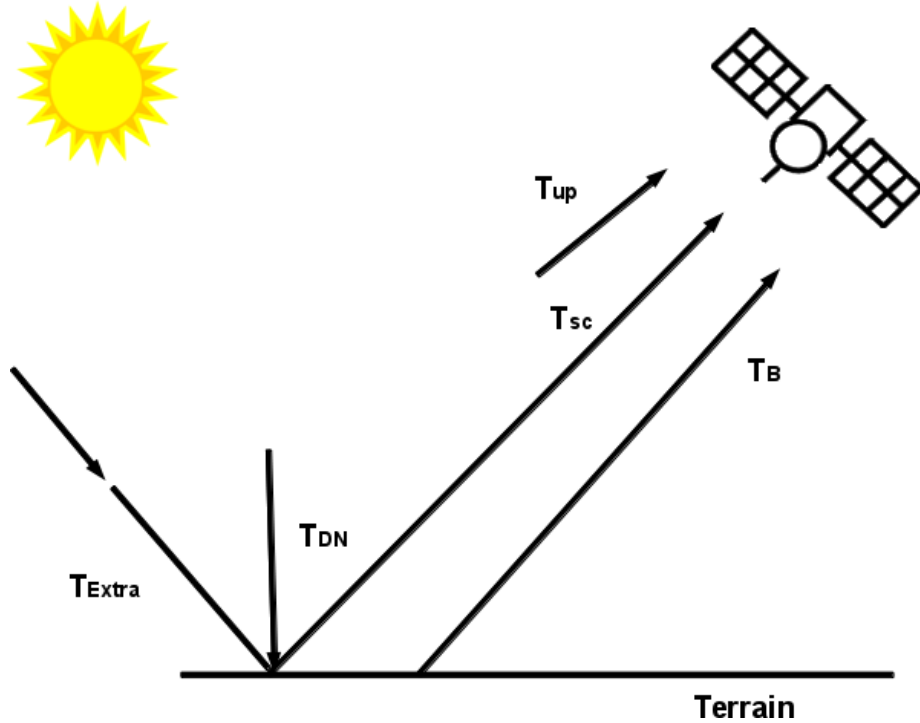


Figure 2.1: *Passive remote sensing scenario. The measured radiation comes from several sources. T_{up} is the direct atmospheric radiation, T_{sc} is the sum of the extraterrestrial radiation T_{Extra} and the atmospheric radiation T_{DN} reflected by the Earth's surface, T_B is the brightness temperature.*

L-Band, the sensitivity of the permittivity to salinity in the first centimeter of the ocean is at its highest point. As mentioned above, T_B is also affected by surface roughness. This is the major geophysical error source which can modify the measured T_B by several Kelvin (*Font et al., 2004*). T_B at polarization p and incidence angle θ can be expressed as (*Zine et al., 2008*):

$$T_B(\theta, SSS, SST, P_{rough}) = T_{B_{flat,p}}(\theta, SSS, SST) + T_{B_{rough,p}}(\theta, SSS, SST, P_{rough}) \quad (2.8)$$

where $T_{B_{flat}}$ is the brightness temperature of a flat surface, and $T_{B_{rough}}$ is the contribution of sea surface roughness, and P_{rough} characterizes the roughness. Different to Aquarius, SMOS does not carry any active instrument for roughness determination simultaneously,

therefore, auxiliary information is necessary to correct this effect (*Font et al., 2004*). *Talone (2010)*, *Zine et al. (2008)* and *Yueh (1997)* give a brief overview of the different emissivity models for calculating T_B from SMOS measurements, taking into account the surface roughness. Another advantage of the L-Band frequency range is that the atmospheric attenuation is nearly zero. This property allows for the detection of microwave radiation under almost all weather and environmental conditions, with the result that data can be collected at any time.

Radiometers do not only measure the radiation emitted from the Earth's surface, but the sum of several contributions as ground emission, atmospheric emission and the cosmic background (see Fig. 2.1), which can be expressed as the apparent temperature T_{AP} (*Ulaby et al., 1986*):

$$T_{AP} = T_{up} + \Upsilon [T_B + T_{SC}] \quad (2.9)$$

where T_{UP} is the direct atmospheric contribution according to the path from the source to the satellite and Υ is the atmospheric transmissivity.

The scattered temperature T_{SC} consists of the radiation from extraterrestrial sources T_{Extra} and the downward atmospheric radiation T_{DN} :

$$T_{SC} = \Gamma [T_{DN} + \Upsilon T_{Extra}]. \quad (2.10)$$

Both T_{DN} and T_{Extra} are reflected at the Earth's surface with the surface reflectivity Γ . From this it follows for Eq. 2.9:

$$T_{AP} = T_{UP} + \Upsilon T_B + \Gamma \Upsilon T_{DN} + \Gamma \Upsilon^2 T_{Extra} \quad (2.11)$$

T_{Extra} is defined as the sum of the cosmic brightness temperature T_{COS} and the galactic brightness temperature T_{GAL} :

$$T_{EXTRA} = T_{COS} + T_{GAL}. \quad (2.12)$$

According to Eq. 2.11 T_B , T_{DN} and T_{Extra} are attenuated depending on the atmospheric transmissivity.

Each of these contributions depends on the frequency, geometrical shape, atmospheric contributions and the physical state and should be well known to get a good result of the geophysical parameter retrieval (*Talone, 2010*).

Salinity determination

The retrieval of salinity is a minimization problem, which requires the knowledge of other geophysical and environmental factors. For this purpose, a maximum-likelihood Bayesian approach is used, taking advantage of background information about physical parameters including SSS, SST and roughness parameter P_{rough} (Gabarro *et al.*, 2009). The satellite T_B^{sat} measured at different incident angles θ are fitted to a set of theoretical modeled T_B^{model} by minimizing the cost function (Gabarro *et al.*, 2009):

$$\chi^2 = \frac{1}{N} \sum_{i=0}^{N-1} \frac{[T_{B_i}^{sat} - T_{B_i}^{model}(\theta, SSS, SST, P_{rough})]^2}{\sigma_{T_B}^2}. \quad (2.13)$$

T_B^{model} are simulated at N different incidence angles using Eq. 2.8. σ_{T_B} is the standard deviation between the measured and the modeled T_B . By a recursive least-square process¹, the geophysical parameters are updated until the cost function converges (Reba *et al.*, 2014).

2.1.1 SMOS mission

SMOS was launched in November 2009 and, with its Microwave Imaging Radiometer using Aperture Synthesis (MIRAS) instrument, measures the microwave radiation emitted from the Earth's surface. ESA's SMOS mission pioneers a completely new synthetic aperture antenna technique, which requires the space-time inversion of measurements made from 69 small receivers, that interact simulating a large conventional antenna during 1.2-sec time frames arranged along Y-shaped antenna arms (McMullan *et al.*, 2008). The 69 receivers measure the incident radiation in L-Band on horizontal and vertical polarizations in the antenna reference frame.

SMOS flies in a sun-synchronous orbit, crossing the equator at the same local mean solar time on its ascending (from south to north) and descending (north to south) path, covering the global ocean every 2.7 days. From an altitude of 763 km and an orbital inclination of 98.4° the satellite has an hexagonal-shaped, alias-free footprint of 1000 km in diameter (ESA, 2010).

¹The minimal χ^2 is compared to a desired threshold in each iteration.

Interferometry in L-Band

The SMOS payload MIRAS maps the T_B by means of 2-D aperture synthesis interferometry. The radiometer using the interferometric principle does not measure the brightness temperature directly, but its Fourier transform over the field of view (FOV).

The measurements of the interferometric aperture synthesis radiometer are the antenna temperature and the visibility (*Corbella et al., 2004*). The antenna temperature is the

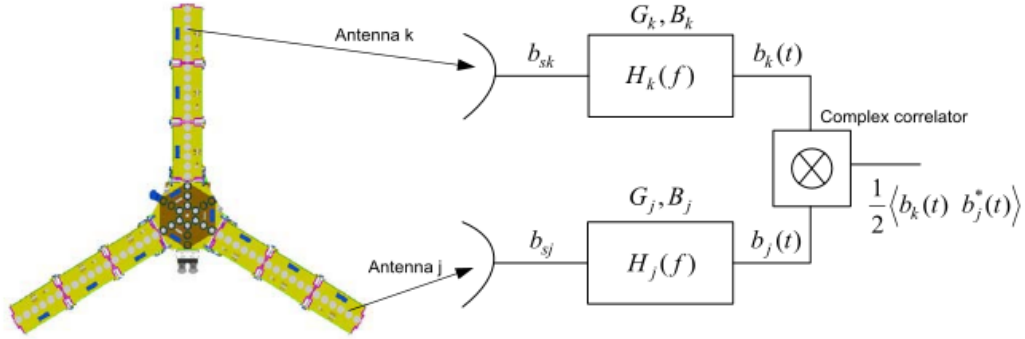


Figure 2.2: *Technical scheme of a single baseline relating the measurement of a visibility sample. Courtesy of Gambau (2012).*

thermal signal measured by a single receiver. The visibility is the complex cross-correlation between the signals $b_k(t)$, $b_j(t)$, measured by each receiver pair k and j (Fig. 2.2, *Corbella et al. (2009)*). The visibility is equivalent to the Fourier transform of the T_B distribution in the FOV and therefore a function of receiver spacing. For any two receivers k and j with $k \neq j$ the visibility $V_{kj}(u_{kj}, v_{kj})$ is:

$$V_{kj}(u_{kj}, v_{kj}) = \int \int_{\xi^2 + \eta^2 < 1} T'_{B_{kj}}(\xi, \eta) e^{-j2\pi(u_{kj}\xi + v_{kj}\eta)} d\xi d\eta \quad (2.14)$$

where

$$u_{kj} = \frac{(x_j - x_k)}{\lambda_0} \quad (2.15)$$

and

$$v_{kj} = \frac{(y_j - y_k)}{\lambda_0} \quad (2.16)$$

are the components of the baseline vector normalized by the wavelength λ_0 . The coordinates $(\xi, \eta) = (\sin\theta\cos\phi, \sin\theta\sin\phi)$ are the director cosines of the incident waves referred

to the instrument's geometrical coordinate frame. (x_k, y_k) and (x_j, y_j) are the positions for all pairs of different receivers. $T'_{B_{kj}}$ is the modified brightness temperature, which includes the brightness temperature as well as the antenna noise and antenna pattern. The visibility is measured for all pairs of antenna receivers. For every single visibility sample a relative internal error correction must be performed before applying the image inversion procedure to obtain the modified brightness temperatures.

In an ideal case, the T'_B maps could be retrieved directly from the calibrated visibilities by applying an inverse Fourier transform. However, MIRAS is a Y-shaped interferometer, so visibility samples are measured over a hexagonal grid in the spatial frequencies domain (*Gambau, 2012*). Therefore, a hexagonal grid (ξ, η) inverse to the (u, v) grid is required. This is done by changing the variables from (u, v) to (k_1, k_2) and (ξ, η) to (n_2, n_1) , in which both are identical regular grids of $N_T \times N_T$ integers, where N_T^2 is the number of non-redundant (u, v) points (*Corbella et al., 2009*). After averaging all redundant visibilities, the inverse Fourier transform is:

$$T'(n_2, n_1) = \Delta A \sum_{N_m}^{N_M} \sum_{N_m}^{N_M} V(k_1, k_2) e^{j \frac{2\pi}{N_T} (k_1 n_2 + k_2 n_1)}. \quad (2.17)$$

In this formula, ΔA is the pixel size, k_1 and k_2 are the wavenumbers, n_1 and n_2 are the grid points. The limits of the summation are:

$$[N_m, N_M] = \begin{cases} [-\frac{N_T}{2}, \frac{N_T}{2} - 1], N_T \text{ even} \\ [-\frac{N_T-1}{2}, \frac{N_T-1}{2}], N_T \text{ odd} \end{cases} \quad (2.18)$$

The calibrated visibility function is then inverted by an image reconstruction algorithm to get T_B as a function of the director cosines at the antenna reference plane. A detailed discussion of the interferometric principle and a complete formulation of the visibility function and the conducted transformations of the visibility function as well as a description of the necessary calibration procedures and further correction techniques can be found in *Gambau (2012)*, *Corbella et al. (2009)* and *Corbella et al. (2004)*.

The major advantages of interferometry, are on the one hand the small Y-shaped antenna, and on the other hand, the multi-angular measurement, which increases the inversion's robustness. The output is an image having several views with different incidence angles on one point of the Earth's surface before it exits the FOV. The resulting FOV of the satellite covers a swath of about 1000 km in width, over which MIRAS features a spatial resolution ranging from 35 km in the center to ≈ 80 km at the edges of the swath.

Level 4 SSS product

ESA produces SMOS Level 2 salinity products, which are available from year 2010 onward. Here, Level 4 SMOS SSS products from the Barcelona Expert Centre (BEC) are used. These products are based on the ESA's Level 2 (L2) Ocean Salinity User Data Product (UDP) and Ocean Salinity Data Analysis Product (DAP). During the SSS retrieval auxiliary information like SST, atmospheric parameters and the wind descriptors were taken into account (see Eq. 2.13). The auxiliary data are taken from the European Centre for Medium-Range Weather Forecasts (ECMWF).

Before BEC creates the Level 3 (L3) and Level 4 (L4) products – all based on the third roughness model² – geographical, retrieval and geometrical filters are applied to the reprocessed L2 data (*SMOS-BEC Team, 2014*). For example, data with suspected ice presence or grid points contaminated by RFI by more than 33% were sorted out. The level 4 product is based on fusing L3 binned maps using the singularity analysis technique (*Umbert et al. (2014)* and *Turiel et al. (2009)*) applied to the high resolution Operational Sea Surface Temperature and Sea Ice Analysis (OSTIA) SST fields (*Donlon et al., 2012*). The singularity analysis is a technique for estimating the singularity exponents of a signal that characterizes the presence of ocean structures in different scalars (*Umbert et al., 2014*). For any given scalar quantity like SST, SSS or sea surface height (SSH), the singularity exponents can be calculated. These exponents are dimensionless measures for the sharpness of regularity of the variation of the scalar quantity around a given point (*Umbert et al., 2014*). *Umbert et al. (2014)* and *Isern-Fontanet et al. (2007)* show that the correspondence of singularity exponents of two quantities with different quality can be used to reduce the effects of noise and artifacts on a given scalar field with lower quality. The SST fields are assumed to have a higher quality than the SMOS SSS fields and are used to improve the quality of the signal by restoring the singular structure that both quantities are presumed to share. Although this technique does not attempt to correct for biases, regional structures are better preserved, which is of importance, especially in frontal zones. The SSS fields can be downloaded at <http://cp34-bec.cmima.csic.es/ocean-reprocessed-dataset/>. The L4 product with a monthly temporal resolution and a spatial resolution of $0.25^\circ \times 0.25^\circ$ grid is used, which I gridded to $1^\circ \times 1^\circ$.

For the analysis of intraseasonal variabilities, the BEC L4 fused product with a temporal resolution of 3 days is used.

²Model 3 is a semi-empirical formulation derived from data sets provided by a field campaign in the Mediterranean Sea (Wind and Salinity Experiment, WISE) to estimate the emission of the sea surface in L-Band dependent on different geophysical parameters and the surface roughness (*Zine et al., 2008*).

As explained in *Font et al. (2013)* and *Gabarro et al. (2012)*, contamination from land is still a problem when land masses enter the very wide SMOS antenna field of view. Thus, absolute salinity values within a band of 1500 km around the main continental masses and ice have to be treated with caution (*Gabarro et al., 2012*). SSS retrieved in the northern North Atlantic and around Asian coasts are contaminated by RFI.

2.1.2 Aquarius mission

The NASA Aquarius/SAC-D instrument comprises a passive microwave radiometer operating in L-band at 1.413 GHz and an active scatterometer operating at 1.26 GHz (*Aslebaugh, 2013*). Aquarius flies in a sun-synchronous polar orbit and crosses the equator at 6 am (descending) and 6 pm (ascending) local time. Aquarius directly retrieves brightness temperatures in approximately 390 km wide swaths with a global coverage of ice-free ocean every 7 days from an altitude of 657 km and an inclination of 98° . The Aquarius instrument consists of three L-band horn antennas sharing a common parabolic reflector. Each horn antenna connects to a separate Dicke radiometer, and the scatterometer is time-shared sequentially between the three horns, which means that the scatterometer signal is rotated among the three horns and through vertical and horizontal polarization channels. To prevent solar contamination, the three horn antennas point away from sun and perpendicular to the direction of flight (*Aslebaugh, 2013*).

Though the FOV is smaller for Aquarius than for SMOS, the SMOS resolution is higher due to the interferometric principle of the 69 small receivers. Between its launch in the summer of 2011, and the end of the mission in June 2015, Aquarius provided global SSS fields with a spatial resolution of about 100 km. While sea surface roughness is estimated from additional wind fields for the SMOS salinity retrievals, Aquarius' on-board scatterometer provides a critical roughness correction for the passive SSS retrievals.

Like SMOS, Aquarius SSS fields are also affected from land contamination, but as its FOV is much smaller, the land contamination is reduced down to 400 km (*Aretxabaleta et al., 2010*). Table 2.1 summarizes the main mission characteristics of SMOS and Aquarius.

Aquarius SSS retrievals

In this study, monthly as well as 7-day smoothed fields at $1^\circ \times 1^\circ$ spatial resolution from January 2012 to December 2013 were used. The L3 fields (version V3.0) used

Table 2.1: Summary of the mission characteristics of the SMOS and Aquarius satellites.

	SMOS	Aquarius/SAC-D
Instrument	MIRAS	Aquarius
Instrument concept	Passive microwave 2D-interferometer	Passive radiometer and active scatterometer
Orbit	Sun-synchronous	Sun-synchronous
Altitude	763 km	657 km
Frequency	1.43 GHz	1.413 GHz and 1.26 GHz
Spatial resolution	35 km at the center of the FOV with a radiometric accuracy $\approx 1.2\text{K}$	79×94 km for inner beam
Temporal resolution	3 days	7 days

and their metadata were obtained the JPL Physical Oceanography Distributed Active Archive Center (PODAAC, <ftp://podaac-ftp.jpl.nasa.gov/allData/aquarius/L3/mapped/V3/monthly/SCISM/>) available since June 2014. The changes made between version V2.0 and V3.0, documented in *Meissner et al. (2014)*, are, for example, an update of the antenna pattern coefficients, the use of Aquarius-derived wind speeds in the roughness correction and an empirical correction of the reflected galactic radiation, which reduces the bias between ascending and descending passes.

The V3.0 product also contains an adjusted SSS SSS_{ba} . A bias was found when comparing Aquarius SSS with HYbrid Coordinate Ocean Model (HYCOM) SSS and Argo salinities. The zonal character of this bias suggests a correlation with SST (*Meissner et al., 2014*). Hence, the adjustment was obtained by fitting a second order polynomial in SST to the observed Aquarius minus HYCOM SSS differences (*Meissner et al., 2014*):

$$SSS_{ba} = SSS_{Aq} - \Delta SSS(SST) \quad (2.19)$$

with

$$\Delta SSS(SST) = -0.0019594 \cdot SST^2 + 1.1257 \cdot SST - 161.4934. \quad (2.20)$$

SSS_{Aq} is the L2 Aquarius SSS product.

For HYCOM, the Navy Coupled Ocean Data Assimilation was used, including also Argo temperature and salinity profiles. For an independent comparison of the salinity products, the Aquarius V3.0 data product, which is not corrected for any SST-dependent bias, is used. For the validation study located in the higher northern latitudes, the bias adjusted Aquarius product is used.

2.2 Ship-based thermosalinograph data

Ship-based thermosalinograph (TSG) salinity measurements were acquired simultaneously with SMOS and Aquarius measurements from the German research vessels RV "Poseidon" (cruises P437-1 and P437-2) and RV "Maria S. Merian" (cruises MSM21-1, MSM21-3 and MSM27), as well as from the Norwegian RV "Johan Hjort" and RV "G.O. Sars".

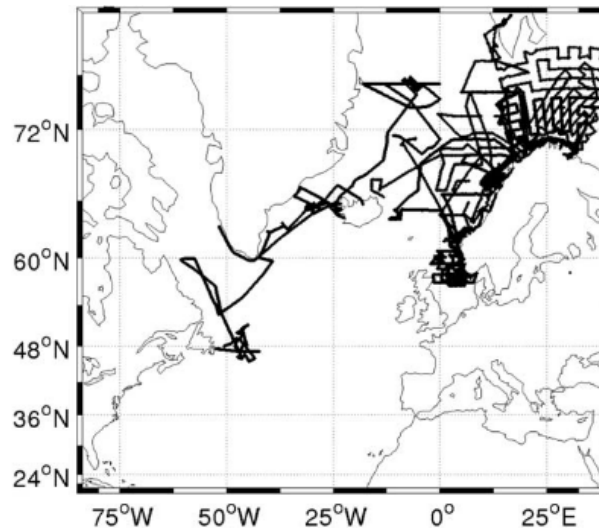


Figure 2.3: *Cruise tracks along which in situ thermosalinograph data were collected.*

All research vessels operated in the subpolar North Atlantic and Nordic Seas during the period from May 2012 until April 2013 (except for January 2013). Figure 2.3 shows all cruise tracks from which data are used in this study. As a first analysis step, the 1Hz TSG measurements were calibrated using bottle samples and CTD measurements available in 4-8 m depth. An example of the resulting TSG salinity variations is shown in Fig. 2.4 together with the CTD measurements used for calibration of the TSG salinity. A comparison involving all data reveals an accuracy of the point-wise TSG data of 0.005 at the depth of the measurement where the ships' hull water intake takes place. For a comparison with the satellite data, TSG observations were monthly averaged within the same $1^\circ \times 1^\circ$ grid for which SMOS and Aquarius data are available. For the later interpretation of the results it should be noted that SMOS measurements represent the salinity values of the top centimeter of the sea surface, whereas the TSG measurements originate from 4-8 m depth levels.

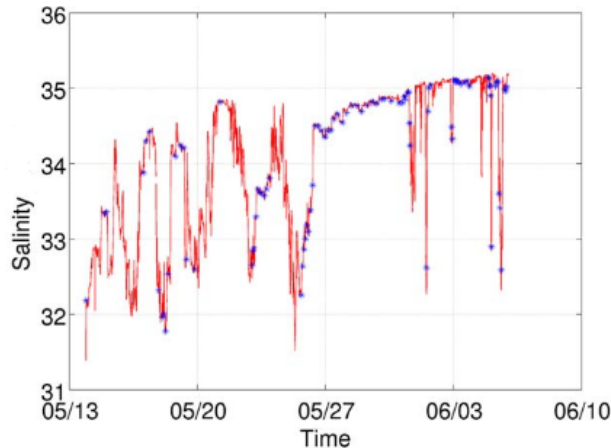


Figure 2.4: *Thermosalinograph salinity measured during May 2012 and June 2012 along one cruise track of the German R/V "Maria S. Merian" (solid line). CTD measurements used for calibration of the thermosalinograph data are shown with asterisks.*

2.3 Argo float data

To validate the salinity variability, a gridded *in situ* salinity product is used, comprising mostly Argo float data. The EN4.1.1 product of the Met Office Hadley Centre, provides series of data sets of global quality-controlled ocean temperature and salinity profiles and monthly objective analyses. For this product, data from all types of ocean profiling instruments, measuring temperature and salinity were merged into one data set. Argo data from the year 2000 onward were obtained from the Argo global data assembly centers. A detailed description of data sources, quality control procedures, processing, and the method of analysis can be found in *Good et al. (2013)*. The product, hereafter "Argo product", has a monthly resolution and is optimally interpolated to a $1^\circ \times 1^\circ$, with covariance scales of 300 and 400 km in zonal and meridional direction, respectively (*Good et al., 2013*).

Individual profile data are used to determine the MLD. As described in Chapter 1 the ML is defined as a layer of constant potential density and the MLD is the depth at which density starts to increase. A second definition of the ML is a layer of constant temperature and the isothermal layer depth (ILD) is the depth at which temperature starts to decrease. These two estimates of the MLD were calculated from individual Argo profiles, following *de Boyer Montégut et al. (2004)*. Here, the ILD is defined as the depth at which temperature changed by a threshold value of $\Delta T = \pm 0.2^\circ\text{C}$ relative to the temperature T_0 at a reference pressure of 10 dbar. The MLD is the depth at which potential density σ changed relative to the reference pressure by an amount of $\Delta\sigma = 0.03 \frac{\text{kg}}{\text{m}^3}$. $\Delta\sigma$ is calculated

as the potential density change equivalent to the same temperature change at the local salinity:

$$\Delta\sigma = \sigma(T_0 + \Delta T, S_0, P_{surf}) - \sigma(T_0, S_0, P_{surf}). \quad (2.21)$$

P_{surf} is the pressure at ocean surface.

The MLD and ILD were averaged over the domain of the box and the averaged salinity within the MLD is taken as the mixed layer salinity (MLS).

2.4 World Ocean Atlas

The World Ocean Atlas (WOA) is a set of gridded and interpolated climatological distribution fields of *in situ* temperature, salinity, dissolved oxygen, apparent oxygen utilization, percent oxygen saturation, phosphate, silicate and nitrate (*Seidov et al., 2010*). Data sources are historical profile data from bottle samples, CTDs, floats, moorings, drifters, gliders and undulating oceanographic recorders available from the National Oceanographic Data Center and World Data Center (*Seidov et al., 2010*). In order to produce a gridded product, original data were checked for their quality. As described in *Seidov et al. (2010)* values outside the expected oceanographic ranges were sorted out and further statistical checks were performed. Then, the data were vertically interpolated to 33 selected standard depth levels from the surface to 5500 m depth. Next, the data were horizontally interpolated on each of the 33 standard depth levels by using an objective analysis technique.

Maps are presented for annual, seasonal and monthly averaging periods on a $1^\circ \times 1^\circ$ grid. The WOA also includes statistical fields (statistical mean, number of measurements, standard deviation) of observed oceanographic measurements interpolated to standard depth levels (*Seidov et al., 2010*). The salinity climatologies are monthly averages over five different periods to reduce the effects of irregular space and time sampling: 1955-1964, 1965-1974, 1975-1984, 1985-1994 and 1995-2006 (*Seidov et al., 2010*).

For the present study, data from the first standard depth level are used. These SSS data were derived from observations originating at the upper five meters of the ocean, which were extrapolated to the sea surface. The SSS actually represents the salinity of the sea surface layer at about 5 m depth. For an independent comparison the WOA 2009 (WOA09) were chosen instead of the more up to date WOA 2013, which also includes the Argo data I use.

2.5 General circulation models

In order to demonstrate that satellite retrieved SSS fields are capable of documenting spatial and temporal variability, general circulation models can be used complementary for the study of salinity variabilities from the observational point of view. This study uses the output of two general circulation models, Massachusetts Institute of Technology general circulation model (MITgcm) for the North Atlantic and the STORM simulation on global scale. The different model characteristics will be described next.

2.5.1 MITgcm/Eddy-resolving model

The interpretation of the SMOS- and Aquarius-retrieved SSS obtained in the high northern latitudes is aided by using the output from an eddy-resolving numerical circulation model of the North Atlantic and Arctic oceans. The model is based on the MITgcm (*Marshall et al., 1997b*) and was configured for the Atlantic Ocean north of 33°S , including the Mediterranean and Baltic Seas, the Nordic Seas and the Arctic Ocean (*Serra et al., 2010*). It ran at a horizontal resolution of about 4 km (about $1/24^{\circ}$ at the equator). The vertical discretization (with 100 vertical levels) varies between 5 m in the upper 200 m and 275 m in the deep ocean. The model bathymetry was extracted from the Global Digital Elevation Model (ETOPO2). The initial model temperature and salinity fields were taken from another run, which was performed with a 8 km spatial resolution and initialized with annual mean temperature and salinity from the WOA09 climatology. The model is forced at the surface by fluxes of momentum, heat and freshwater computed by bulk formulae and 6-hourly atmospheric state fields from the ECMWF/ERA-interim Reanalysis (*Dee et al., 2011*). During the run, the model SSS is weakly relaxed to the Polar Science Center Hydrographic Climatology 3.0 (*Steele et al., 2001*) with a relaxation timescale of one month. At the open northern and southern boundaries, the model is forced by results of $1^{\circ} \times 1^{\circ}$ resolution global MITgcm simulation. Vertical mixing is parameterized by the non-local K-Profile Parameterization (KPP) scheme (*Large et al., 1994*). The background coefficient of horizontal viscosity was set to $3 \times 10^9 \text{ m}^4 \text{ s}^{-1}$, and background coefficients of vertical viscosity and diffusion were set to $1 \times 10^{-4} \text{ m}^2 \text{ s}^{-1}$ and $1 \times 10^{-5} \text{ m}^2 \text{ s}^{-1}$, respectively. In this study, the daily averaged salinity output from the uppermost model layer at 2.5 m depth is used.

2.5.2 STORM model

For global comparisons as well as the regional study of salinity anomalies in the Indian Ocean, the output of STORM simulations is used. The STORM simulations consist of atmosphere and ocean model components are based on the latest version of the ECHAM³ atmosphere model and the Max-Planck Institute for Meteorology Ocean Model (MPI-OM). The ocean model component MPI-OM TP6M (*Wetzel et al., 2007*) uses a Mercator grid with a horizontal resolution of 0.1° at the equator and $1/10^\circ \cdot \cos(\text{latitude})$ away from the equator. This setup yields a total number of 3600×2392 horizontal grid points and 80 vertical layers with a thickness of 10-15 m in the first 200 m, increasing gradually to 279 m for the deepest layer at 6038 m. A curvilinear tripolar grid was chosen to achieve an almost evenly spaced ocean grid. The model is based on the discretized primitive equations for a hydrostatic Boussinesq fluid (e.g. *Cushman-Roisin and Beckers (2011)*). The model is coupled to a sea ice model that includes the dynamics of sea ice circulation, the thermodynamics of sea ice growth and melting, and the thermohaline coupling to the ocean model (brine rejection) (*Wetzel et al., 2007*). A spin-up period of 25 years was applied using the German Ocean Model Intercomparison Project (OMIP) forcing derived from the 15 year ECMWF/ERA reanalysis (ERA15) (*von Storch et al., 2012*). After the 25-year spin-up phase and the reaching of a quasi-equilibrium of the kinetic energy in the deep ocean, the forcing was switched to the 6-hourly NCEP/NCAR reanalysis-1 (*Kalnay et al., 1996*). Further information about the STORM model setting can be found in *von Storch et al. (2012)*. The resulting run will be referred to as the STORM simulation.

2.6 Auxiliary datasets

To quantify all relevant components of the salinity budget, additional data like surface freshwater fluxes, momentum and velocities, are required. The salinity budget calculation will be described in Section 4.2.

Atmospheric data

To assess the role of atmospheric freshwater fluxes on salinity variability, objectively analyzed air-sea fluxes (OAFLUX) evaporation estimates with a monthly $1^\circ \times 1^\circ$ resolution

³Combination of its origin (the 'EC' abbreviating 'ECMWF') and the place of development of its parameterization, Hamburg.

(<http://oaflex.who.edu/data.html>) are used.

Precipitation data were obtained from the Tropical Rainfall Measuring Mission's (TRMM) Microwave Imager (TMI), which is a multi-channel, dual-polarized, conical-scanning passive microwave radiometer designed to measure rain rates over a wide swath under the TRMM satellite. In addition to rain rates, TMI measures also other geophysical parameters as SST, water vapor and cloud liquid water.

Monthly TMI data on a $1^\circ \times 1^\circ$ grid are produced by Remote Sensing Systems and sponsored by the NASA Earth Science MEaSUREs DISCOVER Project. Data are available at www.remss.com.

For the calculation of the subsurface influences – which are composed of entrainment and vertical pumping – as well as the determination of the horizontal Ekman transport, wind speed and direction are needed. These data originate from the WindSat Polarimetric Radiometer, developed by the Naval Research Laboratory (NRL) Remote Sensing Division and the Naval Center for Space Technology for the U.S. Navy and the National Polar-orbiting Operational Environmental Satellite System (NPOESS) Integrated Program Office (IPO).

Monthly averaged WindSat fields with a spatial resolution of $0.25^\circ \times 0.25^\circ$ are produced by Remote Sensing Systems and sponsored by the NASA Earth Science MEaSUREs DISCOVER Project and the NASA Earth Science Physical Oceanography Program. RSS WindSat data are available at www.remss.com.

The wind stress is calculated following the formula by *Large and Pond (1981)*:

$$\tau = c_D \rho_{air} U^2 \quad (2.22)$$

where U is the wind speed at 10 m above the sea surface, ρ_{air} the air density and c_D a dimensionless drag coefficient (*Large and Pond, 1981*):

$$c_D = \begin{cases} 1 \cdot 10^{-3} & \text{for } 4 < U < 11 \\ (0.49 + 0.065 \cdot U) \cdot 10^{-3} & \text{for } 11 < U < 25 \end{cases}$$

For the analysis of intraseasonal variabilities, the described datasets with a temporal resolution of 7 days are used.

Outgoing Longwave Radiation (OLR) data are necessary for comparisons on intraseasonal time scales described in detail in Chapter 4.3. OLR data at the top of the atmosphere are observed from the Advanced Very High Resolution Radiometer (AVHRR) instrument aboard the NOAA polar orbiting spacecraft.

Interpolated OLR data are provided by the NOAA/OAR/ESRL PSD, Boulder, Colorado, USA, from their website at <http://www.esrl.noaa.gov/psd/> (*Liebmann and Smith, 1996*). The OLR product has a spatial resolution of $2.5^\circ \times 2.5^\circ$ and a temporal resolution of 1 day.

Velocity data

Surface velocities are required to estimate the advection terms, explained in more detail in Section 4.2.

Zonal and meridional velocities from the satellite-based OSCAR surface current product are used, which are monthly filtered averages on a $1^\circ \times 1^\circ$ grid available at <http://www.oscar.noaa.gov/>.

The currents are computed by a straightforward linear combination of geostrophic and wind-driven motion *Johnson et al. (2006)*.

Also, geostrophic velocity fields are used, produced by Ssalto/Duacs and distributed by Archiving, Validation and Interpretation of Satellite Oceanographic Data (AVISO), with support from the Centre National d'Etudes Spatiales (CNES). The geostrophic velocities are derived from merged SSH fields of TOPEX/POSEIDON, Jason-1, ERS-1 and 2, Envisat and GFO. A detailed description can be found in *Ducet et al. (2000)*. The geostrophic velocity fields from January 2010 onward have a spatial resolution of $0.25^\circ \times 0.25^\circ$ and temporal resolution of 7 days. To be consistent with the monthly salinity fields, the geostrophic velocity is averaged to a monthly $1^\circ \times 1^\circ$ grid.

Chapter 3

Quality assessment of spaceborne sea surface salinity observations

Before analyzing SSS and SSS variability, obtained from satellite measurements, these data have to be validated. This chapter provides an intercomparison of observations obtained from satellites with *in situ* observations and model simulations of SSS on global scale for the 4-year period from January 2010 to December 2013. The Aquarius period started in January 2012 as Aquarius was launched in mid-2011. The quality of satellite observations varies locally and regional considerations are of importance. Therefore, two regions of the world ocean with different characteristics are presented in detail in the following sections. A bias-correction approach utilizing the data will be presented and validated and causes for the differences between the datasets are discussed.

3.1 Validation on global scale

Presented in Fig. 3.1 are the annually averaged SSS fields of SMOS, Aquarius, Argo and STORM. The SMOS and Aquarius data show the main characteristics of the global SSS distribution, e.g. the high-salinity subtropical gyres, the fresh Amazon plume and the less saline waters in the ITCZ. The less saline waters in the higher northern latitudes are observable. Remarkable is the average difference between SSS from SMOS and WOA09 (Fig. 3.2). The differences are larger in high latitudes than near the equator. In tropical regions, the absolute differences are not larger than 0.3, the absolute differences in the Nordic Seas, where RFI is present (*ESA, 2012*), are larger than 1. In the vicinity of

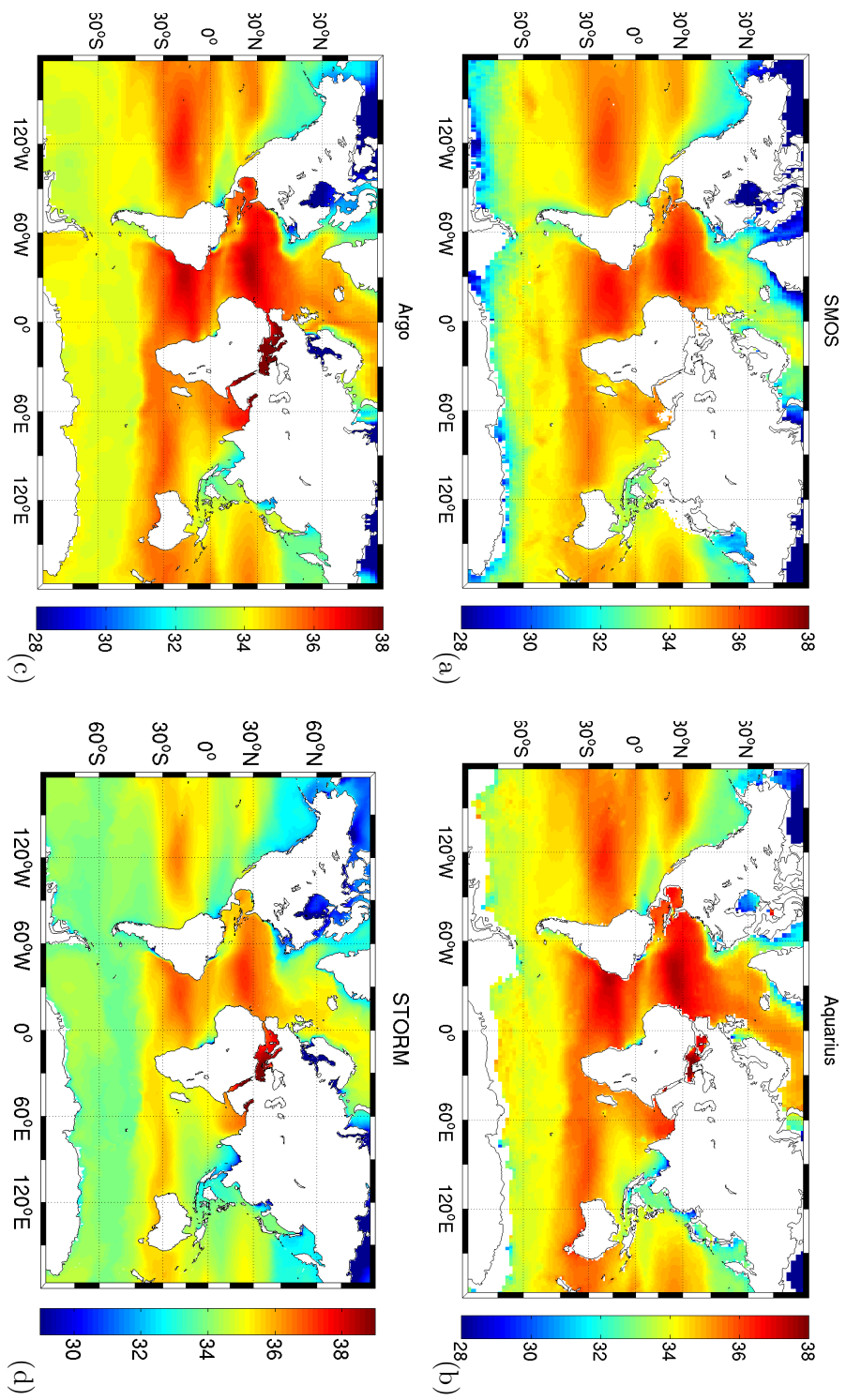


Figure 3.1: Average of (a) SMOS SSS, (b) Aquarius SSS, (c) Argo SSS and (d) STORM SSS for the period from January 2010 to December 2013. Aquarius starting in January 2012

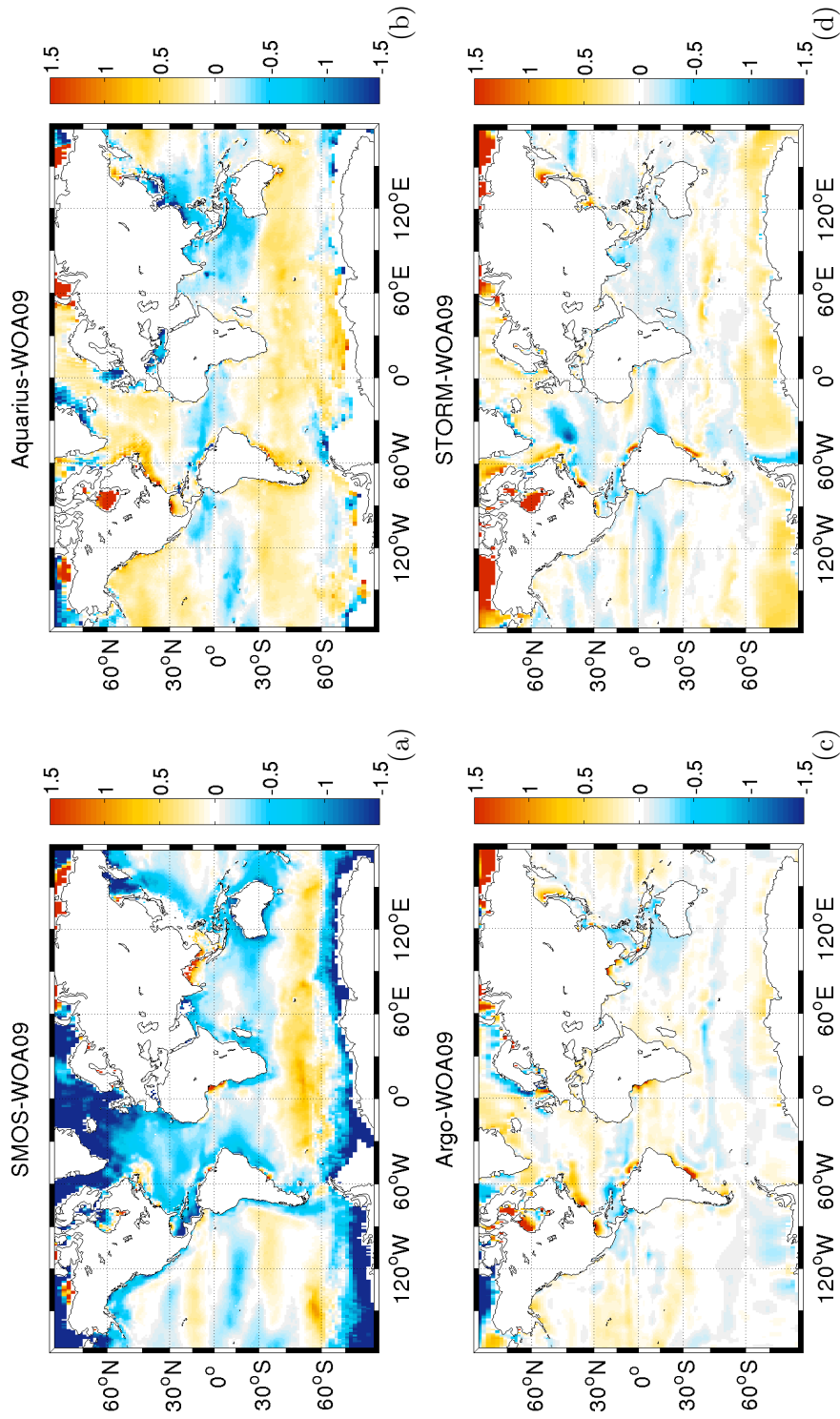


Figure 3.2: Average differences between (a) SMOS SSS, (b) Aquarius SSS and (d) STORM SSS relative to the WOA09 SSS climatology. All averages are for the period of January 2010 to December 2013 except Aquarius where the period starts in January 2012.

coasts, the differences between the satellite and the climatological fields are large reaching values > 1 . This cannot be found in the other datasets. Average differences between Aquarius and WOA09 are slightly positive in high latitudes and negative in the tropics. The differences between Argo SSS and STORM SSS relative to WOA09 are smaller than those for the satellite-retrieved SSS, and show a similar spatial distribution. Here, the absolute differences range from < 0.1 to 0.2 in the central ocean and to approximately 1.5 in high latitudes and along the coasts.

To provide a quantitative assessment of the quality of the observations and model relative to the WOA09 reference, Taylor diagrams are presented in Fig. 3.3. These diagrams show the correlation (COR), the centered root-mean-square difference (RMSD) and the standard deviation (STD) of the different SSS fields relative to the WOA09 field. The data are time-averaged over the 4-year period from January 2010 to December 2013, providing one single value for each grid cell. These values are merged into one dataset, that is then used for the calculation of the statistics. The root-mean-square difference and the standard deviation are normalized by the standard deviation of the reference.

The standard deviation is computed as:

$$\text{STD}(X) = \sqrt{\frac{1}{N} \cdot \sum_{i=1}^N (X_i - \bar{X})^2}, \quad (3.1)$$

where N is the number of data-points, the index i indicates a single value of the considered dataset and \bar{X} represents the average value. The RMSD between observation X and reference Y is calculated as:

$$\text{RMSD}(X,Y) = \sqrt{\frac{1}{N} \cdot \sum_{i=1}^N [(X_i - \bar{X}) - (Y_i - \bar{Y})]^2}, \quad (3.2)$$

The correlation coefficient COR can be expressed as:

$$\text{COR}(X,Y) = \frac{1}{N \cdot \text{STD}(X) \cdot \text{STD}(Y)} \cdot \sum_{i=1}^N (X_i - \bar{X})(Y_i - \bar{Y}), \quad (3.3)$$

The blue dashed lines, originating in the (0,0) point, show the correlation. The normalized standard deviation is represented by the gray dashed lines, whereas the normalized root-mean-square difference is represented by the green dashed lines. A dot between the (0,0) point and the reference indicates that the observation has less variability than the

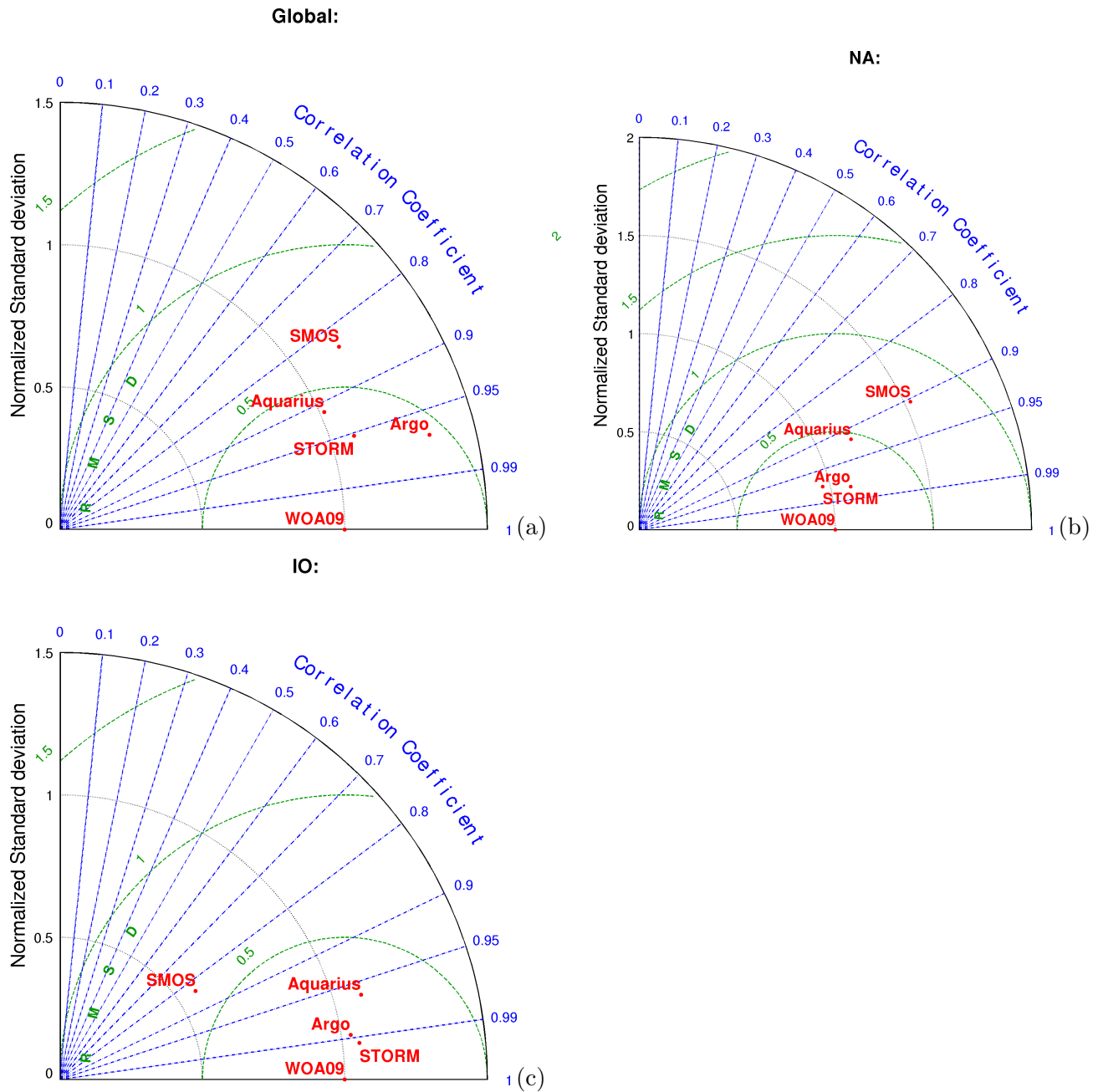


Figure 3.3: Taylor diagram of Aquarius, SMOS, Argo and STORM SSS compared to WOA09 on (a) global scale, (b) in the northern North Atlantic (20°N - 80°N and 75°W - 25°E), and (c) the Indian Ocean (20°S - 20°N and 50°E - 80°E). Standard deviations as well as centered root-mean-square differences (RMSD) are normalized by the standard deviation of the reference WOA09 field.

reference.

On global scale, STORM SSS is closest to WOA09 with a normalized standard deviation of 1.08, a normalized root-mean-square difference of 0.46 and a correlation of 0.95. For Argo and Aquarius, correlation reaches values of about 0.96 and 0.91, respectively. The normalized root-mean-square difference for Aquarius is 0.41. For SMOS, correlation is 0.8, but the root-mean-square difference is 0.64, i.e. twice as high as for Argo. In the northern North Atlantic (Fig. 3.3b, 20°N-80°N and 75°W-25°E), SMOS features the largest differences, with a normalized standard deviation of 1.52 and a normalized root-mean-square difference of 0.74. Here, the correlation between SMOS and WOA09 is 0.9.

STORM and Argo are closest to the reference, with correlations of 0.98 and root-mean-square differences of 0.24 and 0.22, respectively. Aquarius differs from WOA09 with a normalized standard deviation of 1.17, a normalized root-mean-square difference of 0.47 and a correlation of 0.91.

In the Indian Ocean all datasets are closer to the reference field, with root-mean-square differences between 0.13 in the case of STORM and 0.54 in the case of SMOS. The higher root-mean-square difference for SMOS is attributable to the lower data quality in coastal areas. The correlation ranges between 0.83 for SMOS and 0.99 for STORM.

In summary, the validation based on time series of satellite-retrieved, *in situ* and simulated SSS shows that the datasets are often correlated well, but larger differences can be found in regions of lower SST, in coastal areas and especially in the high northern latitudes due to RFI. The observed differences can be caused by various factors, which will be discussed in detail in the next section.

3.2 Northern North Atlantic Ocean

The content of this section is published as a peer-reviewed publication titled "Quality assessment of spaceborne sea surface salinity observations over the northern North Atlantic" by Julia Köhler, Meike Sena Martins, Nuno Serra and Detlef Stammer, published in *Journal of Geophysical Research*, January 2015.

The first region to be investigated in more detail is the northern North Atlantic Ocean from 20°N to 80°N, where warm and saline waters of the North Atlantic Current, originating from the South, interact with cold and less saline waters from the Arctic region (see

Fig. 3.4). The inflow of the North Atlantic Current into the Nordic Seas occurs in three regions (Walczowski, 2014), through the Denmark Strait, over the Iceland-Faeroe Ridge and through the Faeroe-Shetland Channel. The East Greenland Current flows southward along the eastern Greenland continental margin. From the Labrador Sea, the Labrador Sea Rim Current continues southward to Newfoundland (Talley et al., 2011). As described in various studies (e.g. Parry et al. (2007), Rahmstorf (2006)), the exchange of water masses between the Atlantic Ocean and the Nordic Seas by surface currents as well as the overflow of deep water have a strong influence on thermohaline conditions by changing the horizontal and vertical density structure of the upper subpolar North Atlantic and, thus, on the meridional overturning circulation of the Atlantic. Poleward heat transport variations have the potential to make significant changes in the climate system on different temporal and spatial scales (Parry et al., 2007).

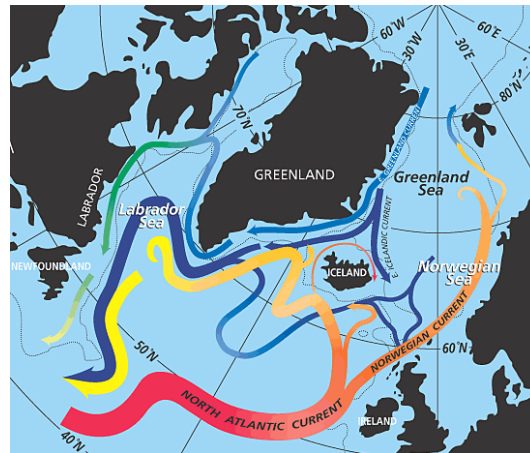


Figure 3.4: Schematic representation of identified current in the norther North Atlantic Ocean. Taken from NASA (http://www.giss.nasa.gov/research/briefs/legrand_01/)

Here, SMOS and Aquarius SSS retrievals are validated against *in situ* salinity observations obtained in cold water regions ($<15^{\circ}\text{C}$) in the subpolar North Atlantic and Nordic Seas during the period from May 2012 to April 2013. SMOS SSS retrievals in the North Atlantic received before May 2012, when major ground-based RFI sources in Canada and Greenland were finally switched off (ESA, 2012), are corrupted by RFI. Together with results from the MITgcm of the North Atlantic and Arctic it will be demonstrated that SMOS and Aquarius satellite data are capable of documenting spatial variations in surface salinity, even in cold water.

In the following, data from ascending and descending SMOS swaths will be analyzed sep-

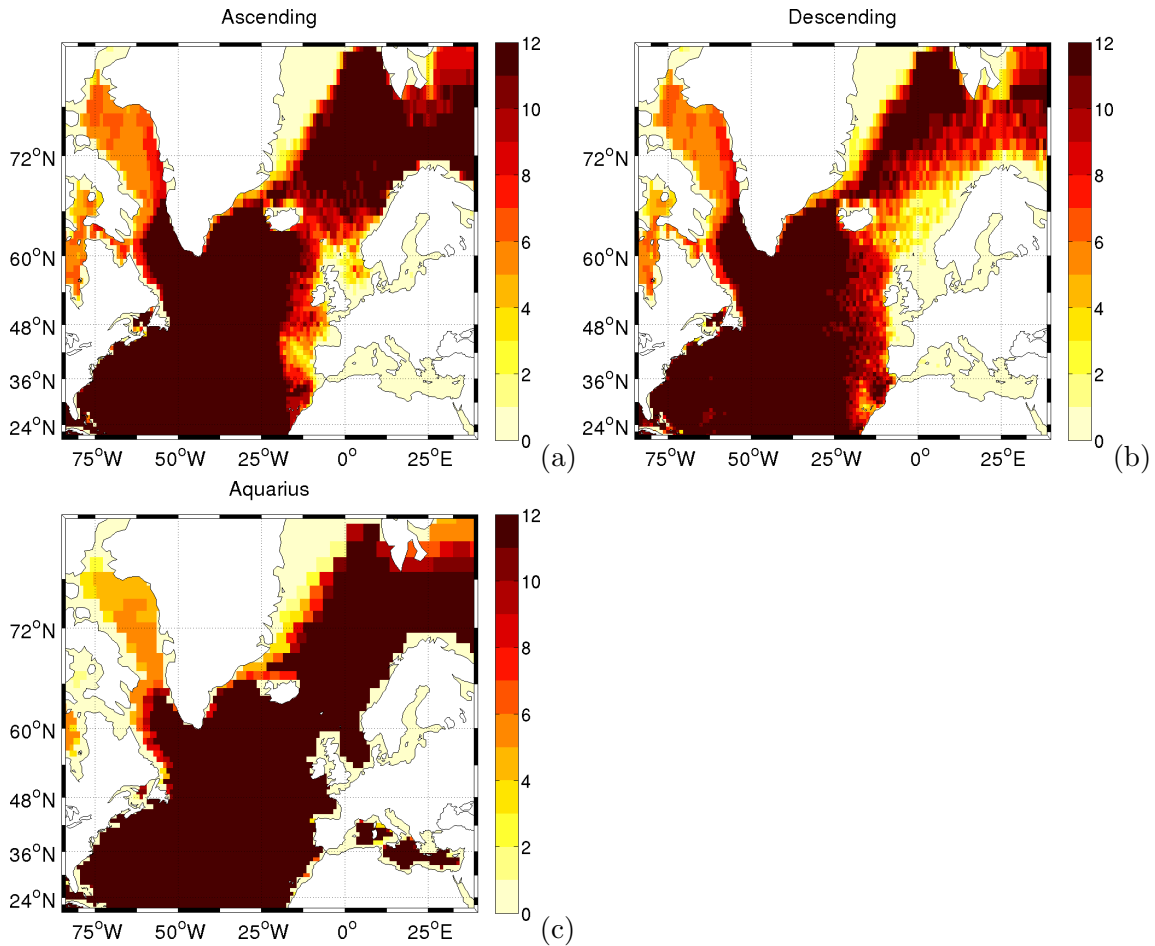


Figure 3.5: Data product availability (in months) during May 2012 to April 2013 for (a) SMOS SSS from ascending orbits, (b) SMOS SSS from descending orbits, and (c) Aquarius SSS

arately, because of large differences in their data quality and in their error characteristics. In particular, significant differences in the quality of the data due to different influences of the ocean-land transition, RFI and sun activity – which in the Atlantic especially degrade data from descending orbits (*Martinez, 2013*) – are expected. As explained by *Font et al. (2013)* and *Gabarro et al. (2012)*, contamination from continents is still a problem when land masses enter the very wide SMOS FOV. Therefore, absolute salinity values within a band of 1500 km around the main continental masses and sea ice edges have to be treated with caution (*Gabarro et al., 2012*). Efforts are under way to further characterize and remove the land-sea contamination over the ocean (*Joe Tenerelli, personal communication,*

and the SMOS Quality Working Group Nr.14).

Figure 3.5 shows the monthly averaged data availability for SMOS ascending and descending orbits as well as Aquarius SSS during the study period from May 2012 to April 2013. Most of the North Atlantic is fully covered during the study period with 12 values per grid box. Exceptions can be found near the eastern coast of Greenland due to ice cover, and in the vicinity of the European continent due to land and/or ice contamination. Active RFI sources from Northern Europe lead to a reduced data availability near the coasts (*Daganzo-Eusebio et al., 2013*), especially for the descending swaths for which the European continent enters the FOV. Data near the coast are contaminated by land effects, e.g., in the European North Sea (Fig. 3.5b). The data availability of Aquarius (Fig. 3.5c) is close to 12 values per grid box, except around Greenland and east of Spitsbergen.

3.2.1 Bias estimation for SMOS salinity retrievals

A typical example of an SMOS ascending SSS retrieval is displayed in Fig. 3.6a, showing the average SSS field for the period from May 2012 to April 2013; the corresponding Aquarius SSS field is shown in Fig. 3.6b. Both fields indicate the subtropical salinity maximum and

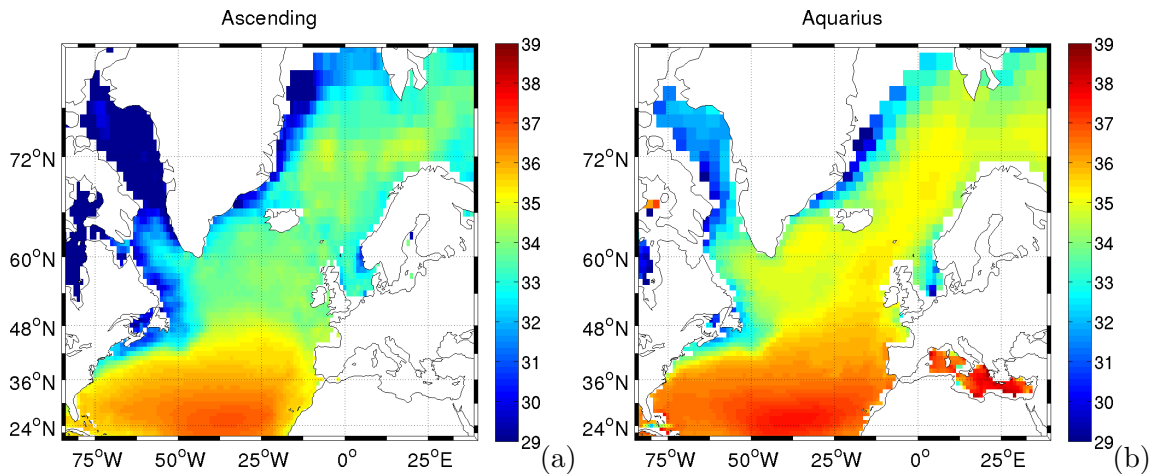


Figure 3.6: Averaged (a) SMOS SSS from ascending orbits and (b) Aquarius SSS for the period from May 2012 to April 2013 after the elimination of a RFI source on Greenland

the spread of high-salinity waters from the subtropics towards the subpolar North Atlantic and even into the Nordic Seas. The low salinities along the Greenland and Icelandic coasts are also well presented. These signals represent the advection of the low-salinity waters of the East Greenland Current originating from the spring-summer sea-ice melting.

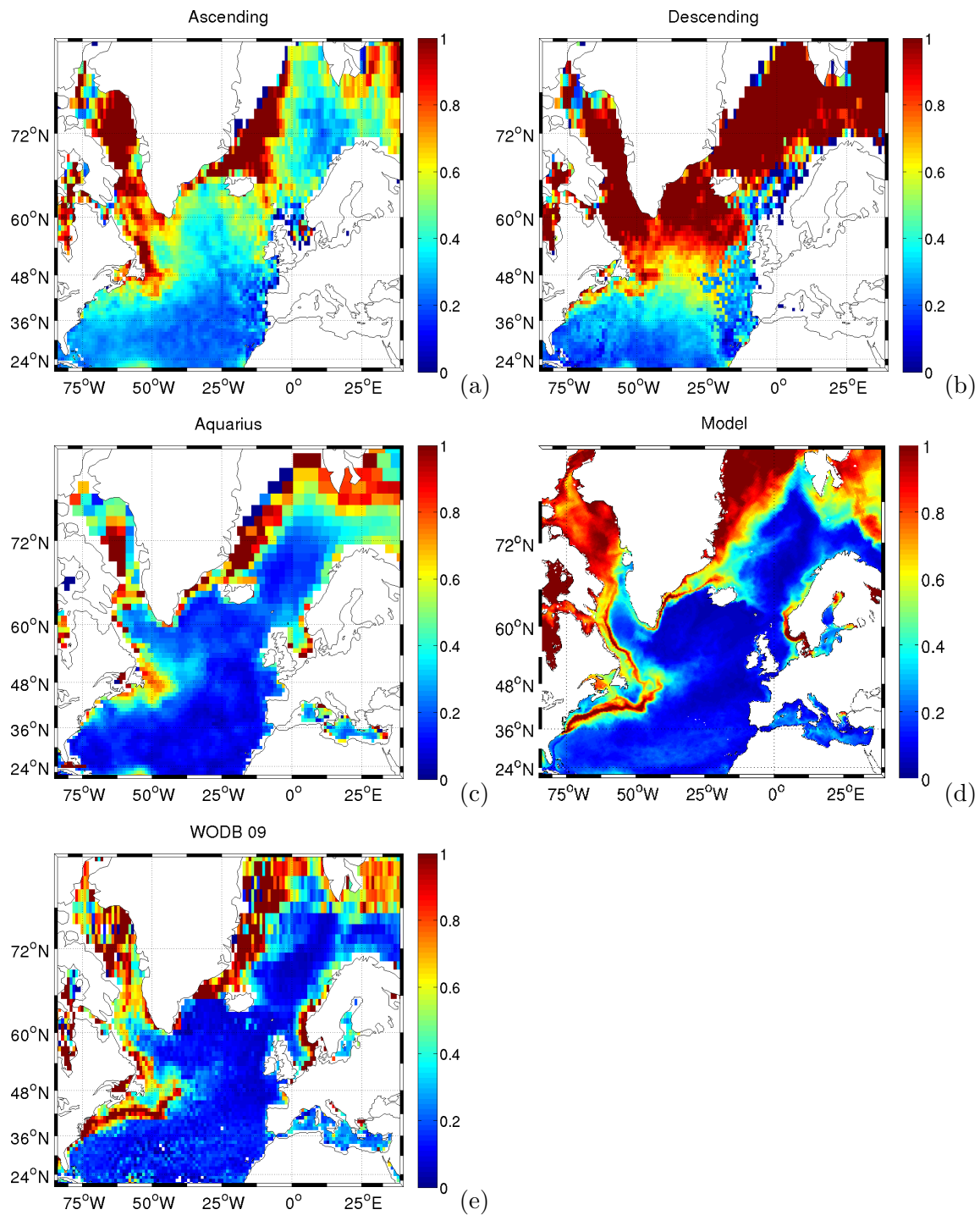


Figure 3.7: Standard deviation of salinity for the period from May 2012 to April 2013 from (a) SMOS ascending orbits, (b) SMOS descending orbits, (c) Aquarius data and (d) from the numerical simulation (at 4 km resolution) between 2005 and 2009 and (e) the salinity standard deviation from WOA09 (Seidov et al., 2010). For a better comparison, the colorbar is saturated.

SMOS shows significantly lower salinities, especially at the eastern edge of the basins and in a band from Iceland to Great Britain. Indeed, the main RFI source in the study area was switched off before May 2012, but thereby weaker RFI sources underneath turned more visible and still lead to an underestimation in the retrieved SSS or data loss (*Daganzo-Eusebio et al., 2013*). The mean difference over the whole study area between both fields is -1.1.

For a quantitative assessment of the quality of the satellite SSS retrievals, the standard deviation in time over the period from May 2012 to April 2013 (including seasonal signals) is computed for each grid point of the SMOS and the Aquarius fields, and the resulting geographic variations of the corresponding standard deviations are compared with the simulated and *in situ* salinity (Fig. 3.7). For SMOS, the standard deviations of SSS are computed separately for ascending and descending swaths. The geographic variability of both the Aquarius SSS standard deviation and the ascending SMOS SSS standard deviation are in good agreement with the model's standard deviation. In particular, both fields show high variability in frontal zones and in the Baffin Bay, Greenland and Barents Seas. Those high variabilities can also be found in the standard deviation of the WOA09 (*Seidov et al., 2010*), reaching values above 1, which reflects the irregular sampling, interannual variability and ice melting near Greenland. Spatial patterns of the *in situ* standard deviation field are very similar to the model's standard deviation field, being the motivation to use model salinities in further analyses. In contrast to the other fields, descending SMOS SSS shows unrealistically high variability, reaching a value of 2.7 over the entire subpolar North Atlantic (not shown, for a better comparison a limitation of the color bar was applied). This is much larger than for any of the other fields and higher than what could be expected from the model results. Averaged over the study area, the SMOS SSS variability from ascending orbits is ~ 0.5 ; over the same area, the Aquarius SSS variability is ~ 0.3 . The SMOS field shows also high variability along the Greenland-Iceland-Scotland Ridge and over large parts of the Labrador Sea, which cannot be found in the Aquarius, *in situ* and in the model STD and probably reflects the influence of land contamination and the impact of RFI sources.

The averaged difference between SMOS SSS and WOA09 salinities are -1.1 and -1.2 for ascending and descending orbits, respectively (Fig. 3.8a,c), pointing to a substantial negative bias in the SMOS retrieval relative to the climatology. The averaged difference of SMOS SSS retrievals relative to the Argo fields is -1.1 and -1.5 for ascending and descending swaths, respectively (Fig. 3.8b,d).

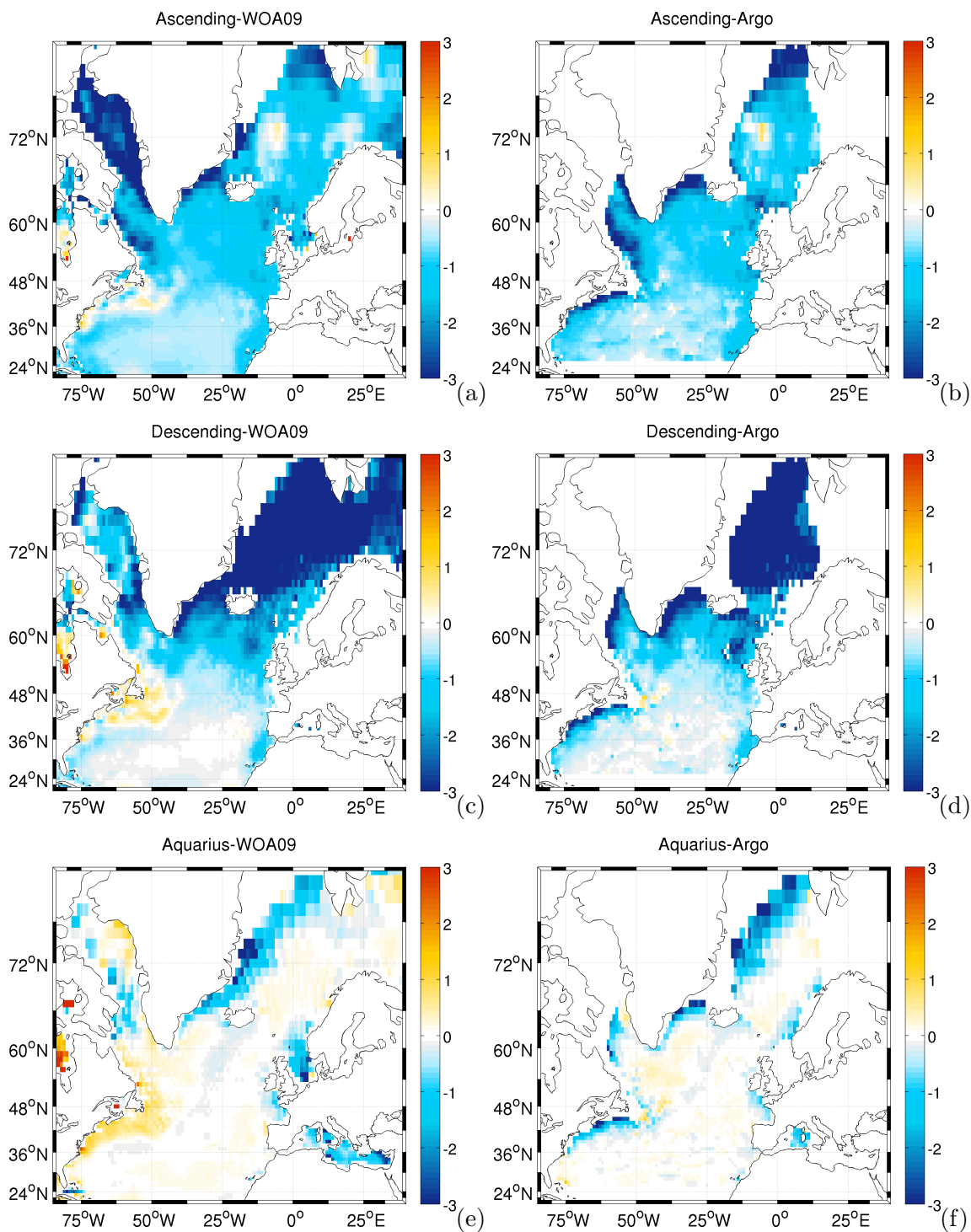


Figure 3.8: Average differences between (a) SMOS ascending SSS and WOA09, (b) SMOS ascending SSS and Argo, (c) SMOS descending SSS and WOA09, (d) SMOS descending SSS and Argo, (e) Aquarius SSS and WOA09, and (f) Aquarius SSS and Argo. All averages refer to the period from May 2012 to April 2013.

In both cases, differences are not uniform in space, but show clear structures with absolute maximum differences (>2) occurring in the vicinity of the cold East Greenland Current and over the Greenland-Iceland-Scotland Ridge. Absolute differences are substantially smaller (< 0.5) in warm subtropical waters (between 25°N and 40°N), suggesting a clear SST bias of the SMOS SSS. Aquarius SSS retrievals are less biased when compared with climatological and Argo data (Fig. 3.8e,f), since an SST-dependent bias was already removed in the Aquarius SSS product (Meissner *et al.*, 2014). Accordingly, the averaged difference over the study area and period between Aquarius SSS and WOA09 is 0.06 and clearly smaller than for SMOS. However, Aquarius SSS are actually positively biased in warm subtropical waters as well as along the North Atlantic Current. In contrast, Aquarius SSS remain negatively biased relative to WOA09 and to Argo fields close to the Greenland coast, suggesting that a small regionally dependent bias remains, which could be due to other error sources. Boutin *et al.* (2014) mentioned that the theoretical error of SMOS SSS mainly depends on the number of brightness temperature data used for the retrieval and on SST. To quantify the dependence of the SMOS SSS bias on SST, Fig 3.9a and b display the salinity differences between SMOS and Argo, separately for ascending and descending orbits, as a function of SST in the region 20°N to 80°N and 85°W to 35°E .

The SST data used in this analysis is an auxiliary product provided by the ECMWF-reanalyzed meteorological fields taken from the original L2 Ocean Salinity User Data Product (UDP). This data, as well as a product description, can be downloaded from <https://earth.esa.int/web/guest/data-access/browse-data-products/-/article/level-2-ocean-salinity-6895>. For the comparison, SST fields were compiled by averaging the original SST values on a $1^{\circ} \times 1^{\circ}$ grid. The differences between satellite-retrieved SSS and Argo salinities are averaged for each SST bin. The resulting median bias and the corresponding standard deviation are shown by the red line and vertical bars in Fig. 3.9a, respectively. The same is done for the differences between satellite-retrieved SSS and WOA09 salinities, indicated by the green line. For SST $>20^{\circ}\text{C}$ the SMOS median bias and the spread of differences tend to diminish (see 3.9a,b, red line). In contrast, for water colder than 5°C , the SMOS ascending median bias reaches -1.8. In the case of the descending SMOS SSS, the median bias is even larger, reaching absolute values of 5 or larger in water colder than 10°C (see 3.9b, red line). Also, the spread of the differences increases in the cold-temperature range. This is especially true for the descending swaths data, that, in this region, are generally more affected from land contamination due to the flight direction of the satellite and different RFI effects.

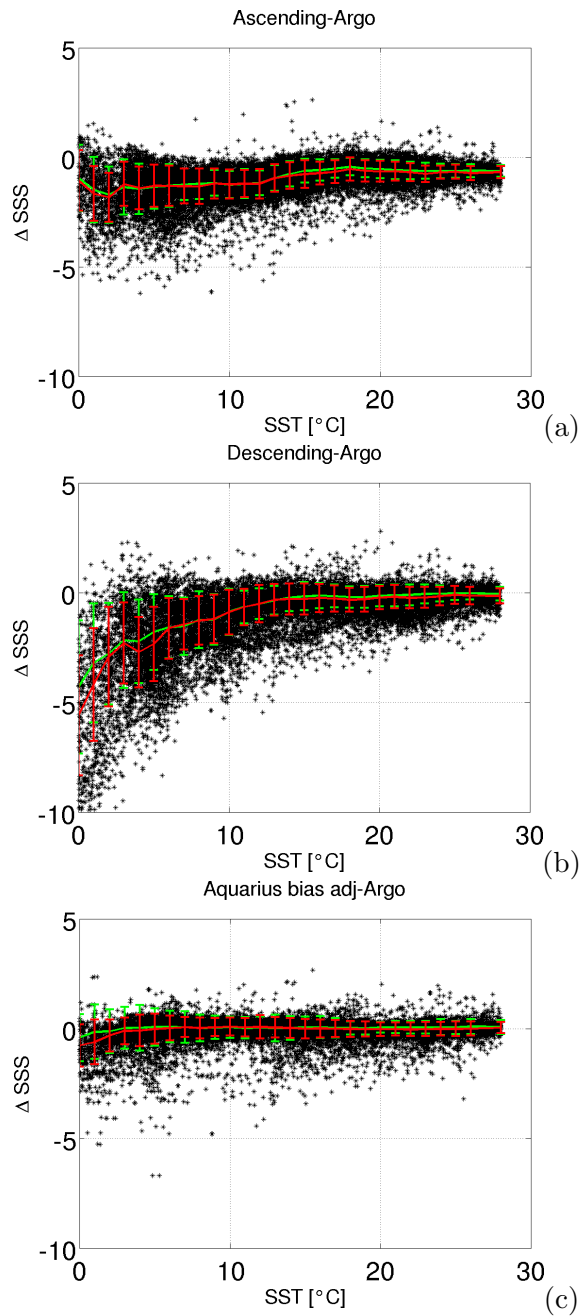


Figure 3.9: Difference between (a) SMOS ascending, (b) SMOS descending and (c) Aquarius SSS retrievals and the Argo salinity for the period from May 2012 to April 2013, as a function of the ECMWF SST between 20°N and 80°N and 90°W and 15°E . A SST-dependent fit based on the median of the differences in 1°C temperature classes is overlaid in red, with the standard deviation of the salinity differences shown by the vertical bars. The SST-dependent fit based on the median of the differences to the WOA09 climatological salinities in 1°C temperature classes is overlaid in green, with the standard deviation of the salinity differences also shown by vertical bars.

Based on these results and the ones shown in Fig. 3.8, the L4 data from the descending SMOS swaths were not considered in further analyses. The standard deviation of SMOS ascending SSS and Argo salinity differences is smaller than the standard deviation for SMOS and WOA09, therefore, the SST-dependent SMOS bias conducted from differences to Argo is used for correcting the SMOS L4 product. In the remaining study, this bias was subtracted from the SMOS L4 product. Also shown in Fig. 3.9c are the salinity differences between Aquarius and Argo as a function of SST for the same region and period as before. The Aquarius bias does not differ significantly from zero and is slightly negative only below about 4 °C. Therefore, no bias correction was performed in this study in addition to what was already applied by the Aquarius project processing.

3.2.2 Processes affecting the differences between satellite and *in situ* salinities

Many factors can cause the differences between satellite retrievals and *in situ* data and can especially lead to larger differences as shown in Fig. 3.9. To some extent those larger differences between SMOS and WOA09 fields can be attributed to a substantial under-sampling of the climatological salinity data (i.e. an increased uncertainty in the WOA09 data), but also to the presence of variability on all timescales, which is expected to be significant in this region due to varying freshwater input resulting from sea ice or land ice melting. However, it has to be considered that some of the SMOS data were obtained in the vicinity of frontal structures, where temporal and spatial SSS variability is large (see Fig. 3.7, e.g. East Greenland Current between Greenland and Iceland, Labrador Sea Rim Current) and, therefore, sampling errors are likely to occur. Associated processes can be linked to (i) temporal frontal and/or eddy-related variability, and/or (ii) vertical near-surface salinity gradients. In this context, one also has to keep in mind that monthly SMOS SSS fields provided from BEC are constructed by averaging data from 7-day repeats (only ascending swaths) on a $0.25^\circ \times 0.25^\circ$ grid, which were spatially smoothed by interpolating them onto a $1^\circ \times 1^\circ$ grid. On the other hand, *in situ* data represent instantaneous point-wise measurements sampled at just a few positions or only once along ship tracks (TSG data) and averaged along-track (nominally over 100 km segments). Due to the average sampling rate of Argo floats of only one sample every 10 days nominally on a $3^\circ \times 3^\circ$ grid (*Tang et al., 2014*) (in our study region the sampling is substantially worse), that dataset is not adequate to resolve small-scale variations in SSS. Consequently, the differences between satellite and *in situ* data can at least partially result from different spatial and temporal

sampling of the strongly varying ocean SSS field, thereby leading to strong aliasing of SSS variability. In this sense, differences do not necessarily represent satellite data errors.

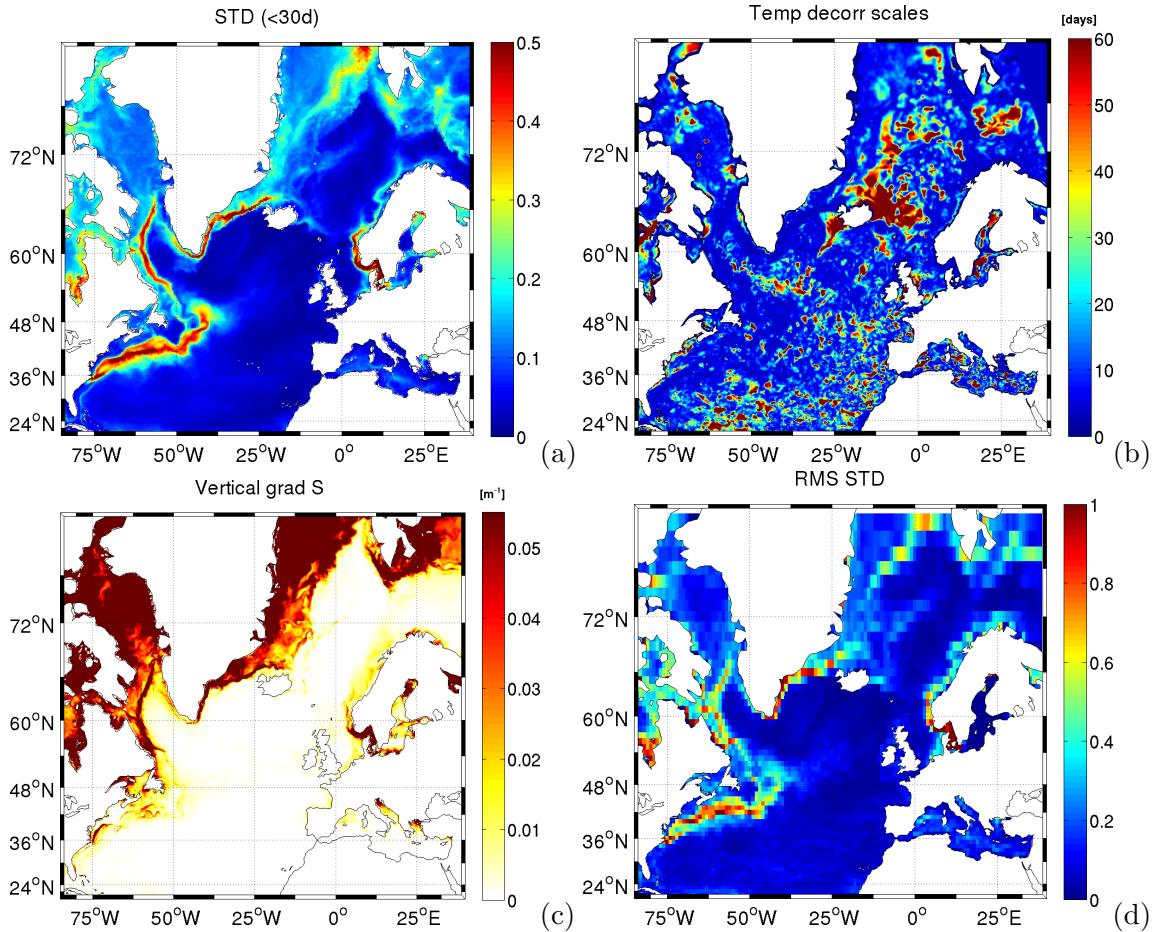


Figure 3.10: (a) Standard deviation of model SSS (with the seasonal cycle removed) on timescales smaller than 30 days. (b) Temporal decorrelation scales computed from the model SSS (with the seasonal cycle removed). (c) Simulated mean vertical salinity gradient between 2.5 m and 7.5 m depth. (d) Root-mean-square difference of all daily $1^\circ \times 1^\circ$ grid box standard deviations, which is the sampling RMSD

To quantify the potential impact of small-scale variability on the diagnosed salinity differences between SMOS and *in situ* measurements, the standard deviation of the daily averaged near-surface (at 2.5 m depth) salinity field output from the model after high-pass filtering, thus retaining only fast salinity variations with timescales smaller than 30 days, was analyzed. As expected, high-frequency salinity variations are enhanced in the vicinity

by frontal structures (e.g. north of the Gulf Stream) and close to the coast of Greenland, north of Iceland and within the East Greenland Current in the Irminger Sea (Fig. 3.10a). This also holds true for the East Greenland Current, suggesting that the enhanced satellite minus *in situ* differences in this area partially result from eddy processes being aliased in the non-synchronously sampled observational data. To determine how quickly the surface salinity field can change in a given time frame, Fig. 3.10b shows the temporal SSS decorrelation timescales computed as an e-folding decay timescale inferred from model salinity autocorrelation functions based on daily data (from which a temporal average and a seasonal cycle were eliminated). The results suggest that along the East Greenland Current salinity anomalies can decorrelate in just a few days, highlighting again the sampling problem in these regions. However, in the interior basin, the decorrelation scales are substantially longer, approaching 30 days or more in some places and thereby making aliasing less problematic here. While this estimation might still be optimistic relative to the real world (because of a potential underrepresentation of high-frequency processes in the model), it yields a useful estimate of what can be expected.

Since SMOS and Aquarius measurements are representative only for the top centimeter of the ocean, any vertical salinity gradient in the upper few meters can lead to a difference between satellite retrievals and Argo or ship-based observations, usually taken at approximately 4 m depth or below. To quantify salinity differences arising from a vertical gradient in salinity in this study area, a near-surface salinity gradient from the numerical simulation using the model fields at 2.5 m and 7.5 m depth (Fig. 3.10c) was estimated. Results suggest that in this study area vertical gradients over this depth range can be as large as 0.05 m^{-1} , with the largest vertical gradients occurring close to the coast of Greenland and in the East Greenland Current frontal zone. Assuming that gradients between the top centimeter of the ocean and 4 m depth are of the same order, these gradients could result in differences of up to 0.2 between satellite and *in situ* data. *Boutin et al. (2013)* and *Henocq et al. (2010)* found that precipitation events over the tropical oceans lead to vertical salinity gradients of up to 0.5 m^{-1} over the upper 10 m. *Boutin et al. (2014)* studied the signature of rainfall with SMOS and drifter observations and found that, averaged over one month, the rain-induced surface salinity decrease is at most 0.2 and up to 40% of the difference between SMOS and interpolated *in situ* salinity near the ITCZ. However, due to the sparsity of simultaneous *in situ* measurements during rain events and SMOS data, *Boutin et al. (2014)* could not reach a conclusion about the vertical gradient between the top centimeter of the water column and 4-5 m depth, where the uppermost Argo and TSG measurements are placed. *Drucker and Riser (2014)* validated Aquarius L2 SSS against Argo salinities and

analyzed the error due to the depth of measurements and vertical salinity stratification. They came to the conclusion that insufficient collocation (horizontally and vertically) is not the most significant problem for the validation. Instead, they found that heavy rainfall can result in vertical differences up to 1 (over the top 0-5 m). However, significant stratification events occurred in < 13% of their data (between 50°S and 50°N); therefore, the produced bias is much smaller than currently achievable L-band radiometric accuracies (*Drucker and Riser, 2014*). Vertical salinity gradients extracted from the model fields are in a good agreement with those found in data from more equatorial areas, although they are smaller. Nevertheless, it is assumed here that vertical salinity gradients in the study area would not be a primary source of the difference diagnosed between satellite-retrieved and *in situ* observations.

Regarding the aliasing of horizontal eddy-related SSS signals, *Vinogradova and Ponte (2013)* examined how much of a difference can be expected between *in situ* salinity and Aquarius-retrieved SSS on the basis of their different sampling of spatial variability. To simulate the Aquarius footprint, daily salinity values from HYCOM were averaged by the authors onto a $1^\circ \times 1^\circ$ grid; the standard deviation within each box then represents the small-scale variability for every day of the year. Results indicate that in some areas of the ocean, small-scale variability can be an important source of sampling errors for *in situ* measurements in regions with strong horizontal salinity gradients such as coastal areas, river outflows and along strong frontal structures, where a sampling error of up to 0.2 was diagnosed. From a similar computation, but based on the MITgcm output (Fig. 3.10d), the conclusion drawn by *Vinogradova and Ponte (2013)* can be confirmed, but uncertainties with values of 1 are substantially larger than those previously reported.

Beside processes in the ocean or biases of *in situ* data, a suite of remaining errors in satellite retrievals can also lead to differences relative to *in situ* data. As described in *Oliva et al. (2013)*, the main error sources in SMOS measurements are antenna pattern, antenna loss, receiver and correlation errors. The antenna pattern errors can cause sidelobes and spatial ripples, which are the dominant contributor to land-sea and ice-sea contamination, as well as sun and RFI tails spreading through the image (*M. Martin-Neira et al., personal communication, April 2013*). The resulting increase of the signal, again, leads to an increase of the brightness temperature and therefore to lower SSS values (*Oliva et al., 2012*). Therefore, SSS retrievals around continents have to be treated with caution, and absolute salinity values are often erroneous. In addition, temporal drifts caused by, e.g. the strong influence of reflected solar radiation or by instrumental drifts due to the evolution of the antenna temperature within a year (*Kainulainen et al., 2012*), as well as short term drifts

(Yin *et al.*, 2013) are also potential error sources.

3.2.3 Validation of corrected salinity retrievals against TSG observations

In principle, all of the above-mentioned error sources need to be considered when interpreting the differences between satellite and *in situ* SSS. Many of these biases show a correlation with geographically changing SSS fields. Apparently, their influence can be reduced by removing an SST-dependent bias from the SMOS data. In the following, one question is of interest: How reliable are the resulting bias-corrected data?

For a quality assessment of the bias-corrected SMOS SSS retrievals, Fig. 3.11a shows the differences between the SMOS and Aquarius fields and the independent *in situ* TSG salinity observations. The differences are calculated as the difference between monthly averaged salinity fields from the satellites and the instantaneous *in situ* data averaged during the corresponding month on the same grid. The size of the shown circles indicates the number of data pairs available in the period from May 2012 to April 2013. Large differences still remain in the East Greenland Current region and along the Labrador Sea Rim Current, where the SMOS differences show negative and positive differences of roughly equal amplitude and on spatial eddy scales as they can be expected from eddy aliasing. The presence of similar differences for the Aquarius fields (Fig. 3.11c) supports this conclusion. Further east, biases in both datasets tend to diminish. Individual fluctuations of ± 0.5 can be attributed to land-sea, ice-sea and RFI contamination. Consistent with previous findings (Section 3.2.2), areas of large differences between TSG and satellite-retrieved SSS correspond to areas of short decorrelation timescales. This suggests that at least some of these differences may result from aliasing of the eddy SSS signal in the TSG data. Large differences and short decorrelation timescales can be found, for example, in the East Greenland Current, Labrador Sea Rim Current and south of Spitsbergen (Fig. 3.10b). However, close to the Greenland coast, it is difficult to isolate the aliasing influence from other influences such as land contamination. Nevertheless, the similarity between SMOS and Aquarius differences suggests that the SMOS data have been improved in a very similar efficient way through the SST-related bias correction. The remaining bias (red bars) and the remaining uncertainty in the data of SMOS and TSG differences are shown in the histograms in Fig. 3.11b. Also included in the figure are SSS errors prior to the bias correction (blue bars), illustrating a shift of the peak in the histograms toward a zero mean, which demonstrates that the bias correction was able to remove the offset in this region.

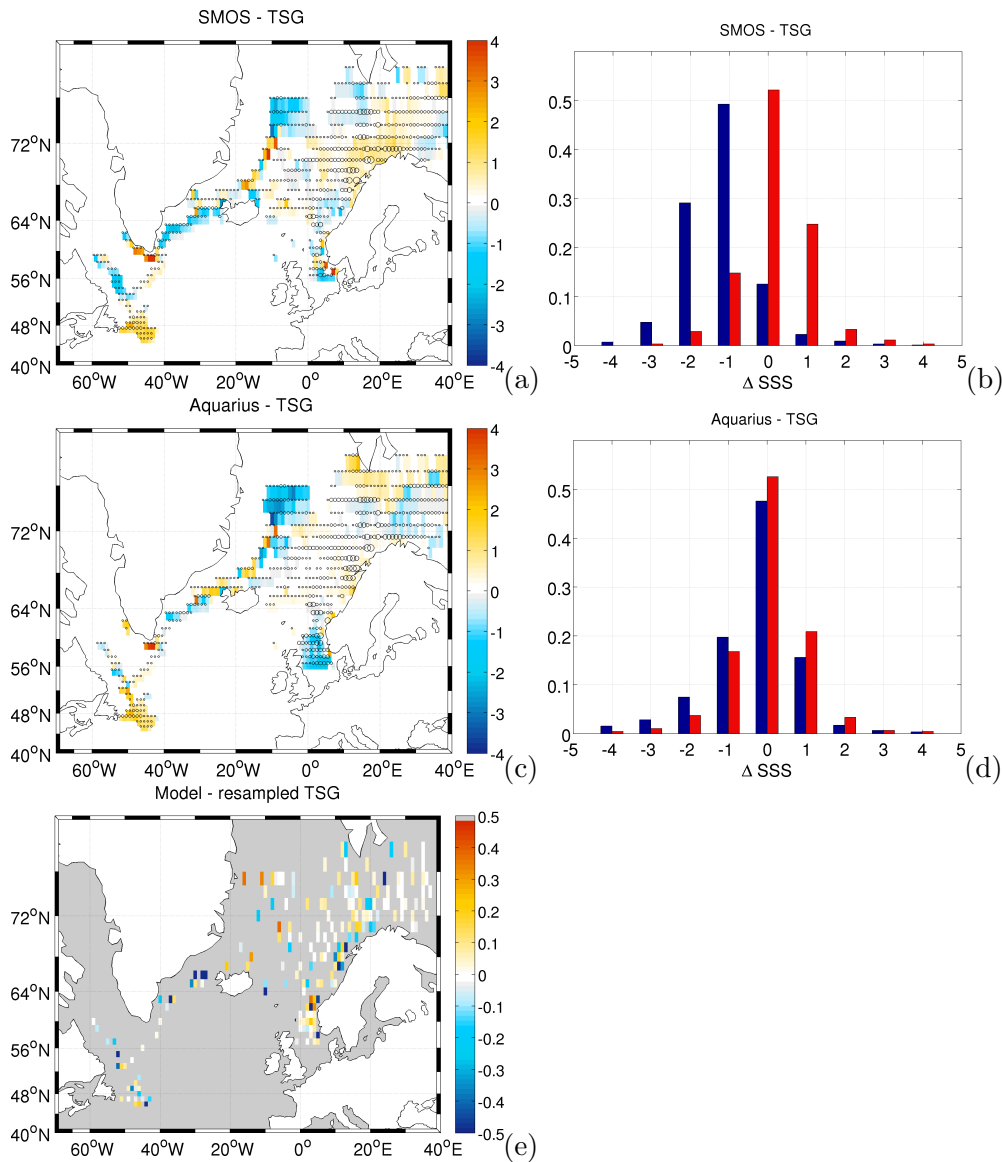


Figure 3.11: Mean differences between $1^\circ \times 1^\circ$ gridded satellite-retrieved SSS and $1^\circ \times 1^\circ$ gridded in situ TSG salinity for the period from May 2012 to April 2013 (where data was available): (a) using the bias-corrected SMOS SSS ascending orbits, and (c) using the Aquarius SSS. Dots correspond to one data pair and the largest circles to eleven pairs. Histograms of mean differences between $1^\circ \times 1^\circ$ gridded (b) SMOS SSS ascending orbits and TSG salinities before (blue) and after (red) the bias correction was applied and (d) Aquarius V2.0 SSS (blue) and Aquarius V3.0 bias adjusted SSS (red) and TSG salinities. (e) Mean differences between $1^\circ \times 1^\circ$ gridded model salinity and $1^\circ \times 1^\circ$ gridded model salinity resampled at the TSG locations.

Table 3.1: *Statistics of satellite-retrieved SSS minus TSG salinities before and after bias correction*

Data product	Mean	STD	RMSD
SMOS L4	-1.2	0.9	1.5
SMOS $L4_{bias-corr}$	0.1	0.9	0.9
Aquarius V2.0	-0.5	1.6	1.7
Aquarius V3.0 SSS_{ba}	0.02	0.9	0.9

The SMOS bias could be reduced from -1.2 to 0.1, and the root-mean-square difference was reduced from 1.5 to 0.9 through the bias correction. However, the standard deviation of the differences remains high with 0.9. The statistics of SMOS SSS minus TSG salinities before and after bias correction are summarized in Table 3.1. The mode of the histogram of the differences between Aquarius V3.0 SSS_{ba} and TSG (Fig. 3.11d, red) is almost zero (averaged difference is 0.02), but the root-mean-square difference of 0.9 is very similar to the SMOS root-mean-square difference value. The earlier version (V2.0) of the Aquarius Level 3 data (shown in blue), that was not SST bias corrected, shows a negative bias up to 3 in cold waters. This tends to diminish for waters warmer than 8°C. Here, the median bias is negative and reaches an absolute value of 0.5 in cold waters, which can be attributed to other error sources like land-sea contamination. The standard deviation of the differences was reduced from 1.6 to 0.9 between Aquarius V2.0 and V3.0 (compare Table 3.1), illustrating again the improvement resulting from the SST bias correction. The correlation of satellite-retrieved SSS to TSG is 0.6 for both, SMOS and Aquarius.

Here, monthly averaged TSG and satellite values are compared. Therefore, monthly standard deviations cannot be estimated. To investigate how representative monthly averaged gridded TSG data are for the total monthly salinity average within one grid box, the model daily averaged salinities were resampled at the TSG positions, averaged to the same spatial and temporal grid and compared with the total gridded model salinity field (Fig. 3.11e). Large averaged differences imply that the gridded TSG values probably do not capture the total SSS. Differences are higher than 0.5 close to the Scandinavian coast and in frontal zones in the western part of the study area. The root-mean-square over all differences is 0.38, with the highest values in coastal areas with high variabilities. There, the validation results have to be considered with caution. Large differences between satellite and *in situ* data can be attributed to sampling errors in the TSG measurements. However, more *in*

situ data are needed to allow a more detailed statement. It could be helpful to consider the differences of individual measurements rather than gridded values (*Boutin et al. (2013)* and *Vinogradova and Ponte (2013)*). In this case, it would be difficult to find SMOS or Aquarius SSS and *in situ* samples collocated within short timescales and spatial scales in the study area and period.

3.2.4 Annual cycle of monthly salinity anomalies

The amplitude of the annual cycle of salinity was calculated by *Martins et al. (2014)* from the same 4 km resolution model output analyzed in this study as well as from gridded *in situ* data. The amplitude is largest (> 1) in the rim of the Baffin Bay, Labrador Sea and Greenland Sea. Changes in sea-ice coverage and associated brine rejection during ice formation have a direct effect on SSS in these areas. Increased amplitudes of the annual cycle along the rims of the Labrador Sea and in the Greenland Sea are caused by the advection of water from ice-covered areas (*Boyer and Levitus, 2002*). The annual signal reaches large values (> 1) along the East and West Greenland Currents and along the rim of the Labrador Sea. A high amplitude seasonal cycle can also be found off the Scandinavian coast, in the areas of Baltic Sea outflow, and in the North Sea due to freshwater runoff. The phase (year day of maximum SSS) of the annual cycle is centered in fall and winter in the East Greenland Current and Labrador Sea Rim Current. Because satellite data are still subject to seasonally varying biases, they are not yet qualified for a quantitative estimate of the seasonal cycle.

To demonstrate the benefit SMOS SSS fields may provide even for studies of salinity variability in the subpolar Atlantic, Fig. 3.12 presents selected monthly salinity anomalies (relative to the annual average) and compares them to salinity anomalies derived from the eddy-resolving simulation and Argo floats. Shown are monthly SMOS SSS anomalies for May, August, October and January between May 2012 and April 2013, SST bias-corrected, and monthly Aquarius anomalies for corresponding months and study period. While the satellite-retrieved salinities and the Argo salinity fields are from 2012-2013, the model fields are from 2005-2006. Interannual changes in the salinity anomaly fields result from a different amount of ice melting in different years. These changes reach up to 0.5 along the northern ice edges in winter, in the eastern rim of the East Greenland Current during summer months and along the North Atlantic Current (not shown). However, the period 2005-2006 was chosen because a simultaneous model output is not available, but it is quite well comparable to the fields of 2012 and 2013 Argo salinity anomalies and

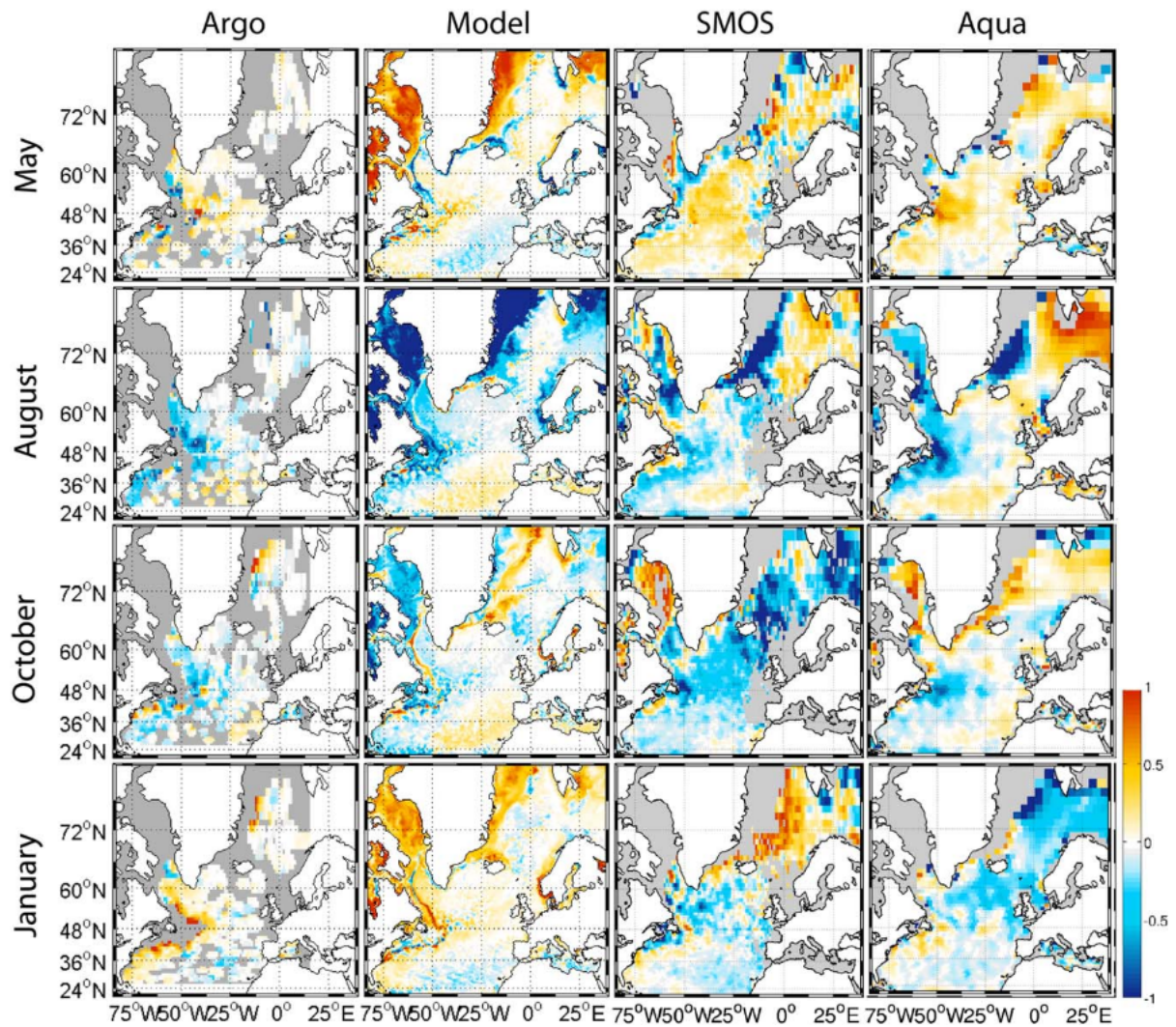


Figure 3.12: Monthly salinity anomalies from (first column) the Argo floats, (second column) the 4 km resolution model, (third column) the $1^\circ \times 1^\circ$ gridded and bias corrected SMOS ascending SSS, and (fourth column) the $1^\circ \times 1^\circ$ gridded Aquarius SSS. Shown are the months of May, August and October 2012 and January 2013 (in the model case 2005 and 2006), respectively. Negative anomalies up to -1 are shown in blue, positive anomalies up to 1 in red. Color scale is saturated. Dark gray shading indicates no data.

helps to interpret those *in situ* fields. The substantially degraded spatial resolution in the Argo fields clearly underlines the large potential of satellite SSS data in describing monthly salinity variations with significantly improved spatial details.

Starting in May, the model shows high positive salinity anomalies below the sea-ice due to brine rejection during the freezing period. Negative anomalies are found at the ice edge in the Nordic Seas and along the East Greenland Current, continuing around the Labrador Sea into the Labrador Current. In general, the North Atlantic region shows positive anomalies north of 40°N but negative anomalies in the eastern subtropics. The SMOS field captures the positive anomalies, and the negative anomalies along the northeastern rims, however, there seems to be a consistently positive anomaly during May. The Aquarius SSS compares well with that from SMOS, except along the Norwegian coast and around Great Britain, where Aquarius' positive anomalies tend to better agree with the model.

In August, negative model anomalies reflect the advection of the freshwater input during the melting season in the whole western North Atlantic. In the western subtropics the negative anomalies can be associated with other processes like advection from the south (*Yu, 2011*) and in the eastern subtropics positive anomalies indicate the summer salinity maximum forced by horizontal advection and vertical entrainment (*Qu et al., 2011*). Both satellite-retrieved salinity fields show the negative anomalies in the Greenland Sea, the Iceland Sea, the Labrador Sea and the region of the Gulf Stream/North Atlantic Current. Furthermore, both products show the positive salinity anomalies in the eastern subtropics. The main difference between SMOS and Aquarius occurs over the eastern part of the Greenland-Iceland-Scotland Ridge, where Aquarius shows positive anomalies while SMOS shows negative anomalies. In this case, the latter is in better agreement with the model.

In October, at the beginning of the freezing season, positive model anomalies can be found at the ice edge due to processes like brine rejection (can be represented by the model fields but not by the satellite fields). The *in situ* data also show positive anomalies in the western part of the Greenland Sea. Negative anomalies still dominate in the western part of the North Atlantic, and positive values are seen in the southeastern Atlantic. Turning to the SMOS salinity anomalies, the start of the freezing season is represented, and also slightly positive anomalies in the eastern subtropics are shown. However, the October field is negative in the remaining domain. The Aquarius salinity anomalies agree reasonably well with the model and Argo anomalies. However, in the Barents Sea Aquarius anomalies are positive, whereas the model and SMOS point to negative anomalies.

The January salinity anomalies are mainly opposite to those in August, with positive model anomalies during the freezing season under the ice due to brine rejection. Also, the salinity anomalies are positive at the ice edge and along the western rim of the study region around the Grand Banks of Newfoundland. The negative phase of the annual salinity cycle can be found in the subtropics, in accordance to the Argo salinity anomaly field. While both SMOS and Aquarius are in a good agreement in the eastern subtropics and off the Grand Banks, the salinities are quite different in the Nordic Seas, where SMOS tends to agree better with the model results.

3.2.5 Concluding remarks

This study shows, that relative to ship-based *in situ* salinity measurements, the SMOS and Aquarius SSS fields reproduce spatial and temporal structures of the SSS during the period from May 2012 to April 2013. Overall, the L4 SMOS salinities are lower than climatological and *in situ* salinities, especially in cold-water regions. The quality can be improved through an SST-dependent bias correction derived empirically as a relation (in space and time) between satellite and Argo data in the North Atlantic (Latitude $>20^{\circ}\text{N}$). The SMOS L4 SSS descending swath data appear substantially corrupted in the North Atlantic and were not considered in the later analyses of this study. After the removal of the SST-dependent bias, the offset between SMOS SSS and independent TSG salinity observations taken in the Nordic Seas and subpolar North Atlantic is notably reduced. However, the differences between satellite and *in situ* data in colder waters remain high. Results are likely to be further improved by using longer time series.

Aquarius overestimates SSS in warm subtropical waters and along the North Atlantic Current in comparison to climatological and *in situ* observations; but the biases are more than 1 smaller than for SMOS, since it was previously corrected through an SST-dependent bias correction. After applying a bias correction to SMOS, one can find better agreements between satellite SSS retrievals and *in situ* fields. The applied bias correction method is confirmed by the similar differences between Aquarius and independent TSG observations. With an equivalently improved retrieval algorithm that reduces the negative SMOS SSS bias in cold waters, the elimination of lingering land contamination in the SMOS SSS field and longer time series from SMOS and Aquarius, one will be able to study changes in salinity over all parts of the world ocean. This will allow a more precise computation of freshwater transports as well as surface freshwater fluxes between ocean and atmosphere. Despite the unprecedented *in situ* Argo salinity sampling, spatial structures remain poorly

resolved in contrast to the satellite retrievals. Therefore, satellite-retrieved SSS need to be part of our sustained long-term climate observing system.

A quantitative study of potential errors in this region is a problematic task, as isolating each type of bias is difficult. In some regions, particularly in regions of large freshwater input like the Greenland shelf, local differences between satellite salinities and *in situ* salinities can be attributed, at least partly, to temporal variability of the location of salinity fronts. *Köhl et al. (2014)* present an alternative approach to infer biases in satellite SSS retrievals, using a dynamically consistent assimilation methodology. Different SMOS SSS products have been developed by several institutions and similar analyses using other SMOS products (not shown) lead to different results, attributable to different strategies for error correction. *Zhang et al. (2013)* compared two SMOS products (BEC L3 and CATDS V02) with Argo measurements and showed that both products perform well in the open tropical oceans; but close to coasts and in higher latitudes, the biases are high. The reasons for using the BEC L4 product in the present study are, on the one hand, the availability of data in the study period and, on the other hand, that frontal structures are potentially better represented, which is of special importance in the study area.

The model simulation gives insight into realistic levels of salinity variability, on the impact of oceanographic processes on the latter, and it supports the deduction of sampling errors in the observations. The quality of the model estimates, however, is affected by errors in the atmospheric forcing, the lack of high-frequency forcing, the lack of resolution for certain subgrid-scale processes, the assumption behind their parameterizations and by natural internal ocean variability.

In an overall sense, this study suggests that even in cold waters the satellite SSS retrievals show reasonable skill in observing changes of the ocean surface salinity. To draw a reliable conclusion, more studies like the one presented are required to determine the quality of the satellite SSS data over all parts of the global ocean and to help improve the inversion algorithms. A problem for improving satellite SSS retrievals in high latitudes is the lack of *in situ* measurements, required for validation and correction of the satellite retrievals. To what extent a sampling error affects the validation results, is an important point for further studies. The results are based only on a study period of one year; the analysis of a multi-year period and more *in situ* measurements in the higher northern latitudes would be helpful to test the robustness of the validation results. In the best case, one would be tempted to use only single satellite-based samples as well as individual *in situ* samples in order to minimize collocation errors, but data pairs of SMOS or Aquarius SSS and *in situ*

samples collocated within short timescales and spatial scales are sparse. Therefore, an up-to-date, global, uniform and quality-checked database of *in situ* measurements, especially TSG sections, would be an asset.

3.3 Indian Ocean

The Indian Ocean is the smallest of all oceans but forms a major part of the largest warm pool on Earth (Schott *et al.*, 2009). Different to the Atlantic and Pacific, the Indian Ocean is bound to the North by the Asian continent, which prevents northward oceanic heat transport (Schott *et al.*, 2009). Three mediterranean seas influence the hydrography of the Indian Ocean: the Persian Gulf, the Gulf of Oman and the Red Sea (Tomczak and Godfrey, 2003). The northern Indian Ocean consists of two basins – the Arabian Sea (AS) in the western part and the Bay of Bengal (BOB) in the eastern part (see Fig. 3.13) – with different hydrographic properties discussed in more detail in Section 3.3.1.

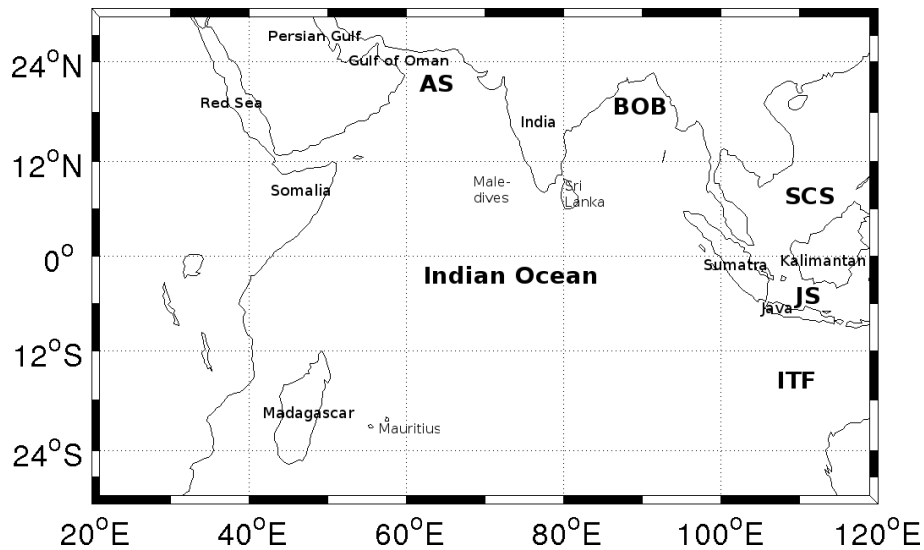


Figure 3.13: Northern and tropical Indian Ocean: Arabian Sea (AS), Bay of Bengal (BOB), South China Sea (SCS), Java Sea (JS) and Indonesian Troughflow (ITF). South-east Asia, comprising Indonesia, the Philippines and Papua New Guinea is named as the maritime continent.

The Indian Ocean is connected to the Pacific via the South China Sea (SCS) and the Java Sea (JS).

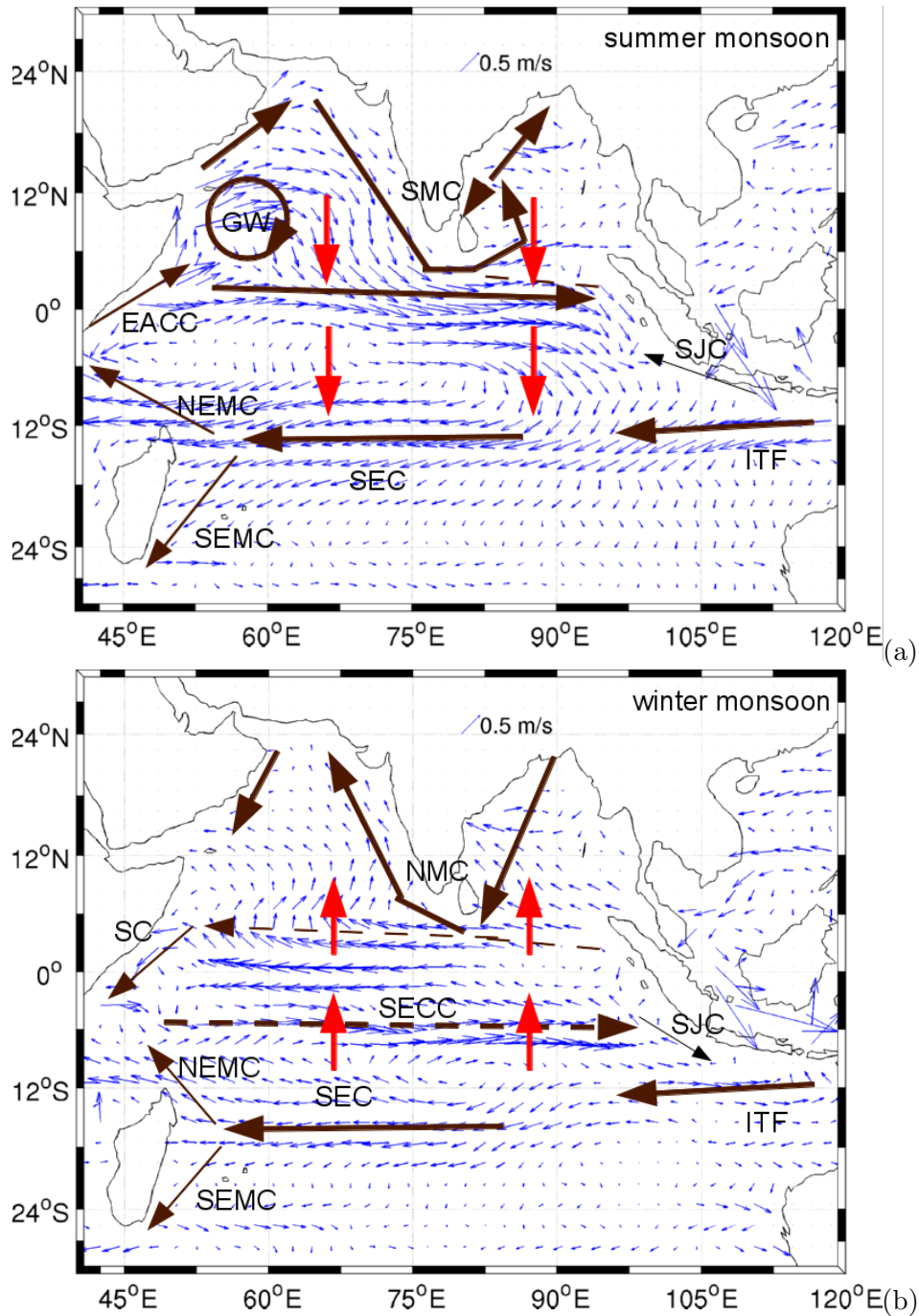


Figure 3.14: Schematic representation of surface currents during (a) summer monsoon and (b) winter monsoon. Currents: South Equatorial Current (SEC), Indonesian Through-flow (ITF), Great Whirl (GW), East African Coastal Current (EACC), South Java Current (SJC), Northeast and Southeast Madagascar Current (NEMC and SEMC), Southwest and Northeast Monsoon Current (SMC and NMC). Red vectors show directions of the meridional Ekman transport. Blue arrows show the OSCAR surface currents.

Various studies showed, that monsoonal climate dominates the northern Indian Ocean, and the seasonal reversals of the monsoon play a critical role in regional ocean-climate processes (*Nyadjro and Subrahmanyam (2014), Sakova (2010), Schott et al. (2009)*). Figure 3.14 shows the current system in the IO during summer and winter monsoon. The seasonal reversing monsoon winds generate large seasonal variations in ocean currents. The Southwest or summer monsoon determines the climate of the northern Indian Ocean during boreal summer (July/August). Asian landmasses heat up and generate a low-pressure area over the continent and strong winds from the Southwest, which results in the eastward Southwest Monsoon Current (SMC). In boreal winter, the Indian Ocean dynamic is determined by the Northwest or winter monsoon – winds blowing from the northeast – which is followed by the current reversal from the SMC to the westward Northeast Monsoon Current (NMC). These seasonal current reversals dominate the water mass exchange north of 4°N.

The zonal water transport in equatorial regions is controlled by strong eastward surface jets referred to as Yoshida-Wyrtki Jets (*Schott et al., 2009*). The South Equatorial Current (SEC), supplied by the Indonesian Throughflow, is the westward part of the large-scale subtropical gyre, driven by the Southeast trade winds. These trade winds persist throughout the year south of 10°S with a shift to the north during boreal summer and fall and a shift to the south in boreal winter and spring (*Sakova (2010), Schott et al. (2009)* and *Tomczak and Godfrey (2003)*). Upwelling occurs off Northeast Africa, the Arabian Peninsula, India as well as at the northern edge of the trade winds. Upwelling is generated by wind as well as by remotely forced Rossby and Kelvin waves (*Sakova, 2010*). Weak upwelling occurs off the coast of Sumatra and Java. Here, strong upwelling can occur, which is associated with a climate anomaly known as the Indian Ocean Dipole (*Sakova (2010), Schott et al. (2009)*) and discussed in detail in Section 4. A detailed description of the current system in the IO can be found in *Sakova (2010), Schott et al. (2009)* and *Tomczak and Godfrey (2003)*.

3.3.1 Spatial salinity distribution

To validate the satellite-retrieved SSS, the annual average is compared with Argo data, the STORM simulations and WOA09 climatology for the period from January 2010 (January 2012 in the case of Aquarius) to December 2013 (Fig. 3.15).

All datasets show similar patterns with low salinities in the east (South China Sea, Gulf of Thailand), in the Bay of Bengal and Indonesian Throughflow and high salinities in the

Arabian Sea and south of 20°S . The generally low SSS in the Bay of Bengal and high SSS pattern in the Arabian Sea are a result of precipitation and river runoff exceeding evaporation in the Bay of Bengal and vice versa in the Arabian Sea.

Low salinity waters extend westwards south of $\approx 10^{\circ}\text{N}$, and higher salinity waters propagate to the East along the equator. For SMOS, the SSS is still underestimated at the western edge of the basin, with an average SSS of 35.2 in the Arabian Sea.

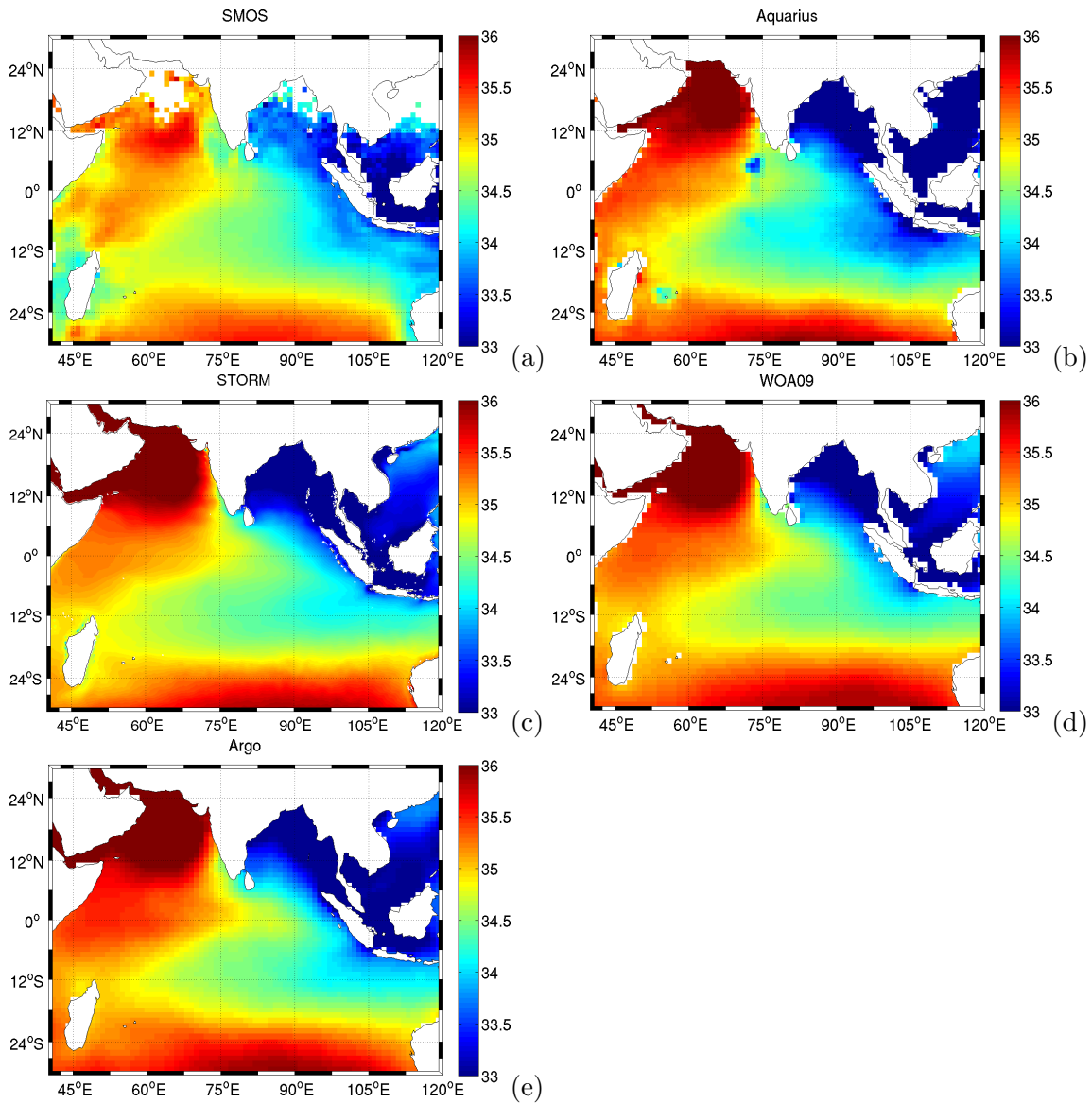


Figure 3.15: Annually averaged SSS for the period from 2010 to 2013 from (a) SMOS, (b) Aquarius, (c) STORM SSS, (d) WOA09 and (e) Argo

In the Bay of Bengal, the SSS seems to be overestimated with values of about 33.7. Aquarius SSS in the Arabian Sea is 35.8 and 32.3 in the Bay of Bengal.

The systematic underestimation in SMOS SSS retrievals can be attributed to RFI sources in the study area (*Daganzo-Eusebio et al., 2013*). No salinity retrievals are available in a band (several hundred kilometers) around landmasses. This can also be caused by RFI sources and the influence of land contamination (compare BEC L4 product description in Section 2.1.1).

Remarkable are also lower salinities north/northwest of Mauritius/La Réunion (20°S; 57°E) and close to Australia, which cannot be found in the Argo salinity fields. The Aquarius field shows lower salinities at the position of the Maldive Islands (2°N; 73°E) and Mauritius/La Réunion, which is unrealistic and likely due to the influence of land. The STORM salinity field is in good agreement with the Argo and WOA09 fields showing similar SSS patterns.

3.3.2 Spatial distribution of salinity variability

For a quantitative assessment of the quality of the satellite SSS retrievals, the variabilities are computed. Figure 3.16 shows the total standard deviation of the SMOS and Aquarius fields over the period from January 2010, respectively, January 2012 to December 2013. These fields are compared with the resulting geographic variations of corresponding amplitudes of the STORM SSS, WOA09 and Argo standard deviation fields. The distribution of the variabilities obtained from SMOS and Aquarius SSS is in agreement with the variabilities of Argo and climatological data. The maxima of the variabilities coincide spatially. All fields show high variability near the coast, in the Bay of Bengal and southern Arabian Sea around the Maldive Islands. The latter is dominated by seasonal reversal of flow patterns due to the monsoon cycle, which will be discussed in detail in the following chapter. Also, higher variability can be found in a band south of the equator until 12°S. Overall, the variability of SSS is more distinct in the northern Indian Ocean than in the southern Indian Ocean due to strong seasonality in the hydrological forcing and monsoon-driven reversal of the near-surface circulation (*Rao and Sivakumar, 2003*).

In the case of SMOS, higher variability can be found in the South China Sea (5°N; 110°E), but cannot be found in the Aquarius or Argo standard deviation field. This can be attributed to the above-mentioned error sources. Higher variability off Sumatra and Java can also be observed in the SMOS standard deviation field and corresponds well to the variability observed by Argo.

The spatial variability of the Aquarius SSS standard deviation is in good agreement with the standard deviation of Argo SSS. In particular, both fields show high variability in the Bay of Bengal, southwest of India, Java Sea and south of the equator until 12°S . The latter can also be found in the other datasets, but not as strong as in Aquarius and Argo. Remarkable are also higher variabilities in Aquarius around La Réunion and Mauritius which cannot be found in any other datasets, possibly reflecting land contamination. STORM reproduces the spatial patterns of the observed variability.

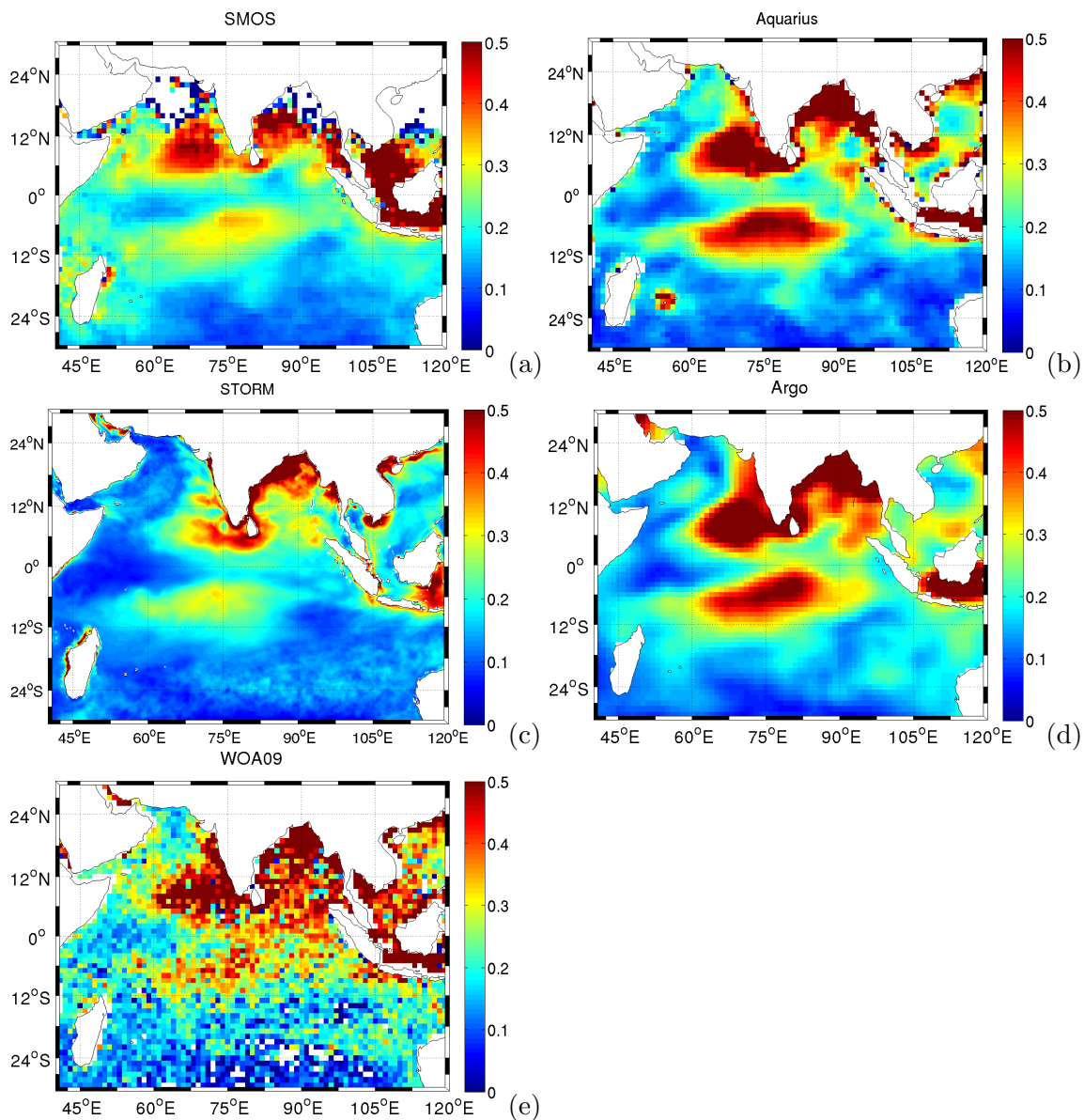


Figure 3.16: SSS STD for the period from January 2010 (2012 for Aquarius) to December 2013 from (a) SMOS, (b) Aquarius, (c) STORM, (d) Argo and (e) WOA09

Furthermore, high variabilities at the major river outlets in the Bay of Bengal and in the South China Sea are reflected. Different to the other fields is the lower amplitude in a band south of the equator and also in the Bay of Bengal and southwest of India.

Averaged over the study area, the SMOS SSS variability is ~ 0.2 , while the Aquarius SSS variability is ~ 0.3 . High variabilities can also be found in WOA09. A detailed description of SSS variabilities on different timescales will be given in the following chapter.

3.3.3 Validation of satellite salinity retrievals

The satellite-retrieved SSS were compared with climatological and *in situ* salinity fields (Fig. 3.17). Averaged over the study area, the annual-mean difference of the SMOS SSS and WOA09 reaches absolute values of 0.4. The absolute difference of SMOS SSS and Argo is 0.17 (Fig. 3.17b). In both SMOS comparisons, spatial patterns are similar and show clear structures with larger positive differences in the Bay of Bengal and South China Sea and larger negative differences in the Arabian Sea and in Australian coastal regions. Differences are substantially smaller ($< |0.1|$) far away from the coast, suggesting a distance to coast-dependent bias (Fig. 3.18), which results from RFI. Difficulties in resolving SSS along coastal regions furthermore relate to land contamination and to strong salinity gradients on small spatial scales which cannot be resolved by SMOS. Therefore, differences between satellite and *in situ* SSS in the Bay of Bengal and southern Arabian Sea can also be attributed to sampling errors, that are an important error source in regions of large small-scale variability (compare Section 3.2.2 and (Vinogradova and Ponte, 2013)).

Differences to WOA09 and Argo in the equatorial region and also in the upwelling region off Sumatra and Java are < 0.1 .

Aquarius SSS retrievals are negatively biased when compared with WOA09 and Argo data (Figs. 3.17c, d). The absolute differences averaged over study area and period are small, with 0.3 for WOA09 and 0.2 for Argo, respectively. Here, the SSS seems only slightly negatively biased in the western part of the Indian Ocean. In the eastern part of the basin, the differences are larger, suggesting a small regionally dependent bias. High negative differences can be found around small islands like the Maldives and Mauritius/La Réunion due to land contamination (Fig. 3.17c,d). Averaged differences of STORM and WOA09, respectively, Argo and WOA09 are positive in the South China Sea, negative in the Bay of Bengal and around zero in the western part of the Indian Ocean. Overall, these differences are smaller than the ones between satellite-retrieved SSS and *in situ* salinities.

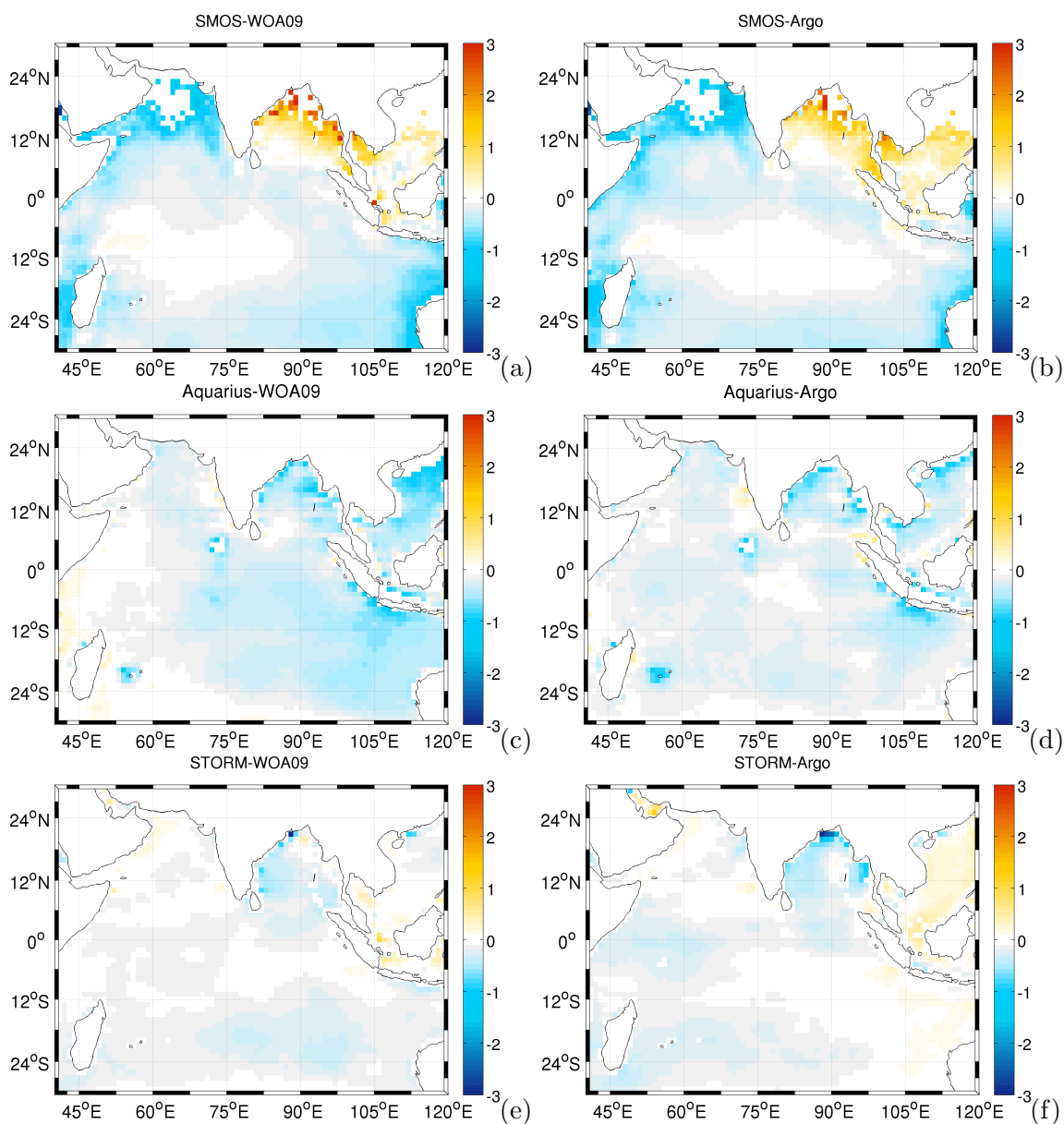


Figure 3.17: Average differences between (a) SMOS SSS and WOA09, (b) SMOS SSS and Argo SSS, (c) Aquarius SSS and WOA09, (d) Aquarius SSS and the Argo SSS, (e) STORM SSS and WOA09, and (f) STORM SSS and Argo SSS.

The average difference between STORM SSS and WOA09 and between STORM SSS and Argo is 0.16 and -0.07, respectively (Figs. 3.17e,f).

A comparison of SMOS and Argo SSS as a function of the distance to coast (Fig. 3.18a) demonstrates that for distances to the coast larger than 1000 km, the differences tend to

diminish. In contrast, in a band of about 500 km around landmasses, differences can be >1.5 . Also shown are the differences between Aquarius and Argo as a function of the distance to coast (Fig. 3.18b). Aquarius SSS fields are also affected by land contamination, but this contamination is reduced to a region of about 150 km in width around continental margins due to its smaller FOV (*Kim et al., 2014*). Here, absolute differences reach 2 for distances of ~ 150 km.

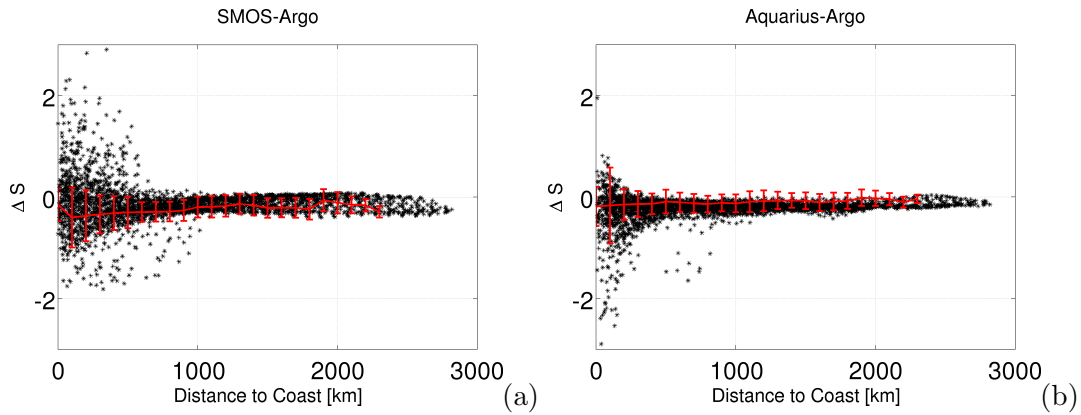


Figure 3.18: Difference between (a) SMOS SSS and Argo SSS, and (b) Aquarius SSS and Argo SSS for January 2012 till December 2013, as a function of the distance to coast between $10^{\circ}S$ and $30^{\circ}N$ and $50^{\circ}E$ and $100^{\circ}E$. A distance to coast-dependent fit based on the median of the differences in 100 km classes is overlaid in red, with the standard deviation of salinity differences shown by the vertical bars.

A harmonic analysis was performed in order to obtain the amplitudes of the annual cycle AC . AC is described by an amplitude A_k and phase ϕ_k of a harmonic and is determined via a cosine fit to the time series from January 2010 (January 2012 in the case of Aquarius) to December 2013 of each grid cell with a period of $\tau = 12$ months. The AC can be written as:

$$AC = A_k \cos(\omega t + \phi_k) \quad (3.4)$$

with

$$\omega = \frac{2\pi}{\tau} \quad (3.5)$$

The Taylor diagram in Fig. 3.19 summarizes statistical measures of the annual cycle's quality in the Indian Ocean, described by the different datasets compared to the annual

cycle of WOA09. The standard deviations and root-mean-square differences are normalized by the standard deviation of the reference WOA09.

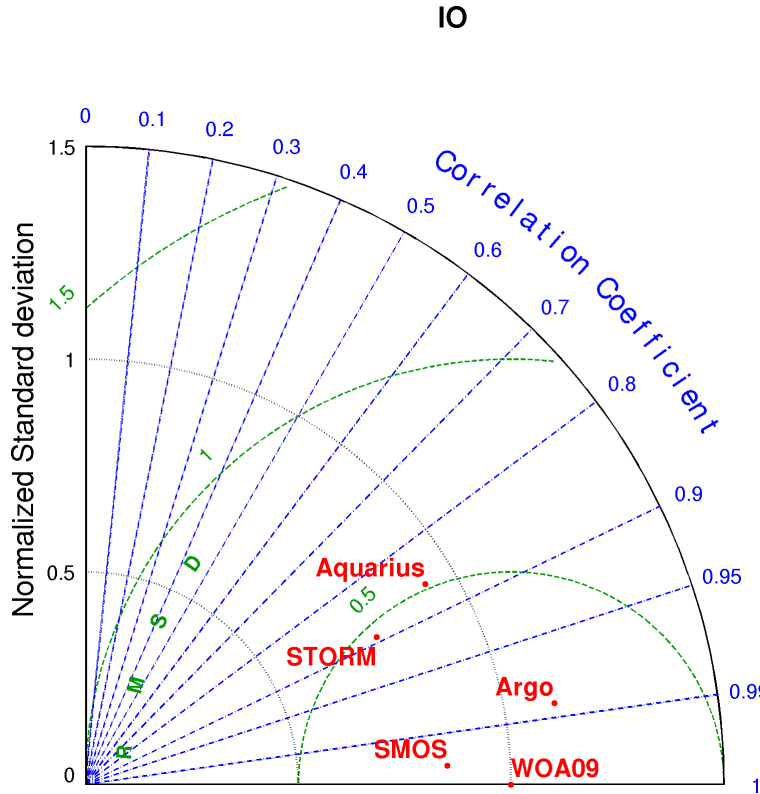


Figure 3.19: Taylor diagram for the annual cycle of salinity in the Indian Ocean ($20^{\circ}S$ - $20^{\circ}N$ and $50^{\circ}E$ - $80^{\circ}E$) observed by SMOS, Argo, Aquarius and STORM compared with the climatological WOA09 annual cycle. Standard deviations as well as centered root-mean-square differences (RMSD) are normalized by the standard deviation of the reference WOA09 field.

The statistics for the different datasets confirm the good agreement between the satellite data, *in situ* observations and model and the climatological WOA09 field shown in Fig. 3.16. For both SMOS and Aquarius, the correlation reaches high values of 0.99 and 0.86, respectively. The normalized root-mean-square difference is small with 0.14 for SMOS and 0.21 for Argo. In the case of Aquarius, the root-mean-square difference yields 0.51, but the normalized standard deviation is 0.92. Only two years of Aquarius data were analyzed, whereas WOA09 represents the annual cycle computed from more than 50 years.

In summary, the validation shows that SMOS and Aquarius reproduce the main temporal and spatial features well. SMOS and Aquarius data are useful for scientific studies of SSS

variabilities in the tropical Indian Ocean, especially in regions far away from the coast. Differences to Argo are less than 0.1 in equatorial regions and the upwelling region off Sumatra and Java. Therefore, the following chapter will analyze in detail low-frequency SSS variability in the Indian Ocean and discuss the control mechanisms.

Chapter 4

Driving mechanisms of seasonal and interannual SSS variability in the Indian Ocean

The previous chapter showed that the satellite-retrieved SSS fields reproduce realistic spatial and temporal variations. In higher latitudes, the SMOS SSS is negatively biased primarily due to the lower sensitivity of brightness temperature to SSS, the influence of RFI and land contamination. The differences to climatological and *in situ* data decrease with lower latitudes.

The different SSS fields reproduce the annual cycle of the climatological field in the tropical Indian Ocean well. In the following, the annual cycle as well as year-to-year variabilities of the salinity in the Indian Ocean and their causes are examined by combining *in situ* observations and remotely sensed measurements.

4.1 Salinity variability

This study focuses on salinity variability of the Indian Ocean from annual to interannual timescales. The annual and semiannual cycle are the subject of various studies (e.g. *Sakova (2010)*, *Schott et al. (2009)*, *Rao and Sivakumar (2003)*, *Schott and McCreary (2001)*, *Masumoto and Meyers (1998)* and *Donguy and Meyers (1996)*) and are briefly summarized in the following section. The main characteristics of interannual variability are discussed in Section 4.1.2, and a detailed analysis of the year-to-year variability's driving mechanisms

is given in Section 4.2.

4.1.1 Annual cycle

As shown by *Rao and Sivakumar (2003)* most of the variability of SSS in the Indian Ocean is explained by the first two harmonics of the observed annual cycle. Spatial patterns of annual amplitude are a result of the interaction between ocean and atmosphere.

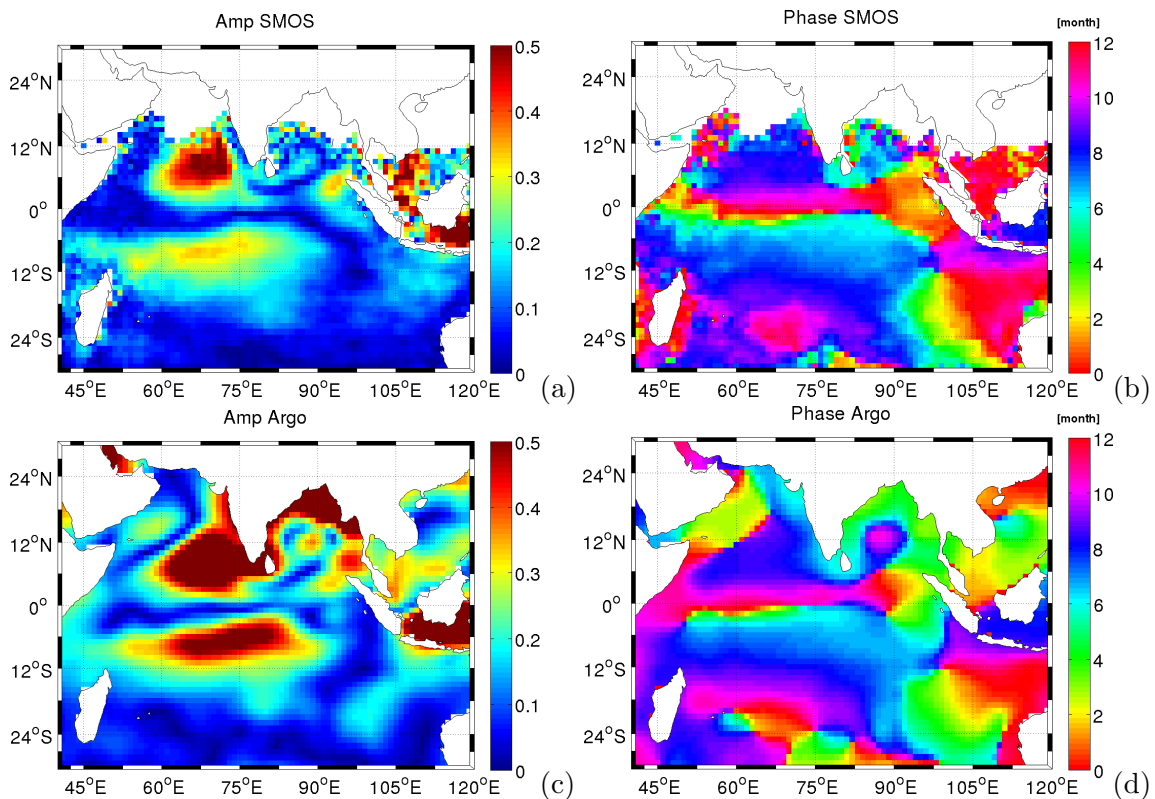


Figure 4.1: Amplitude and phase of the annual harmonic generated from (a,b) SMOS SSS and (c,d) Argo

Figure 4.1 shows the amplitude and phase of the annual cycle obtained from SMOS and Argo SSS. Winds and current patterns completely reverse north of 10°S due to the monsoon cycle. South of 10°S, the southeast trade winds are present during the whole year, although with a significant annual cycle (*Schott and McCreary, 2001*). The northern edge of the southeast trade winds shifts northward during summer and retreats poleward during winter. This is represented by the large annual SSS amplitude in a band around 10°S. The amplitude of the annual cycle reaches values of approximately 0.5 and 0.3 in the case of

Argo and SMOS, respectively.

Large annual amplitudes (≈ 0.5) can be found in the coastal regions of the Bay of Bengal, where high precipitation (P) and river runoff govern the variability (see Fig. 4.2a). These high annual amplitudes are not shown in SMOS, as no data are available close to the coasts. *Shankar (2004)* and *Brandt et al. (2002)* showed that the large annual amplitude in the Arabian Sea between 6°N and 10°N is due to the westward propagation of annual Rossby waves, which radiate from the western coast of India and forced from the Bay of Bengal and by the action of wind stress curl over the Arabian Sea. Both, Argo and SMOS show the large annual amplitude in the southern Arabian Sea. Low saline waters flow from the Bay of Bengal into the Arabian Sea during the northeastern (winter) monsoon phase, thereby lowering the salinity.

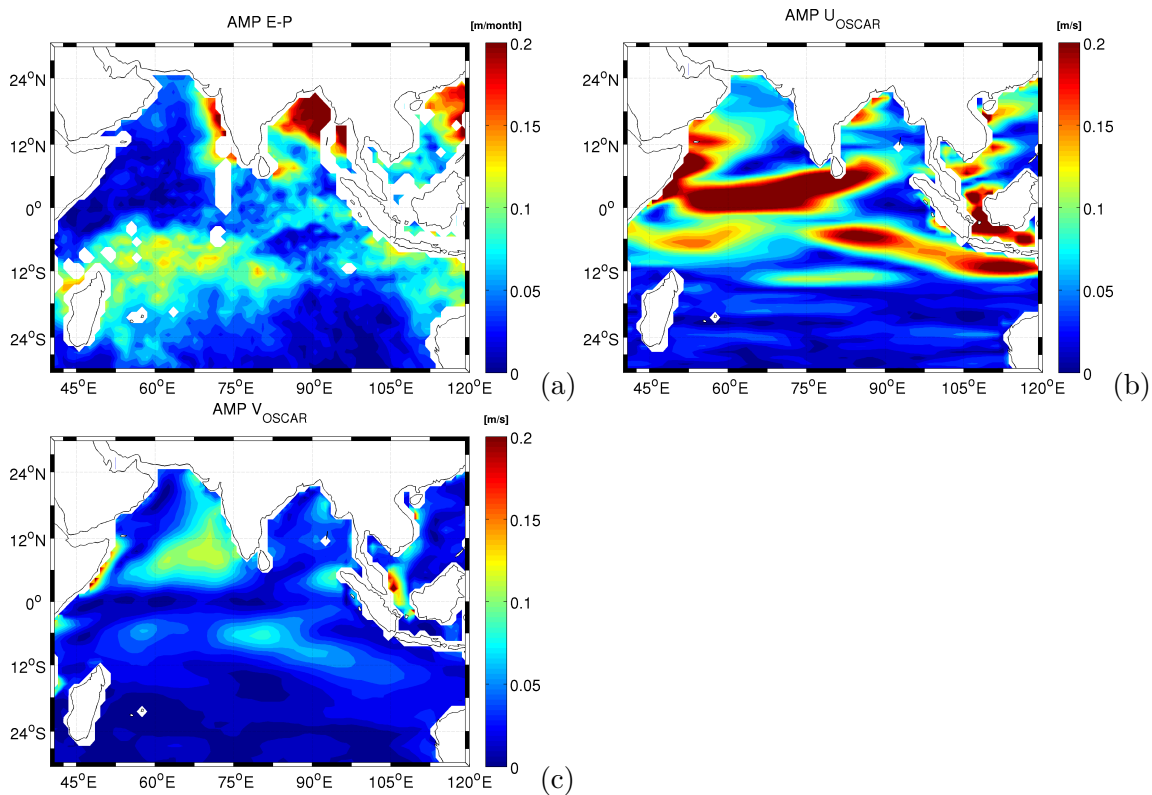


Figure 4.2: Amplitude of the annual cycle for (a) $E-P$ (in $\frac{m}{month}$) and (b) zonal OSCAR velocity and (c) meridional velocity (in $\frac{m}{s}$)

During the southwestern (summer) monsoon phase, high-salinity waters flow from the Arabian Sea into the Bay of Bengal. The annual amplitude of zonal and meridional velocity (see Fig. 4.2b,c) is also increased in the southern Arabian Sea and south of the

Indian subcontinent. During summer monsoon, strong southeasterlies blow along the coasts of the Arabian peninsula and Somalia and create strong coastal upwelling and downwelling in the interior of the Arabian Sea. The annual amplitude of zonal and meridional velocities is increased off Somalia and the Arabian peninsula. This upwelling is indicated by the higher amplitudes in Argo but not represented by SMOS. Seasonally varying upwelling also occurs off the coast of Sumatra and Java, which is represented by Argo and SMOS. Higher amplitudes can also be found in the Java Sea, the location of exchange between the Indian Ocean and the Pacific Ocean. These annual amplitudes are closely linked to the monsoon cycle and the input of small rivers (*Boyer and Levitus, 2002*).

The observed annual phases correspond with the month of maximum SSS during the annual cycle and are presented in Fig.4.1b,d. Both fields are in good agreement with each other, indicating the salinity maximum in the central equatorial Indian Ocean in September-November due to the eastward advection of high-salinity waters under the influence of the semiannual Yoshida-Wyrtki Jets (e.g. *Nyadjro and Subrahmanyam (2014)*, *Sakova (2010)*, *Schott et al. (2009)*). These jets characterize the transition from summer to winter monsoon and vice versa and are accompanied by a shoaling of the thermocline in the west and a deepening of the thermocline in the eastern Indian Ocean.

In the equatorial region, the SSS is lowest in March/April due to advection of low-salinity water from the eastern Indian Ocean/Indonesian Throughflow. In the Bay of Bengal, the SSS is highest in June and lowest in September/October. As shown by *Akhil et al. (2014)*, a tongue of low-salinity waters forms in the northeastern Bay of Bengal during August to October and spreads along the eastern and western boundaries of the Bay of Bengal. During late winter, this freshwater tongue weakens and retreats back to the northeastern Bay of Bengal. The freshwater supply varies strongly on seasonal timescales, and the freshening in boreal fall follows the seasonal maximum of precipitation and river discharge (*Akhil et al., 2014*). Here, low-salinity surface waters lay above more saline water, resulting in a sharp near-surface haline stratification (differences up to 4) between SSS and salinity at 50 m depth in front of major river outlets (*Akhil et al., 2014*).

Corresponding phase patterns can also be observed south of Sumatra and Java. The salinity maximum is reached in September/October due to the seasonal upwelling of high-salinity waters.

Differences between the phase of the annual cycle obtained from SMOS and Argo can be found in a region influenced by the Indonesian Throughflow, where SMOS indicates a salinity maximum in December and Argo in January. Also different are the phases west

of Sumatra. Here, SMOS has its salinity maximum in January, whereas Argo has its maximum in February/March.

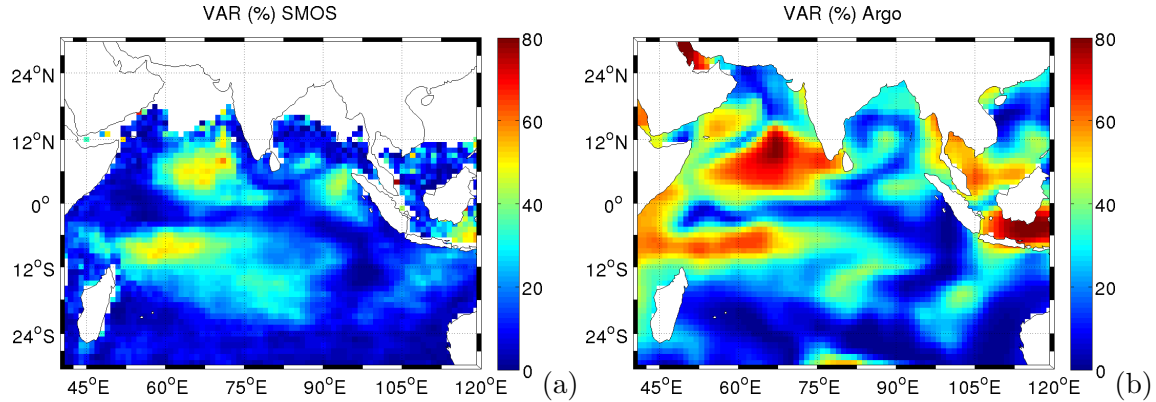


Figure 4.3: Percentage of total variance contained in the annual and semiannual cycle for (a) SMOS and (b) Argo

The second harmonic of the annual cycle in SSS (not shown) is less distinct but has larger amplitudes in the Bay of Bengal, where the wind forcing is the main driver for the semiannual variability (*Benshila et al., 2014*). A detailed discussion of the annual cycle can be found in *Benshila et al. (2014)* and in the above mentioned studies.

Figure 4.3 shows the contribution of the annual cycle to the variability for SMOS and Argo. More than 70% of variability in Argo SSS is explained by the first two harmonics in the southeastern Arabian Sea and the Java Sea, which is not represented by SMOS. Also, the higher variability in the tropical Indian Ocean is explained by the annual cycle to approximately 60%. SMOS shows corresponding spatial patterns in the interior but does not resolve the annual amplitudes in coastal areas.

4.1.2 Interannual variability

On interannual timescales, the Indian Ocean Dipole (IOD) is an important phenomenon of tropical ocean-atmosphere interaction (*Ashok et al., 2003*). The IOD – first identified by *Saji et al. (1999)* – manifests through a zonal SST gradient, where the western Indian Ocean becomes warmer (colder) than the eastern Indian Ocean during positive (negative) IOD events. As described by *Sakova (2010)*, under normal conditions, monsoon winds blow from west to east in June, which produces upwelling off Somalia in the western In-

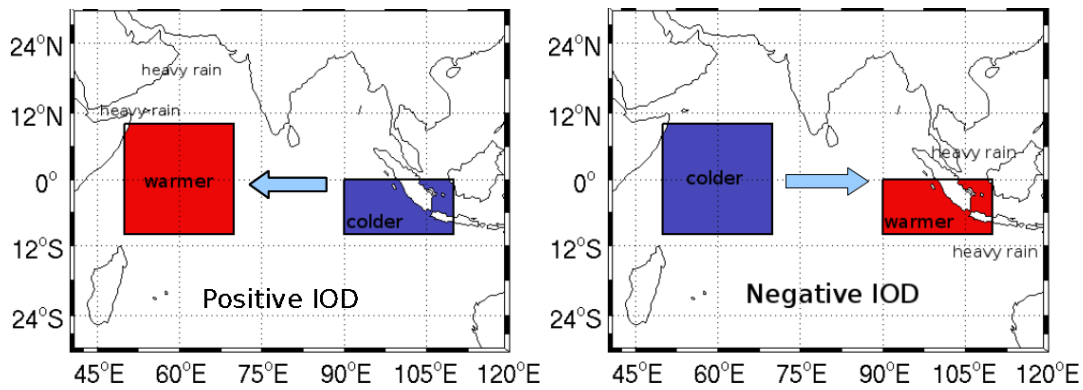


Figure 4.4: Indian Ocean Dipole (IOD) positive (left) and negative (right) phase. Arrows mark the wind direction.

dian Ocean during summer monsoon. This upwelling weakens in fall due to the reduced monsoon winds, which results in an increase in SST in the western Indian Ocean. In boreal fall, stronger westerlies near the equator transport the warm water eastward. During positive IOD (P-IOD), a cooling off Sumatra-Java and a warming off Somalia combined with anomalous easterlies along the equator and stronger precipitation in the western Indian Ocean occur in boreal fall (see Fig. 4.4). The easterly alongshore winds near Sumatra favor upwelling in the eastern Indian Ocean, which contributes to the cooling of SST in the eastern Indian Ocean due to Ekman pumping lifting colder water to the surface, a process known as Bjerknes feedback (*Sakova (2010), Schott et al. (2009)*). During negative IOD (N-IOD) events, opposite conditions prevail in the Indian Ocean with warmer waters and higher rain rates in the eastern Indian Ocean and negative SST anomaly differences in the western Indian Ocean. N-IOD events represent an intensification of normal conditions in the Indian Ocean, while P-IOD events are characterized by a reversal of these. A detailed description of the IOD characteristics can also be found in *Sakova (2010)*. Small changes in SST have profound effects on the atmosphere. A warmer ocean creates increased convection, rise of warm and moist air, consequently resulting in rainfall. Therefore, SST changes alter atmospheric circulation and rainfall distribution and have a strong influence on the weather of neighboring regions such as East Africa, India and Indonesia as well as East Asia, Mediterranean regions and Australia (*Ashok et al., 2003*). *Ashok et al. (2004)* showed that IOD events influence the strength of the monsoon by inducing anomalous convergence (divergence) patterns over the Bay of Bengal during P-IOD (N-IOD) events, leading to enhanced (reduced) rainfall. *Qiu et al. (2014)* showed that rainfall anomalies occur over southern China influenced by the IOD, with a stronger influence from P-IOD. Over the Bay of Bengal and South China Sea, a low-level anomalous anticyclone amplifies

the southwesterlies during boreal fall resulting in increased moisture flux and higher rain rate over southern China.

As described by *Sakova (2010)*, the decay of a P-IOD is characterized by a slow eastward propagation of the warm SST anomaly, resulting in a deeper thermocline and reduced upwelling. This causes an increase of SST in the eastern Indian Ocean. The western Indian Ocean becomes colder, which causes a stronger monsoon. The enhanced Ekman transports strengthened coastal upwelling, which contributes to rapid cooling. Accordingly, the subsurface processes play an important role in the development and the decay of IOD events in the Indian Ocean (*Feng and Meyers (2003)*, *Rao et al. (2002)* and *Vinayachandran and Yamagata (1999)*). Rossby and Kelvin waves change the depth of the thermocline in the upwelling region off Sumatra and Java. A deeper thermocline increases the temperature of entrained water, whereas a shallower thermocline decreases it. The zonal SST anomaly gradient between the western equatorial Indian Ocean and the eastern equatorial Indian Ocean acts as a dipole and is described by the Dipole Mode Index (DMI, *Saji et al. (1999)*). The DMI is positive during P-IOD events and negative during N-IOD events. An IOD behavior is identified when the absolute detrended DMI value exceeds 1 standard deviation for more than 8 weeks (Commonwealth of Australia 2015, Bureau of Meteorology <http://www.bom.gov.au/climate/ahead/model-summary.shtml#tabs=Indian-Ocean>). The IOD can coincide with El Niño-Southern Oscillation (ENSO) events caused by an extension of the Walker Circulation to the west and can be triggered via the Indonesian Throughflow (*Zhang et al. (2013)*, *Ashok et al. (2003)*). If both modes are in phase, the impacts of El Niño and La Niña are often more extreme over Australia, whereas the impacts of these events can be diminished in the case of an out-of-phase-event (*Ummenhofer et al., 2009*). IOD events develop during boreal spring/summer (pre-IOD), peak around October and decay by the end of the year.

The anomaly does not only manifest in SST but also in other atmospheric and oceanic variables. SSH, wind stress, pressure, precipitation and outgoing longwave radiation are anomalous during IOD events. Various studies (e.g. *Nyadjro and Subrahmanyam (2014)*, *Durand et al. (2013)*, *Zhang et al. (2013)*, *Grunseich et al. (2011a)*) report that SSS shows anomalies during positive and negative IOD phases, too. As shown by *Grunseich et al. (2011a)*, SSS variations in the tropical Indian Ocean appear to have reinforcing effects on the IOD, creating a positive feedback, which leads to larger SSS anomalies. The temporal development of the DMI for the period from 1980 to 2014, presented in Fig. 4.5a, shows that extreme P-IOD events occurred during 1994 and 1997, and less strong P-IOD events occurred in 2006, 2007 and 2012. Strong N-IOD events occurred in 1996, and in 2010 cou-

pled with a moderate La Niña (<http://www.jamstec.go.jp/frgc/research/d1/IOD/e/seasonal/outlook.html>).

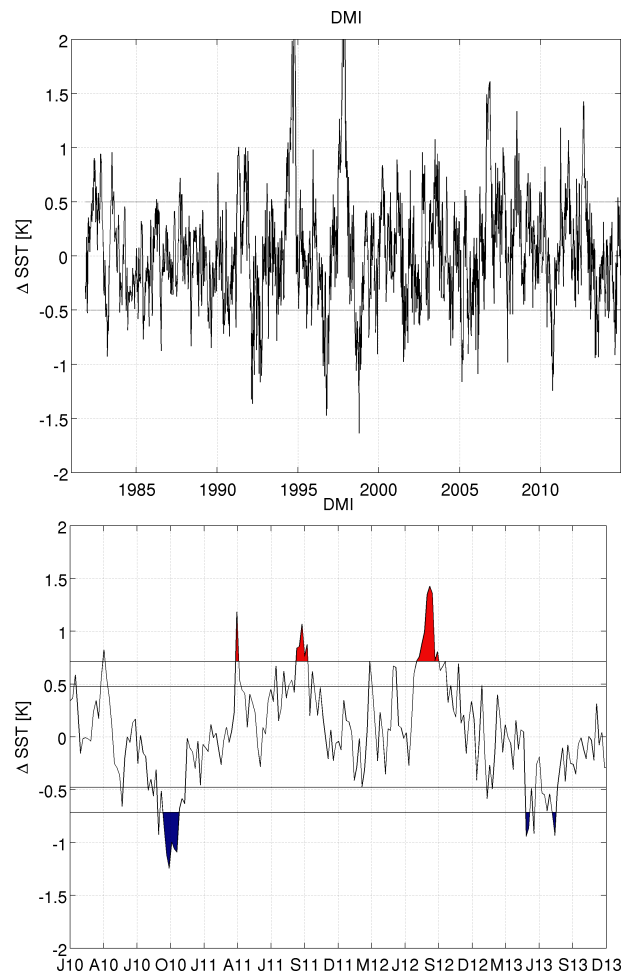


Figure 4.5: Dipole mode Index. Zonal weekly SST anomaly gradient between the western equatorial Indian Ocean (5°E - 70°E and 10°S - 10°N) and the eastern equatorial Indian Ocean (90°E - 110°E and 10°S - 0°N) for the period (a) 1980-2014 and (b) 2010-2013. The index is calculated by the NOAA, using the Reynolds OIv2 SST analysis, made available through the IRI Data Library, and is updated weekly (last update 07-OCT-2015).

Shown in Fig. 4.5b is the DMI for the period from 2010 to 2013 with a distinct SST dipole during the N-IOD in 2010 and P-IOD in 2012. The lines represent the standard deviation ($\text{STD}=0.51$) and 1.5 standard deviation ($1.5\cdot\text{STD}=0.7$). In 2010 and 2012, the DMI exceeds the 1.5 standard deviation threshold for more than 8 weeks. The P-IOD in 2012 develops in July, peaks in August and decays after October. 2011 is also defined

as a P-IOD year, but here, the dipole is not as distinctive as in 2012. Figure 4.6 shows the standard deviation of SMOS and Argo fields of the 4-year-period (2010-2013) with the annual and semiannual cycle removed. Both fields show high variability in the Bay of Bengal and coastal areas around the Indian subcontinent reaching amplitudes of up to 0.5. High variability can also be found south of the equator where SSS variations are related to P-IOD and N-IOD events. Averaged over the study area (30°S - 24°N ; 40°E - 120°E), the SMOS variability is 0.2, whereas the Argo variability is 0.1. Overall, the SMOS field is noisier, while Argo shows pronounced amplitudes in the Bay of Bengal and also in the central equatorial Indian Ocean between 70°E and 90°E .

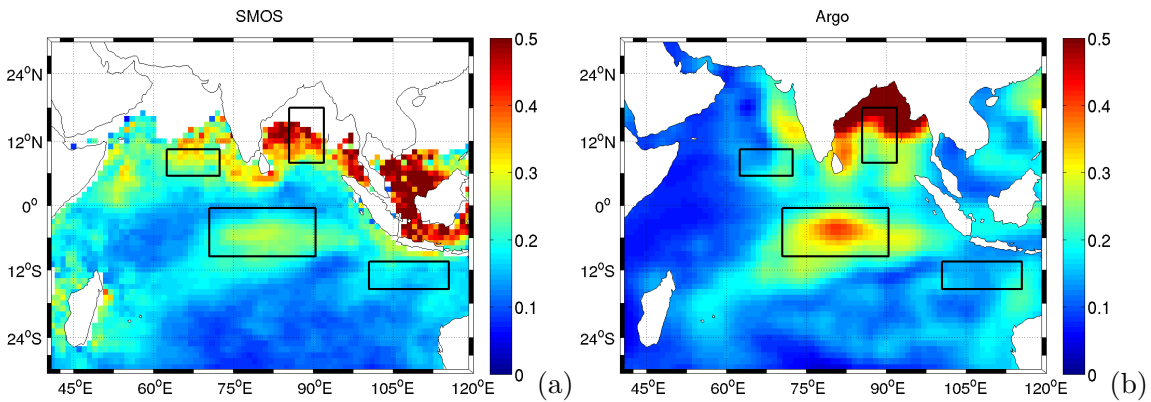


Figure 4.6: Standard deviation fields of (a) SMOS and (b) Argo salinities (with the seasonal cycle and semiannual cycle removed). The boxes mark the NWIO region (5°N - 10°N ; 62°E - 72°E), the BOB (8°N - 18°N ; 85°E - 92°E), SEIO (1°S - 10°S ; 70°E - 90°E) and ITF (10°S - 15°S ; 100°E - 115°E).

In the following, regions with pronounced variability are chosen to analyze salinity anomalies and the driving mechanisms: the Northwestern Indian Ocean (NWIO), the Bay of Bengal (BOB), the South Equatorial Indian Ocean (SEIO) and the Indonesian Through-flow (ITF) region. The regions are indicated in Fig. 4.6, and the abbreviations for the regions (NWIO, BOB, SEIO and ITF) are used when describing these boxes. Figure 4.7 shows the temporal evolution of box-averaged monthly anomalies (relative to the annual average) for SMOS, Argo, STORM and Aquarius SSS for the period from January 2010 to December 2013. *Nyadjro and Subrahmanyam (2014)* showed that SMOS is able to capture the anomalous SSS signal during the N-IOD event in 2010, comparing two different regions in the tropical Indian Ocean. The authors chose a region close to the coasts of Java and Sumatra. Since a distance-to-coast-dependent bias is found in the satellite SSS

data (compare Fig. 3.18), study areas not that close to the coast were chosen here. Positive SSS anomalies can be found in the SEIO box (see Fig. 4.7a) during the peak of the N-IOD in boreal fall 2010. SMOS captures the high salinity waters in this region and matches closely with Argo and STORM. Negative SSS anomalies can be observed in the spring of 2012 and after the peak of the P-IOD in 2012, which develops in July and decays after October.

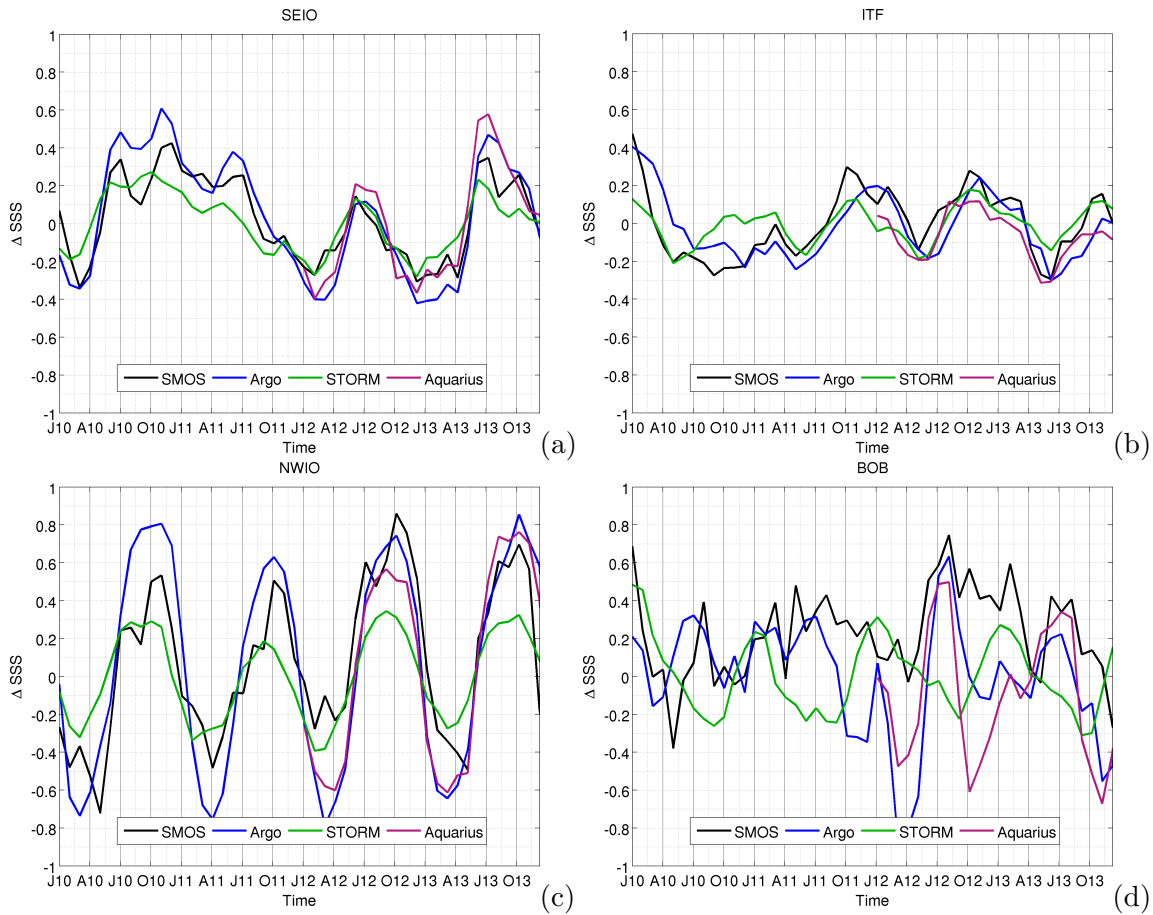


Figure 4.7: Temporal development of box averaged monthly anomalies for SMOS, Argo, STORM and Aquarius salinities for (a) SEIO, (b) ITF, (c) NWIO and (d) BOB region for the period from January 2010 to December 2013. Anomalies are calculated as monthly mean salinity minus 4-year salinity average.

In the ITF box (Fig. 4.7b), negative SSS anomalies are present during the N-IOD peak in 2010. During the same period in the following years, the anomalies are positive. Here, the temporal development of box-averaged anomalies for the different datasets differs from

each other. SMOS and Argo capture the low-salinity signal during the N-IOD, whereas STORM anomalies are inconspicuous.

In the NWIO box, the SSS anomalies, conducted from the different datasets, show a distinct annual cycle with minima in boreal spring and maxima in boreal fall. The SSS minima are due to the transport of low-salinity waters from the Bay of Bengal into the Arabian Sea during winter monsoon. Argo shows slightly larger amplitudes than SMOS, except in the fall of 2012, where SMOS anomalies are larger.

In the BOB, the anomalies of the different datasets differ even more strongly from each other. SMOS shows a positive bias, with a minimum anomaly in May 2010 and maximum anomalies between March 2012 and March 2013. In general, SMOS overestimates the SSS in the BOB and underestimates the SSS in the NWIO region. STORM shows a prominent annual cycle with minima in boreal summer and maxima in boreal winter, reflecting the annual cycle of river discharge, which is highest in August (*Durand et al., 2011*). Monthly Argo anomalies show lower variability until 2012. Large negative anomalies up to -0.8 are present in March 2012, and large positive anomalies can be observed during the boreal summer of 2012. Aquarius also shows these large negative anomalies. This negative SSS signal is highly correlated with a large precipitation signal in this region at this time (not shown).

Figure 4.8 shows the box-averaged SSS anomalies (relative to the 4-year-mean) of SMOS and Argo after removing the annual and semiannual cycle. The x-axis shows the month, and the y-axis shows the years, so that the differences between the years are clear to identify. Significant positive anomalies (approximately 0.3) of SMOS and Argo SSS appear in the SEIO region during the peak of the N-IOD, which prevails until the boreal summer of 2011 (Fig. 4.8a). Negative SSS anomalies can be observed in the second half of 2011 during the weak P-IOD. In 2012, a moderate P-IOD occurred in the central Indian Ocean, characterized by negative SSS anomalies. In 2013, positive anomalies can be observed. These are less intense than in 2010, thus confirming the weaker N-IOD phase. Further southeast in the ITF region, negative SSS anomalies are present during boreal fall 2010 (Fig. 4.8b). During the P-IOD events in 2011 and 2012, positive SSS anomalies are observable in the ITF region. Positive SMOS SSS anomalies are more pronounced during October/November 2011 than the Argo SSS anomalies.

Large differences between Argo and SMOS anomalies occur west of the Indian subcontinent in the NWIO region (Fig. 4.8c, compare also Fig. 4.7). SMOS shows negative anomalies in the pre-IOD phase (summer), whereas Argo shows slightly positive anomalies. Large differences between SMOS and Argo can also be found in the BOB region (Fig. 4.8d).

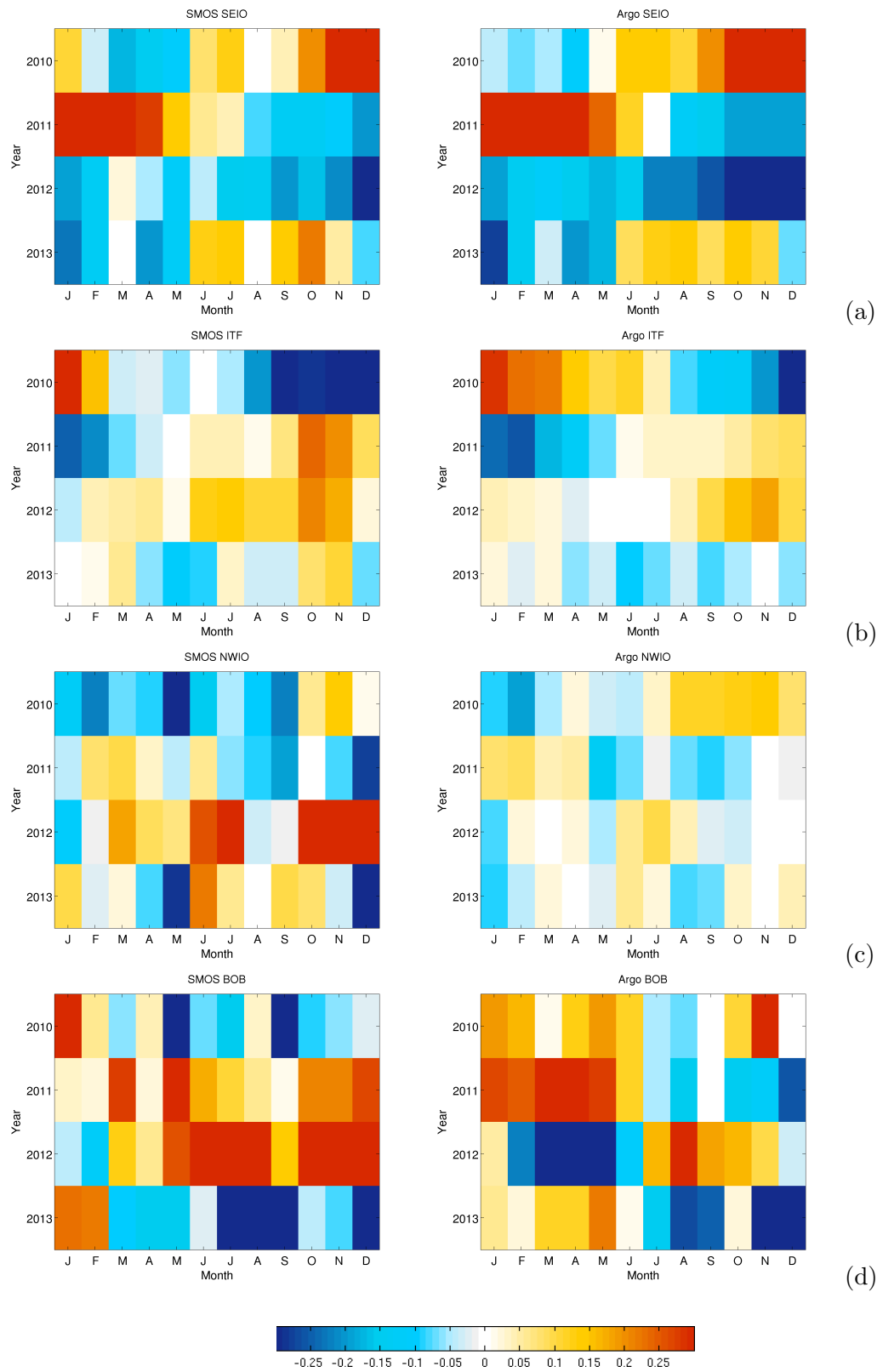


Figure 4.8: Month-year plot of monthly SMOS (left) and Argo (right) anomalies relative to the 4-year-mean with the annual and semiannual cycle removed for (a) SEIO, (b) ITF, (c) NWIO and (d) BOB region. Color scale ranges from -0.3 (blue) to 0.3 (red).

SMOS results in negative anomalies from May to July 2010, whereas Argo shows positive values. In the boreal spring of 2012 large negative anomalies are present in Argo, but cannot be found in SMOS. The same is true for the period from October to December in 2011 and 2012.

In summary, in near-shore regions, the datasets differ significantly from each other due to the various limitations discussed in Chapter 3. In equatorial regions, all used datasets show the expected SSS anomalies during the N-IOD event in 2010 and the P-IOD events in 2011 and 2012. The mechanisms governing these anomalies will be analyzed in detail in the following budget analyses by combining satellite-retrieved SSS with the Argo measurements. Due to the large uncertainties in coastal regions, only the regions in the central Indian Ocean (SEIO and ITF) are considered in further analyses.

4.2 Salinity budget analyses

The temporal development of salinity is governed by several processes such as evaporation, precipitation, river runoff, melting and formation of sea ice, horizontal transport and mixing. The relative importance of all these processes and their changing with time and region is not well known. By combining satellite-retrieved measurements with *in situ* measurements the relative importance of surface fluxes, advection and subsurface processes can be examined. According to *Nyadjro and Subrahmanyam (2014)*, *Li et al. (2013)* and *Qu et al. (2011)*, the salinity conservation equation can be expressed as follows:

$$\underbrace{\frac{\partial S}{\partial t}}_{\text{ST}} = \underbrace{\frac{S(E-P)}{h}}_{\text{SEF}} - \underbrace{(\mathbf{U} \cdot \nabla S)}_{\text{ADV}} - \underbrace{\frac{\partial h}{\partial t} \frac{\Delta S}{h} H - w_{EK} \frac{\partial S}{\partial z}}_{\text{SUB}} + \text{R} \quad (4.1)$$

ST is the salinity tendency and denotes the change of the salinity S with time t . The Surface External Forces (SEF) term on the right hand side of the equation describes the surface external forcing from the atmosphere, representing the combined effect of surface freshwater flux (E-P) and the mixed layer depth h . The second term on the right hand side represents horizontal oceanic advection (ADV). The velocity field \mathbf{U} can be separated into horizontal Ekman components (u_{es}, v_{es}), driven by wind stress τ , and the geostrophic components (u_{gs}, v_{gs}), which are governed by the horizontal pressure gradient. The geostrophic components of horizontal salinity advection can be expressed as:

$$u_{gs} = -u_g \frac{\partial S}{\partial x} \quad , \quad v_{gs} = -v_g \frac{\partial S}{\partial y} \quad (4.2)$$

where u_g and v_g are surface geostrophic velocities in zonal and meridional direction.

The Ekman wind drift component of horizontal salinity advection was calculated from:

$$u_{es} = -u_e \frac{\partial S}{\partial x} \quad , \quad v_{es} = -v_e \frac{\partial S}{\partial y}. \quad (4.3)$$

The Ekman velocity (u_e, v_e) is related to the surface wind stress τ in zonal and meridional direction:

$$u_e = \frac{\tau^y}{\rho_0 f h} \quad , \quad v_e = -\frac{\tau^x}{\rho_0 f h}, \quad (4.4)$$

where f is the Coriolis parameter and ρ_0 the surface water density.

The third term SUB in Eqn. 4.1 represents subsurface processes including entrainment and vertical pumping. The Heaviside function H accounts for the fact that the salinity is only affected by entrainment when subsurface water is entrained into the mixed layer. Therefore, the entrainment term is multiplied with the Heaviside function H :

$$H = \begin{cases} 0, & \frac{\partial h}{\partial t} \leq 0 \\ 1, & \frac{\partial h}{\partial t} > 0 \end{cases}. \quad (4.5)$$

Since detrainment does not affect salinity and temperature in the mixed layer, H equals zero in the case of a decreasing MLD.

ΔS is the difference between the salinity and the salinity immediately below the mixed layer, which is calculated from individual Argo profiles as described in Section 2.3.

The Ekman pumping velocity w_{EK} is defined as:

$$w_{EK} = \frac{1}{f \rho_0} \nabla \times \tau. \quad (4.6)$$

$\frac{\partial S}{\partial z}$ in the SUB term represents the vertical salinity gradient within the mixed layer which is also calculated from individual Argo profiles. Residual R includes processes not considered, as lateral and vertical mixing processes and estimation errors in the process terms SEF, ADV and SUB.

4.2.1 Salinity flux anomalies

N-IOD events are accompanied by the amplified eastward Yoshida-Wyrtki Jets. These transport warmer, more saline waters in the upper layer, increasing SSH and MLD in the

East (Schott et al., 2009).

The horizontal SSS flux F in $\frac{\text{kg}}{\text{m}^2\text{s}}$ for each grid cell can be expressed as (Nyadjro and Subrahmanyam, 2014):

$$F_x = \rho \cdot u \cdot SSS \cdot 10^{-3} \frac{\text{kg}}{\text{g}} \quad , \quad F_y = \rho \cdot v \cdot SSS \cdot 10^{-3} \frac{\text{kg}}{\text{g}} \quad (4.7)$$

where $U = (u, v)$ is the zonal OSCAR surface velocity, and ρ is the surface water density, which is a function of SSS and SST.

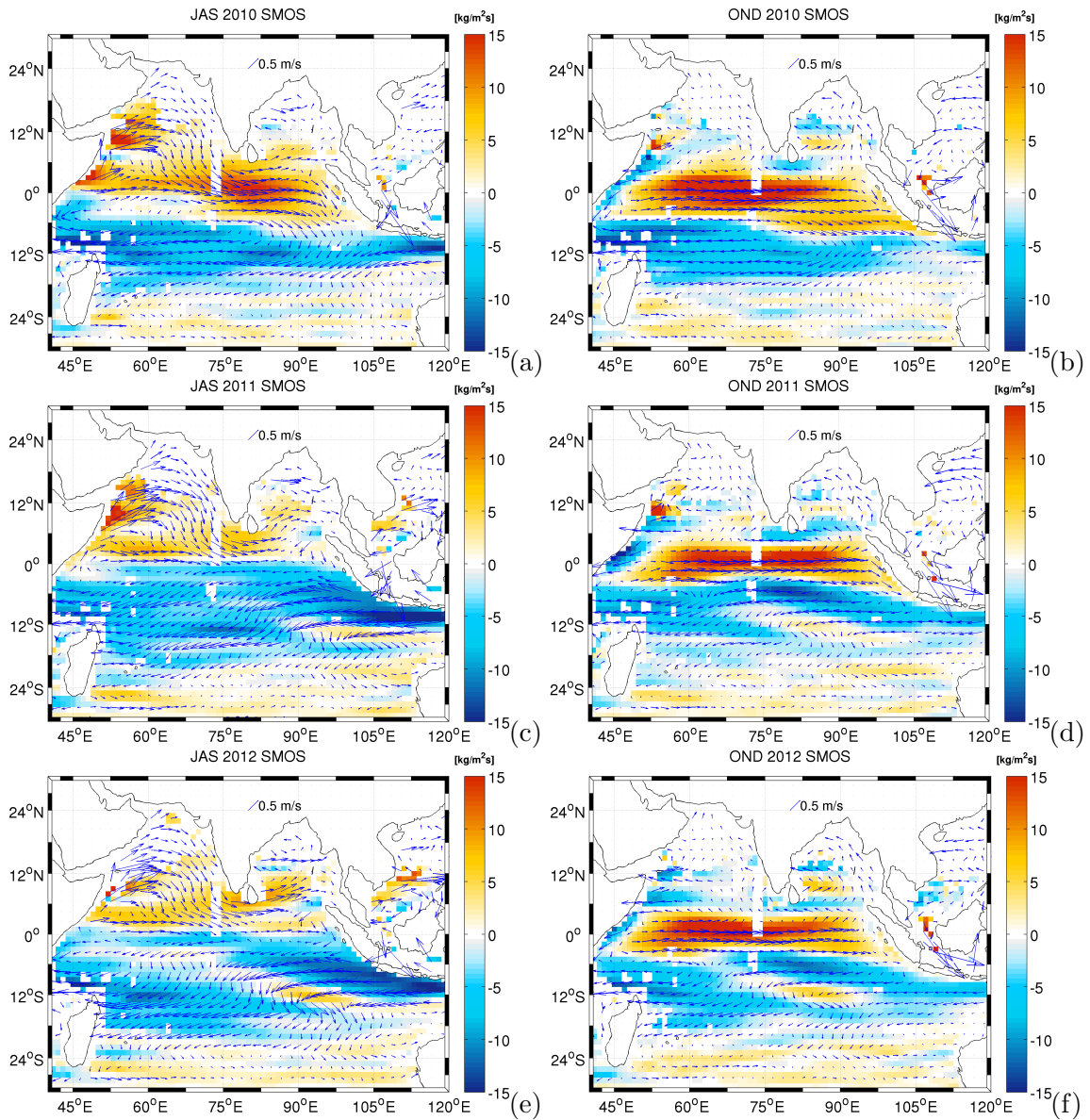


Figure 4.9: Average zonal (positive eastward) SMOS SSS flux in $\frac{\text{kg}}{\text{m}^2\text{s}}$ for (left) July-September and (right) October-December 2010, 2011 and 2012

The meridional SSS flux is significantly lower than the zonal one. Therefore, Fig. 4.9 shows the zonal SMOS SSS flux and OSCAR surface currents for the period from July to September and October to December in 2010, 2011 and 2012, respectively. Here, it will be build upon the studies of *Nyadjro and Subrahmanyam (2014)*, who analyzed the N-IOD in 2010. During the summer monsoon, high-salinity surface waters from the Arabian Sea and northeastern African regions flow towards equatorial regions (see Fig. 4.9a,c,e). The semiannual Yoshida-Wyrtki Jets transport the high-salinity waters along the equatorial region (see Fig. 4.9b,d,f). In the last quarter of 2010, the high-salinity waters extend into regions southwest of the equator due to the strengthening of the Yoshida-Wyrtki Jets during the N-IOD. In 2011 and 2012, negative salinity flux anomalies are present in equatorial regions due to the reversal from westerlies to easterlies during the P-IOD events (see Fig. 4.9c,e). The westward SSS flux in equatorial regions between October and December 2011 is stronger than between October and December 2012.

In a band around 10°S, the zonal SSS flux is dominated by the westward SEC, which is weakened during N-IOD. The SEC brings warm, low-salinity waters from the Pacific into the Indian Ocean through the Indonesian Throughflow (*Schott et al., 2009*).

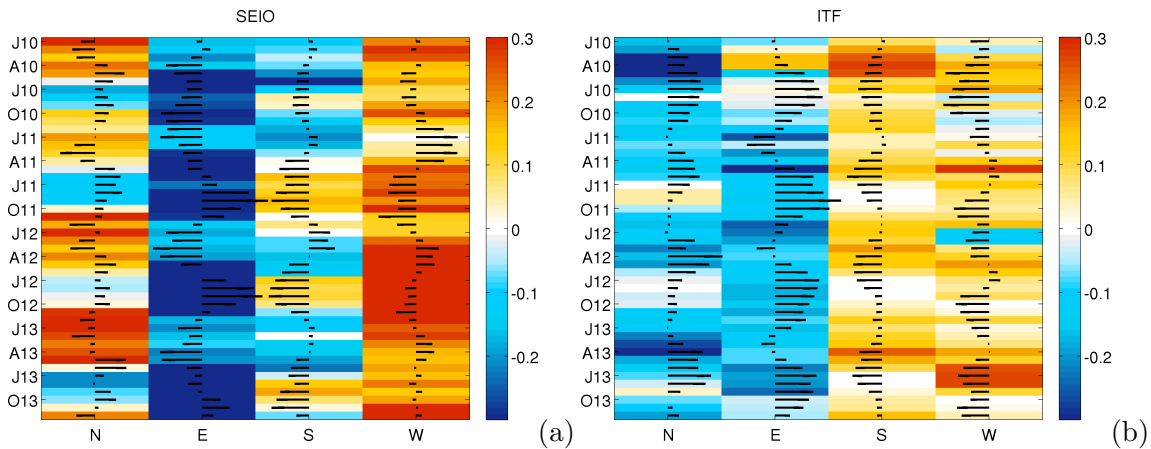


Figure 4.10: Temporal development of the volume transport through the lateral boundaries (North, East, South, West) and salinity difference between the averaged salinity outside the box at the considered lateral boundary and the average salinity in the considered box for (a) SEIO and (b) ITF region. Arrows to the left indicate an outflow. Arrows to the right an inflow.

Figure 4.10 shows the temporal development of the volume transport across the boundaries of the SEIO and ITF boxes where SSS anomalies during the IOD events are large and

visible in all datasets used (see Fig. 4.7). The volume transport holds:

$$V_x = \int_{y_1}^{y_2} u \cdot z \, dy \quad , \quad V_y = \int_{x_1}^{x_2} v \cdot z \, dx \quad (4.8)$$

V_x and V_y are integrated along the four lateral boundaries of the two boxes. The horizontal current components are representative until the depth $z = 30$ m (*Johnson et al., 2006*), and x_i, y_i are the geographical box boundaries. The sign of V_x and V_y describes the direction of the transport in or out of the box. Arrows to the right indicate an inflow into the box while arrows to the left indicate an outflow. The figure also shows the difference between the average salinity alongside the lateral boundary and the average salinity in the considered box, which indicates whether the flux increases or decreases the SSS in the box. A positive SSS difference concurrent with a volume transport out of the box means that low-salinity waters flow out the box. A positive SSS difference concurrent with a volume transport into the box means, that high-salinity waters flow into the box.

At the lateral boundaries of the SEIO region (see Fig. 4.10a), the annual cycle due to the seasonal, monsoon-induced reversal of currents can be observed. The volume transport into the box is increased in boreal spring and summer through the northern (N) and western boundary (W). The outward volume transport through the eastern (E) and southern (S) boundary is increased in boreal spring and in boreal summer, respectively.

Anomalies in these patterns can be observed during the N-IOD 2010 and also during the P-IOD events in 2011 and 2012. The volume transport of high-salinity waters through the western boundary is increased in the peak-phase of the N-IOD in 2010. At the same time, the outflow at the eastern boundary increases. This corresponds with the previous results, confirming that the strengthening of the Yoshida-Wyrtki Jets transports high-salinity waters into regions south of the equator.

During the P-IOD events in 2011 and 2012 (August/September) the volume transport into the box at the eastern boundary is maximal due to the northward shift of the trade winds bringing less saline waters into the box.

Further southeast, in the ITF region, the volume transport shows a clear annual cycle. The volume transport into the box through the northern and eastern boundary is maximal in boreal spring and summer, respectively. The volume transport out of the box is increased during the summer months and happens mainly through the southern and western boundary. Anomalies in the volume transport are less distinct than in the SEIO region, but in the spring of 2010, high-salinity waters are transported into the region through the eastern boundary, while low-salinity waters are transported into the box through the

northern boundary.

In the boreal summer of 2011, high-salinity waters are transported through the northern boundary into the ITF region (see Fig. 4.9b, northern (N) boundary, July-October, positive salinity difference). This indicates advection of high-salinity upwelling waters off Sumatra and Java through the northern boundary, which is consistent with observations during P-IOD events. Slightly positive salinity differences can also be observed in the summer of 2012, but less distinct than in 2011.

In summary, the transports through the lateral boundaries show a clear annual cycle linked to the monsoon cycle. During the N-IOD in 2010, the southeastward transport of high-salinity waters is increased due to the strengthening of the Yoshida-Wyrtki Jets. During the P-IOD events in 2011 and 2012, the currents change direction and low-salinity waters are transported in equatorial regions. Horizontal transports are an important driver for the observed SSS anomalies in the central Indian Ocean. Negative SSS anomalies were observed in the ITF region during the N-IOD event in 2010 and positive SSS anomalies were observed during the P-IODs in 2011 and 2012. The volume transport in the ITF region does not vary significantly between the years. This implies, that also other processes are of importance for the salinity tendencies during IOD events. In the following, the salinity budget is calculated in order to quantify the mechanisms, driving the temporal development of salinity and the observed anomalies in the Indian Ocean. Furthermore, the components of horizontal salinity advection will be analyzed in detail to show which processes have the main influence on the horizontal transports.

4.2.2 Salinity budget in the tropical Indian Ocean during the Indian Ocean Dipole

The salinity budget terms of the Indian Ocean are examined for each grid point using monthly SMOS SSS and Argo MLS fields and the simplified salinity budget of Eq. 4.1. As shown in Section 3.3.3, the SMOS and Argo data agree well in regions far away from the coast. Mean differences between these two datasets in the SEIO and ITF region are less than 0.1 and, therefore, I assume, that SMOS SSS tendency is a good proxy for the MLS tendency. The spatial distribution of the SMOS budget terms, including surface external forces SEF, horizontal advection ADV and subsurface processes SUB over the tropical and subtropical Indian Ocean are shown in Fig. 4.11, averaged over the peak-IOD period from August to October, 2010 and 2011.

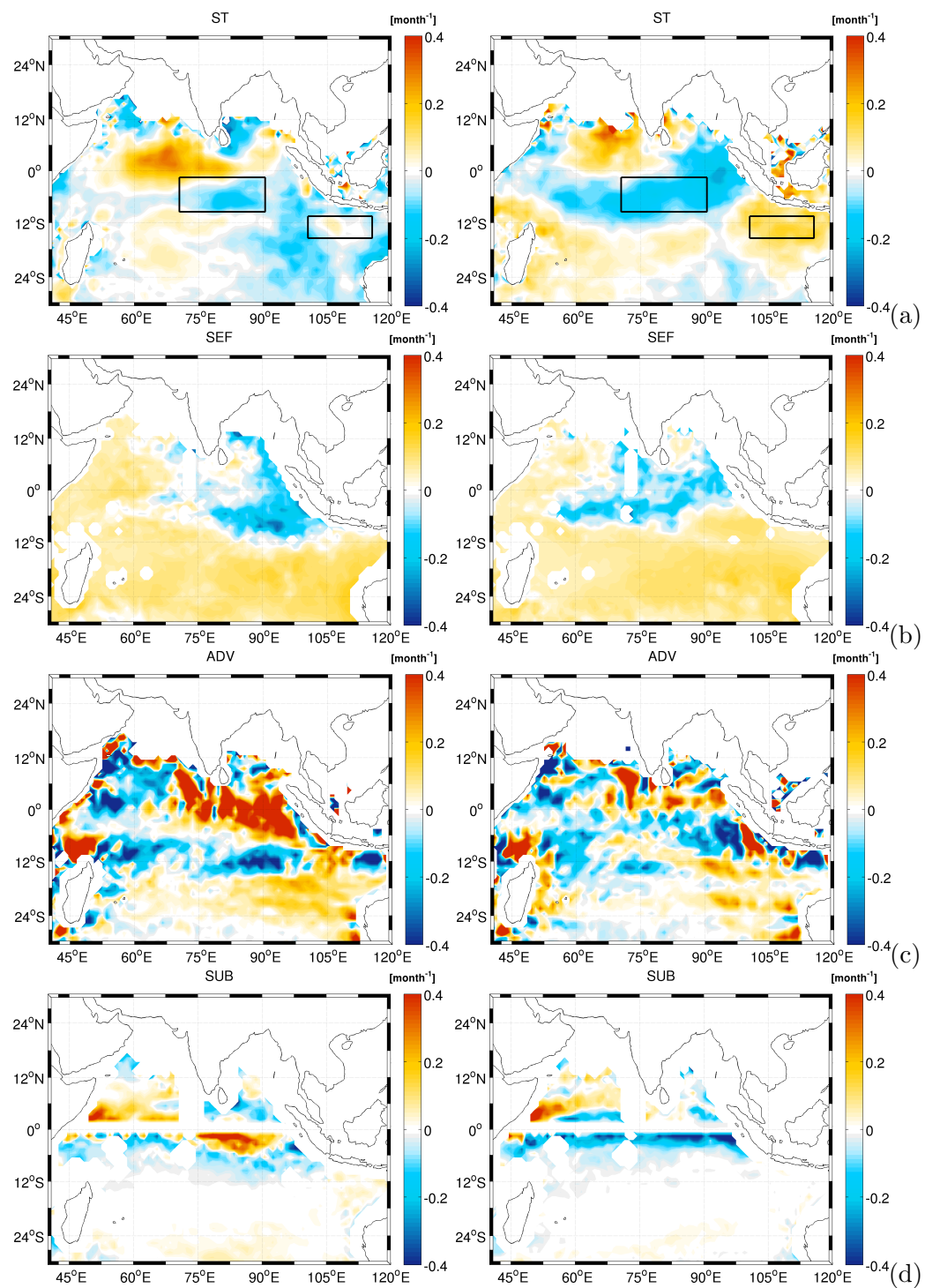


Figure 4.11: Horizontal distribution of: (a) salinity tendency (*ST*), (b) surface external forces (*SEF*), (c) horizontal advection (*ADV*) and (d) subsurface influences (*SUB*) for the period from August to October 2010 (left) and 2011 (right). The boxes in (a) represent the SEIO and ITF regions.

The 2010 averages represent conditions during an N-IOD event, whereas the 2011 averages represent the conditions during a weak P-IOD event. Starting in 2010 the ST is positive in the central Indian Ocean and negative south of the equator (see Fig. 4.11a left). SEF are negative in the eastern part of the basin and north of 10°S . The interannual fluctuations of E are negligible, and P exceeds E conspicuously. Therefore, negative SEF indicate increased precipitation, whereas positive SEF represent reduced precipitation. The horizontal distribution of E-P is shown in the appendix B. Horizontal ADV is positive in the eastern equatorial regions, and the SUB term is positive south of the equator (see Fig. 4.11c,d left). The unusually strong equatorial jets during N-IOD events transport high-salinity waters in regions south of the equator and the unusually strong wind regime increases equatorial Ekman convergence and Ekman divergence in the South, which is represented by the large SUB term.

In 2011, the ST is positive south of Sumatra and Java and negative in the equatorial region (see Fig. 4.11a right). This corresponds to the spatial distribution of the SEF term, which is negative in the northeastern and central Indian Ocean and positive south of the maritime continent. Horizontal ADV is less pronounced in 2011. Positive ADV can be observed in the equatorial region due the advection of high-salinity waters by the Yoshida-Wyrtki Jets which are present in the equatorial region independently from IOD events. Negative ADV can be observed in a band south of the equator, which corresponds to the results shown before (compare Fig. 4.9d), namely that low-salinity waters are advected westward due to the reversal from westerlies to easterlies. Positive ADV can be observed west of Sumatra. In this region, the current flow has a northward component, and high-salinity waters are transported off the Sumatra and Java upwelling region. The SUB term is negative south of the equator, indicating convection.

Large differences in the salinity budget terms can be observed between the years, therefore, the temporal development of the box-averaged salinity budget components for the SEIO and ITF region is analyzed in detail. Figure 4.12 presents the low-pass filtered salinity budget anomalies, showing the interannual variability. For filtering the signal, a Fourier transform was applied to express the function of time as a function of frequency by decomposing it into sinusoids at different frequencies. The signals are low-pass filtered by removing Fourier components with frequencies higher than a cut off frequency of 13 months. The signal is converted back from the frequency domain to the time domain with the inverse Fourier transform.

Even though the SMOS data only cover a period of four years, they show a pronounced year-to year variability.

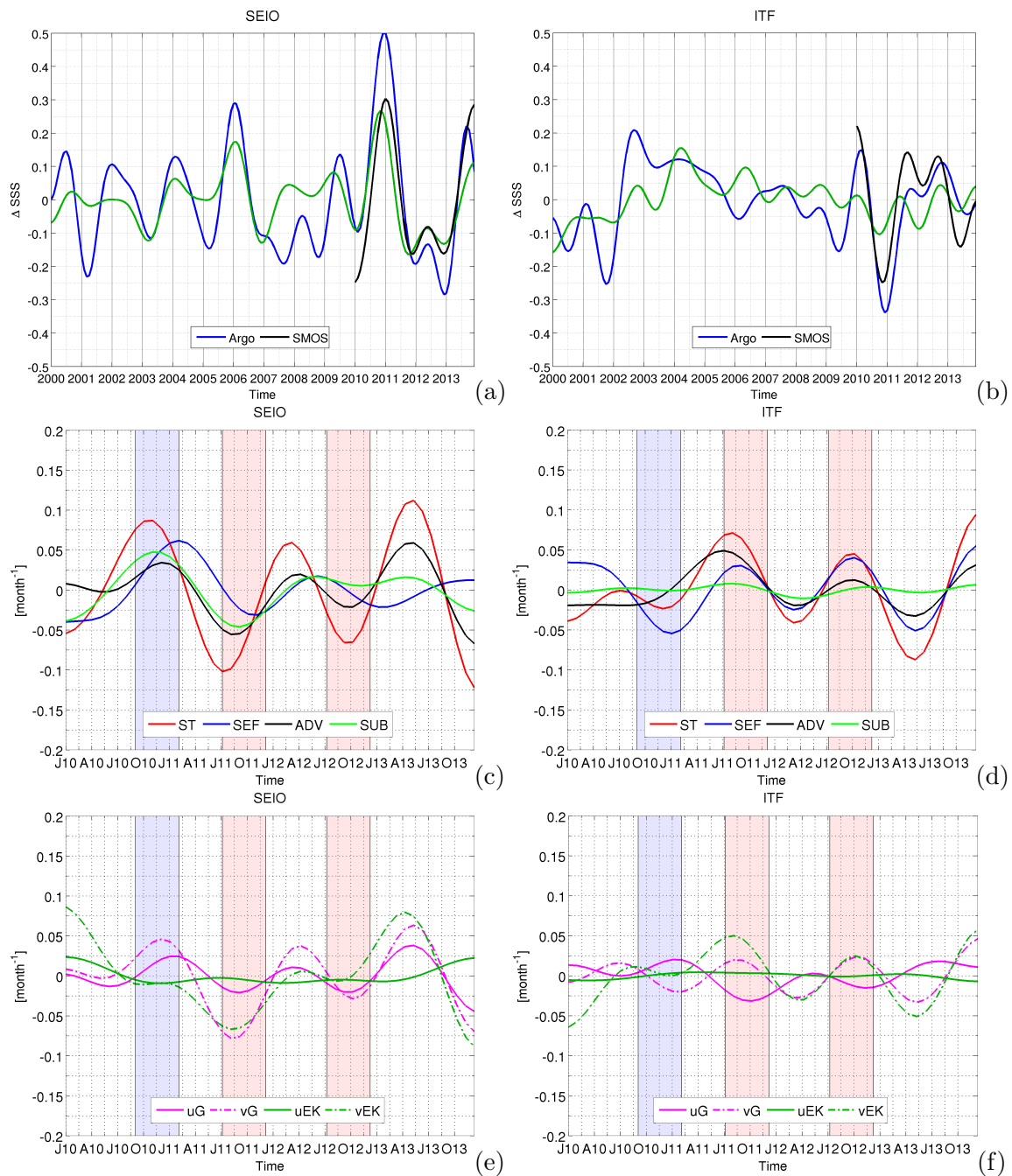


Figure 4.12: Interannual variation of box-averaged (a,b) SSS anomalies and (c-f) salinity budget components for (left) SEIO and (right) ITF region. (c,d): Salinity tendency (ST, red), surface external forces (SEF, blue), advection (ADV, black) and subsurface influences (SUB, green). (e,f) Components of ADV: mean zonal geostrophic flow (uG, magenta) and zonal Ekman ADV (uEK, green) and mean meridional geostrophic flow (vG, magenta dashed) and meridional Ekman ADV (vEK, green dashed).

To confirm, that this is attributable to interannual variability, Fig. 4.12a,b show an intercomparison of low-pass filtered Argo, STORM and SMOS SSS in the SEIO and ITF region. Argo and STORM time series start in 2000, whereas SMOS starts in 2010. Argo and SMOS show similar amplitudes only slightly varying in magnitude. In 2011 and 2012, SMOS shows a larger amplitude than Argo in the ITF region. In the SEIO region, interannual SSS anomalies deduced from STORM data show a behavior which corresponds to Argo but varies significantly in strength. In the ITF region, STORM shows different interannual anomalies than Argo. Due to the good agreement between Argo and SMOS, the SMOS data are considered to provide a reliable basis for the analysis of the SSS dynamics. Thus, Fig. 4.12c,d present the SMOS salinity budget terms as low-pass filtered anomalies for the period from January 2010 to December 2013. An analysis of the unfiltered salinity budget anomalies over the period from 2010 to 2013 can be found in appendix B.

Starting in the SEIO region, ST has a large amplitude of interannual variability with maxima during the IOD events. ST is positive during the N-IOD in 2010 and negative during the P-IOD events in 2011 and 2012. Remarkable is also the positive ST in the spring of 2013. At this time, the DMI is negative which may indicate the development of a N-IOD event. During the N-IOD in 2010, SUB and ADV are increased and show large in-phase variations with ST and a correlation of 0.9 and 0.7 (>95% confidence level), respectively. Although SEF has a large amplitude, the variations are not in phase. This confirms the results shown in Fig. 4.11, namely that south of the equator the ST is mainly driven by horizontal ADV and Ekman pumping during the N-IOD.

During the P-IOD in 2011, low-salinity waters are advected towards equatorial regions due to the reversed equatorial wind regime. This was shown in Fig. 4.9c,d and Fig. 4.11c and can also be observed in Fig. 4.12c where the horizontal ADV is increased during the peak-P-IOD in 2011 with opposite direction compared to 2010. During the P-IOD in 2012, ADV is reduced but increases in the spring of 2013, driving the large amplitude of ST.

As ADV showed to be of major influence for the ST, ADV is decomposed in its zonal and meridional components. Figure 4.12e,f show the low-pass filtered anomalies of the horizontal ADV terms. Both meridional and zonal components are important, but the meridional component shows a higher correlation with the total ADV (compare also Table B.1 in appendix B). As supposed, the meridional geostrophic ADV component (v_G) increases during the peak-N-IOD in 2010 due to the stronger-than-normal Yoshida-Wyrtki Jets. At the same time, the northward Ekman transport is reduced (v_{EK}).

During the peak-P-IOD in 2011 (July-October 2011), low-salinity water is advected into the SEIO region. The geostrophic flow (u_G , v_G) and meridional Ekman ADV (v_{EK}) show

a larger amplitude. This is due to the anomalous easterlies which transport low-salinity waters into the SEIO region and increase the southward Ekman transport during the summer monsoon. Increased meridional Ekman and geostrophic ADV can also be observed during the P-IOD in 2012, but less distinct than in 2011. The P-IOD events terminate abruptly as the wind changes to westerlies *Sakova (2010)*. The northward Ekman transport increases during the winter monsoon season.

In the ITF region, ST is negative during the peak-N-IOD in 2010 which is driven by negative SEF. ST shows also a strong positive peak during the summer/fall of 2011, driven by positive SEF and increased ADV. As shown in Fig. 4.12f, the meridional Ekman component has a large amplitude at this time. During the P-IOD event in 2012, ST is also positive but the amplitude is less distinct than in 2011. The SEF variability in 2012 is of the same amplitude as during the P-IOD in 2011, whereas the horizontal ADV and SUB is less strong.

As described before, P-IOD events are accompanied by a reversal of the equatorial wind regime. The anomalous easterlies favor the upwelling of cold and high-salinity waters off Sumatra and Java. The transport of high-salinity waters into the ITF region is clearly shown during the weak P-IOD event in 2011 (compare Fig. 4.10b, Fig. 4.12d). The southward Ekman transport of high-salinity waters is increased at this time (Fig. 4.12f, positive v_{EK} amplitude). During the P-IOD in 2012, southward Ekman ADV is less distinct due to weaker upwelling off Sumatra and Java.

During the IOD events, the salinity budget is nearly closed (compare Fig. B.2e,f in appendix B), which means that the ST can mainly be explained by the discussed processes. The residual R is $<0.03 \text{ month}^{-1}$. This R may result from enhanced mixing processes, diffusion and estimation errors in the process terms.

In summary, the positive and negative anomalies associated with the IOD events from 2010 to 2013 can be observed. The positive SSS anomalies in the SEIO region during the N-IOD event in 2010 can be explained by the advection of high-salinity waters towards equatorial regions and enhanced Ekman pumping bringing high-salinity waters to the surface. During the P-IOD events, low-salinity waters are advected into the SEIO region. At this time the meridional geostrophic ADV component and the southward Ekman ADV of low-salinity waters are increased, driving together with the negative SEF term, the observed negative SSS anomalies.

In the ITF region, maximum meridional Ekman transport anomalies can be observed in the summer of 2011, indicating the advection of high-salinity upwelling waters off Sumatra and Java into the box. In 2012, the P-IOD characteristics are less distinct than in 2011,

despite the strong SST dipole during the peak phase. The anomalous IOD characteristics were also mentioned by *Lan (2012)* with regard to the SST dipole. The SST dipole in 2012 develops in July and decays after October, which is shorter than historical events (see Fig. 4.5 and *Lan (2012)* and Table 1 in *Grunseich et al. (2011a)*). In 2013, N-IOD characteristics are present and comparable with the strong N-IOD in 2010 even though the SST dipole is not distinctive (weak N-IOD with DMI exceeding 1.5 standard deviation only for a few weeks).

In 2012 and 2013, the Madden-Julian Oscillation (MJO; Madden-Julian Oscillation official monitoring page, Commonwealth of Australia 2015, Bureau of Meteorology: <http://www.bom.gov.au/climate/mjo/>), which tends to be most powerful during boreal spring and summer, has been active over the Indian Ocean. The MJO has wide ranging impacts on precipitation, SST and atmospheric circulation in tropical regions and varies also on interannual timescales (*Marshall and Hendon, 2013*). The modulated IOD characteristics may be attributable to the interaction with the intraseasonally varying MJO. Therefore, in the following, the development of the moderate P-IOD and weak N-IOD events in 2012 and 2013, respectively, will be analyzed in relation to the MJO.

4.3 Influence of the Madden-Julian Oscillation on SSS dynamics

The MJO, first discovered by *Madden and Julian (1972)*, is a dominant mode of variability on intraseasonal timescale. It influences many global meteorological phenomena. As described by *Zhang (2005)*, an MJO event features a large-scale eastward moving center of strong convection with enhanced rainfall (active phase), bordered to the east and west by regions of weak convection and reduced rainfall. The latter is referred to as the inactive phase. One half of the globe lies within the active phase and the other half in the inactive phase with opposite characteristics concerning to clouds and rainfall. The dominant period of the MJO spreads over a range of 30 to 100 days with an average period of 30 to 60 days (*Zhang, 2005*). This convective anomalies propagate eastward, influencing also SSS, which responds to freshwater fluxes and advection. *Drushka et al. (2014)* described how the MJO influences thermohaline dynamics of the upper ocean convective cells, which produce turbulent and sensible heat flux anomalies as well as precipitation anomalies. Zonal wind anomalies produce turbulent mixing in the upper ocean and horizontal advection of temperature and salinity and their gradients (*Drushka*

et al., 2014). Positive SSS anomalies occur during inactive MJO phases of enhanced winds, reduced cloud cover and positive outgoing longwave radiation (OLR) anomalies.

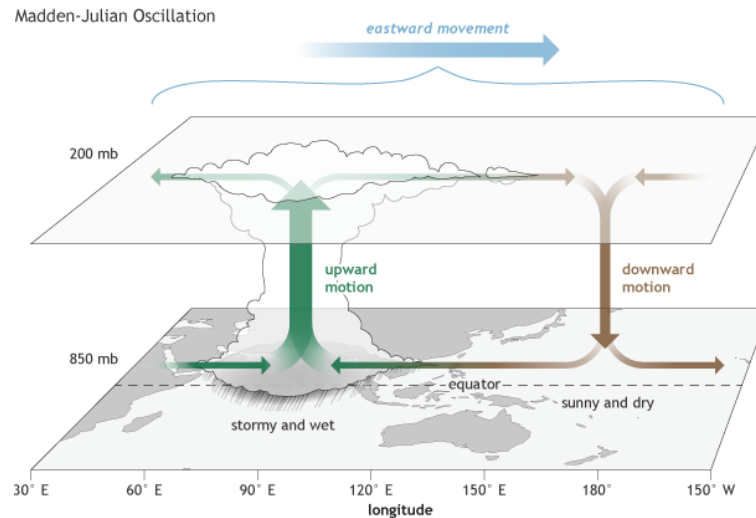


Figure 4.13: Atmospheric structure of the Madden-Julian Oscillation for the active phase (enhanced rainfall, green) centered over the Indian Ocean and the suppressed convective phase (brown) centered over the Pacific Ocean. Horizontal arrows pointing left represent easterlies, whereas arrows pointing to the right represent westerlies. The entire dipole moves eastward over time, circling the globe and eventually returning to its point of origin. Taken from *climate.gov* (<https://www.climate.gov/news-features/blogs/enso/what-mjo-and-why-do-we-care>, freely re-usable), drawing by Fiona Martin

Negative OLR anomalies are an indicator of enhanced cloudiness and convection. More convective activity implies higher, colder cloud tops, that emit much less infrared radiation into space. Negative OLR anomalies occur with increased precipitation and together with a wind reduction, resulting in negative SSS anomalies. Enhanced surface westerly winds occur near the western and eastern edge of active convection. Wind-induced advection can also produce SSS anomalies (*Grunseich et al., 2011b*). *Grunseich et al. (2013)* analyzed the influence of the MJO on SSS in the Indian Ocean by comparing MJO-related variables with Aquarius SSS anomalies. SSS anomalies are formed during 10 active MJO phases between September 2011 and February 2013. With a temporal resolution of one month one is able to resolve variations with periods of two months (Nyquist frequency), which corresponds to the MJO-period but is at the limit of resolution.

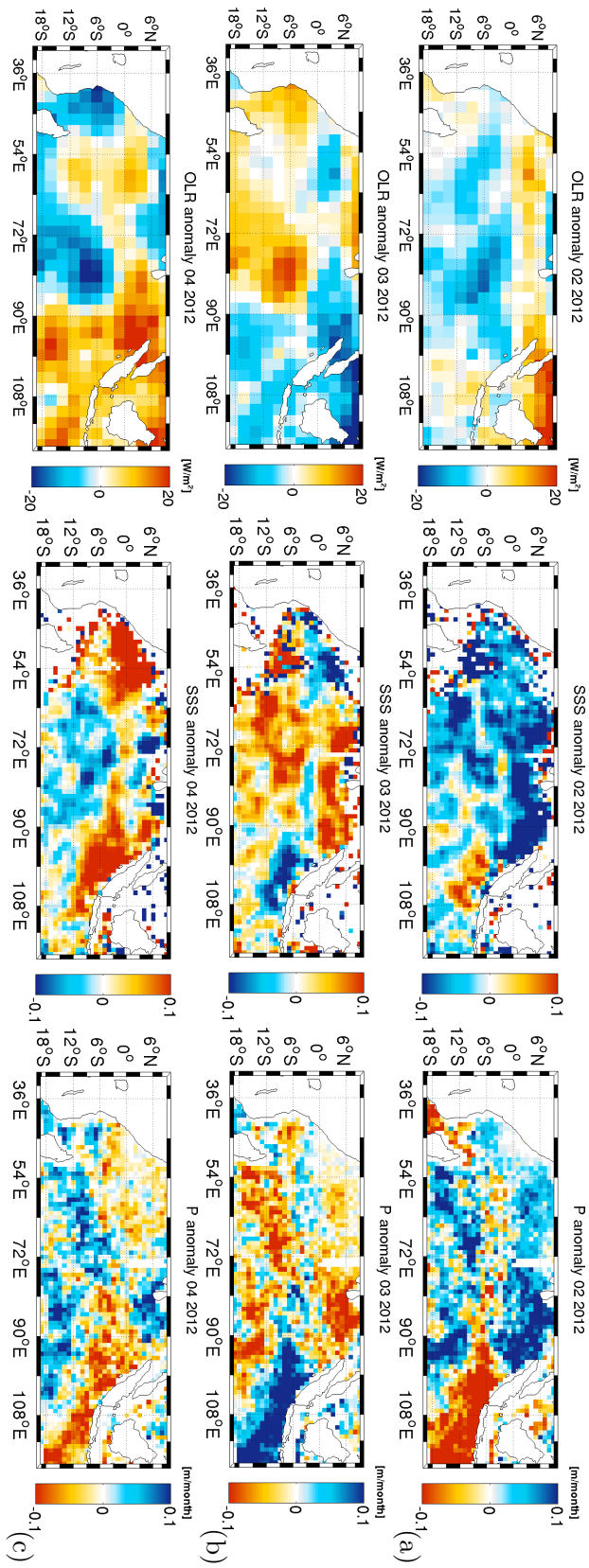


Figure 4.14: Intraseasonal anomalies of (left) outgoing longwave radiation (OLR), (middle) SMOS SSS and (right) precipitation for (a) February, (b) March, and (c) April 2012. Note, that the color bar of P anomalies is inverted so that blue indicates an increased precipitation and red indicates reduced precipitation.

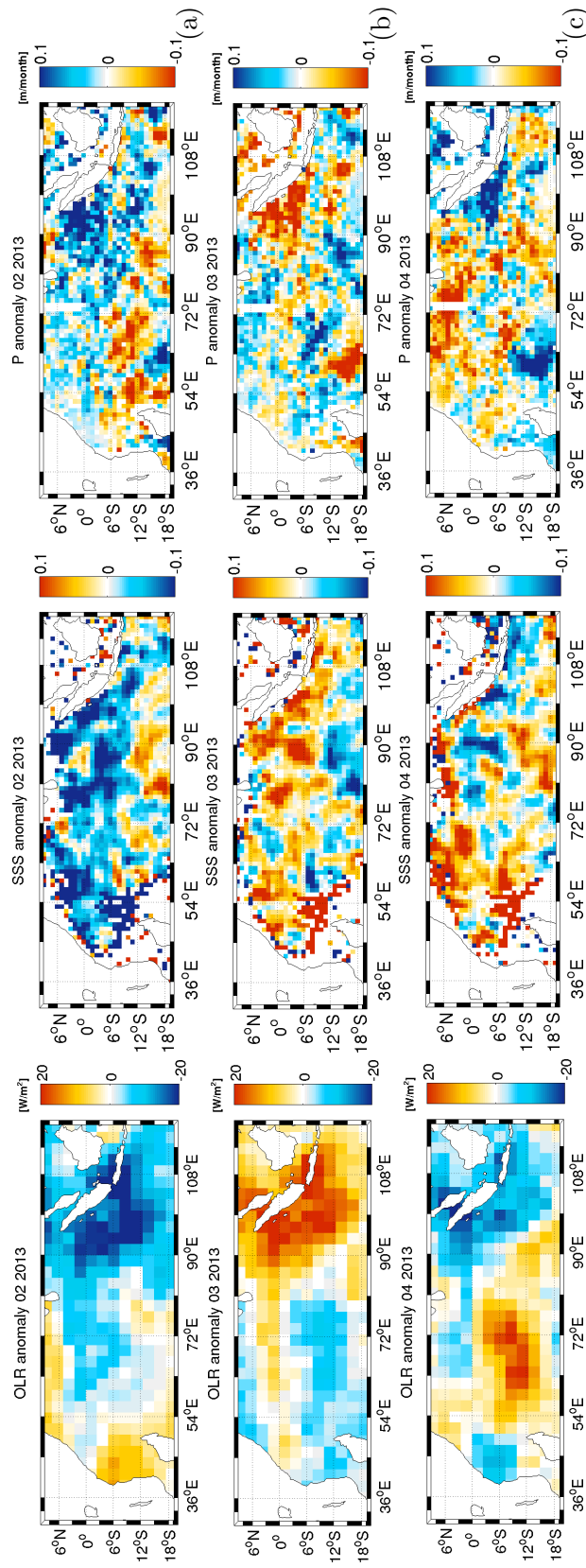


Figure 4.15: Intraseasonal anomalies of (left) Outgoing longwave radiation (OLR), (middle) SMOS SSS and (right) precipitation for (a) February, (b) March, and (c) April 2013. Note, that the color bar of P anomalies is inverted so that blue indicates an increased precipitation and red indicates reduced precipitation.

Table 4.1: Correlation of intraseasonal OLR and P anomalies to SSS anomalies in the SEIO and ITF region for the 4-year period from 2010 to 2013 and for 2012. The correlations for the 4-year period are significant at the 95% confidence level. Significance was calculated using student *t* test.

Region	OLR 2010-2013	P 2010-2013	OLR 2012	P 2012
SEIO	0.63	-0.76	0.61	-0.83
ITF	0.66	-0.47	0.82	-0.73

To get a first impression of intraseasonal variability of the MJO-related variables, high-pass filtered OLR, SSS and P anomalies (cut-off frequency of 3 months) are shown in Fig. 4.14 and Fig. 4.15 for the spring season in 2012 and 2013, respectively. Negative OLR anomalies form over the western Indian Ocean, whereas positive anomalies persist over the maritime continent (see Fig. 4.14a). In March 2012, large negative OLR anomalies over the maritime continent can be observed, whereas positive OLR anomalies are formed in the central Indian Ocean (see Fig. 4.14b). One month later, in April 2012, the positive OLR anomalies are centered in the eastern Indian Ocean and over the maritime continent. SSS and P anomalies correspond spatially to the OLR anomalies and reveal a strong relationship between atmospheric and oceanic conditions.

Negative OLR anomalies and enhanced precipitation are present in the western Indian Ocean in February and April 2012, which contributes to the development of negative SSS anomalies. In March, negative OLR, SSS and P anomalies can be observed southwest of the maritime continent. By comparing Fig. 4.14 and Fig. 4.15 it can be observed that the center of the large anomalies of OLR, SSS and P shifts to the north in 2013. The anomalies are centered west of the maritime continent. *Zhang (2005)* showed that the surface cools in the convective centers of the MJO and warms outside, creating an SST gradient. In March 2013, the inhibited convective over the eastern Indian Ocean may support the development of an SST dipole and the weak N-IOD development in 2013.

The high-pass filtered anomalies are shown in Fig. 4.16 as box-averaged time series for the SEIO and ITF regions. Starting in the SEIO region, intraseasonal OLR anomalies are large during boreal spring, except in 2011. Also P amplitudes increase slightly during this period. Large zonal wind anomalies during the peak of the N-IOD in 2010 are shown. Zonal wind anomalies can also be observed in the timeframe from boreal winter 2011 to spring 2012.

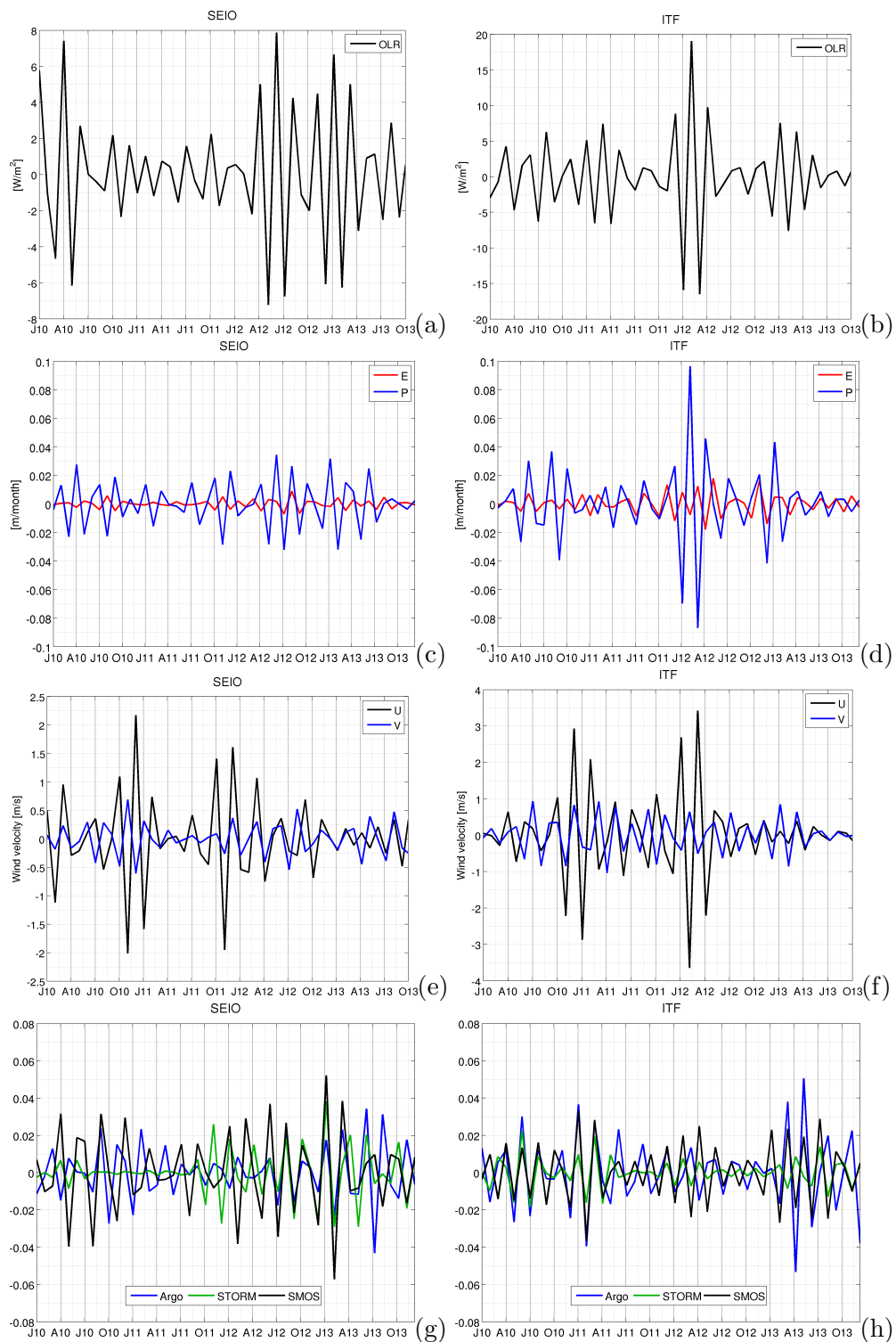


Figure 4.16: Intraseasonal variation of box-averaged (a,b) Outgoing longwave radiation (OLR), (c,d) evaporation (E) and precipitation (P), (e,f) zonal (U) and meridional (V) wind velocity and (g,h) SMOS SSS for (left) SEIO region and (right) ITF region

A connection between the variables is clearly shown in the ITF region in the spring of 2012, where OLR anomalies, P anomalies and zonal wind velocity anomalies are larger than in the years before. Figure 4.17 presents monthly SST and wind velocity anomalies (relative to the monthly average over the 4-year study period) for February, March and April 2012.

In March 2012, large negative SST anomalies and strong westerlies occur in a band southeast of the equator. Anomalous westerlies in this region lead to a deepening of the thermocline (compare also 4.21c, all discussed in detail in Section 4.4) which affects the upwelling regime off Sumatra and Java. A deeper thermocline inhibits the upwelling of colder and high-salinity waters, which influences the development of the negative SST anomaly in the eastern Indian Ocean and may be responsible for the later development of the P-IOD in 2012 (Lan, 2012). Intraseasonal variability of SSS is largest during the N-IOD phases, indicating that both modes interact.

Table 4.1 summarizes the correlation between the different variables.

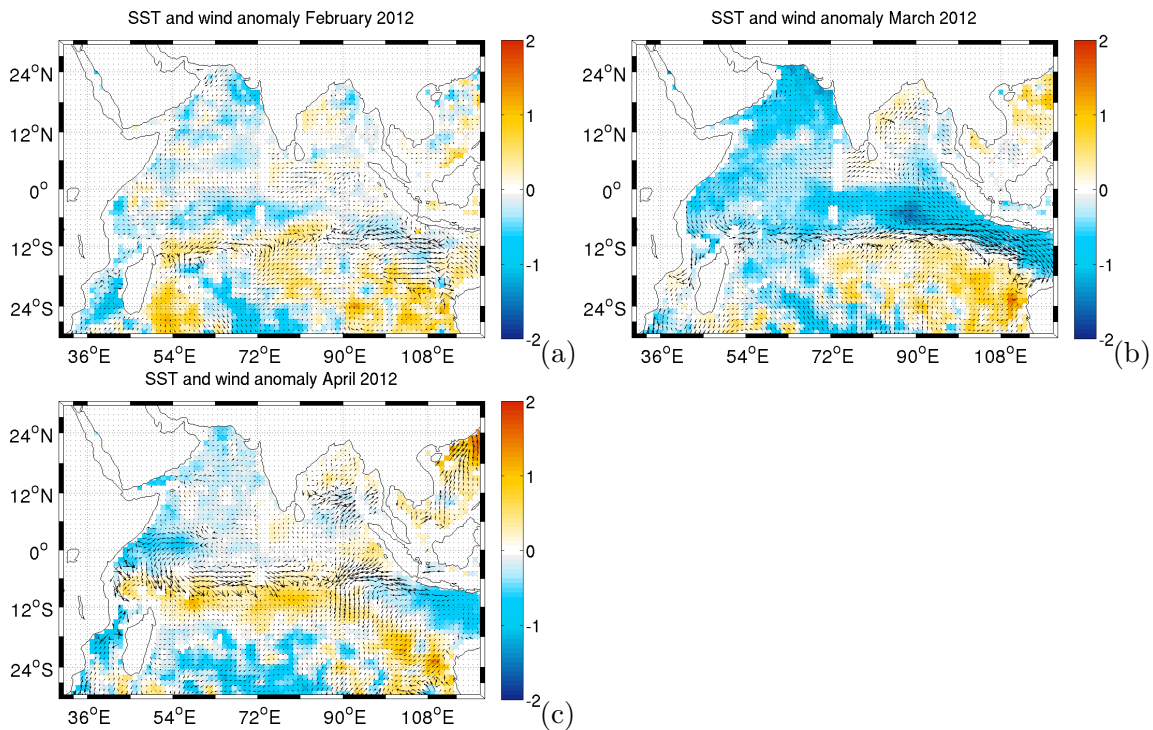


Figure 4.17: Monthly SST (color-coded) and wind anomaly (arrows) relative to the monthly average over the 4-year study period for (a) February, (b) March, (c) April 2012

Correlations between filtered SMOS SSS and P in the SEIO region and ITF region are

-0.76 and -0.47, respectively. Correlations between filtered SSS and OLR anomalies reach values of 0.63 and 0.66 for SEIO and ITF, respectively. For the one-year period of 2012, the variables are even better correlated. *Zhang (2005)* describes the strong year-to-year variability in MJO activity, characterized by strong periods and periods with a weaker or even absent MJO.

It was shown that even with monthly data the intraseasonal variability is covered, possibly modulating the IOD characteristics. The MJO appears also on timescales less than two month. In order to verify the origin of the intraseasonal variability, a wavelet analysis is applied to MJO-related variables using data with a higher temporal resolution. The results are described in the following section.

4.3.1 Analysis of variabilities using wavelet transform

The wavelet transform decomposes a time series into the time-frequency space. As distinct to the Fourier transform, which is only localized in frequency, one is able to determine the dominant frequencies and their variation in time (*Torrence and Compo, 1997*). A Fourier transform decomposes the signal in cosines and sines, and the functions are localized in the Fourier space. In contrast, the wavelet transform is based on a particular family of wavelets, which is a class of orthogonal functions localized both in time and frequency domains (*Sakova, 2010*). A practical guide to wavelet analysis is given by *Torrence and Compo (1997)* and shortly summarized in the appendix. Figure 4.18a,c presents the OLR and SSS wavelet power spectrum. Here, OLR and SMOS SSS data with a daily and 3-day¹ temporal resolution, respectively, are chosen to capture also periods shorter than two months. The constructed time series were averaged over 5°S-0° and 87°E-93°E. This region was chosen, because of its strong MJO-related signals (*Grunseich et al., 2013*) and its relatively large distance to the coast, in order to avoid the strong influence of land contamination and RFI in the SMOS data. The spectra reveal the variability of the OLR and SSS signal at different frequencies within the 4-year time interval of the signal. The wavelet amplitudes are color-coded and give the signal strength. The background spectrum is modeled by choosing an appropriate lag-1 autocorrelation (0.76 for OLR and 0.83 for SMOS SSS). The cone of influence, indicating the region of the wavelet spectrum affected by boundary effects is shown as a black line.

¹The data quality of the 3-day resolution SSS product is low, therefore, it was only chosen for the analysis of fast processes.

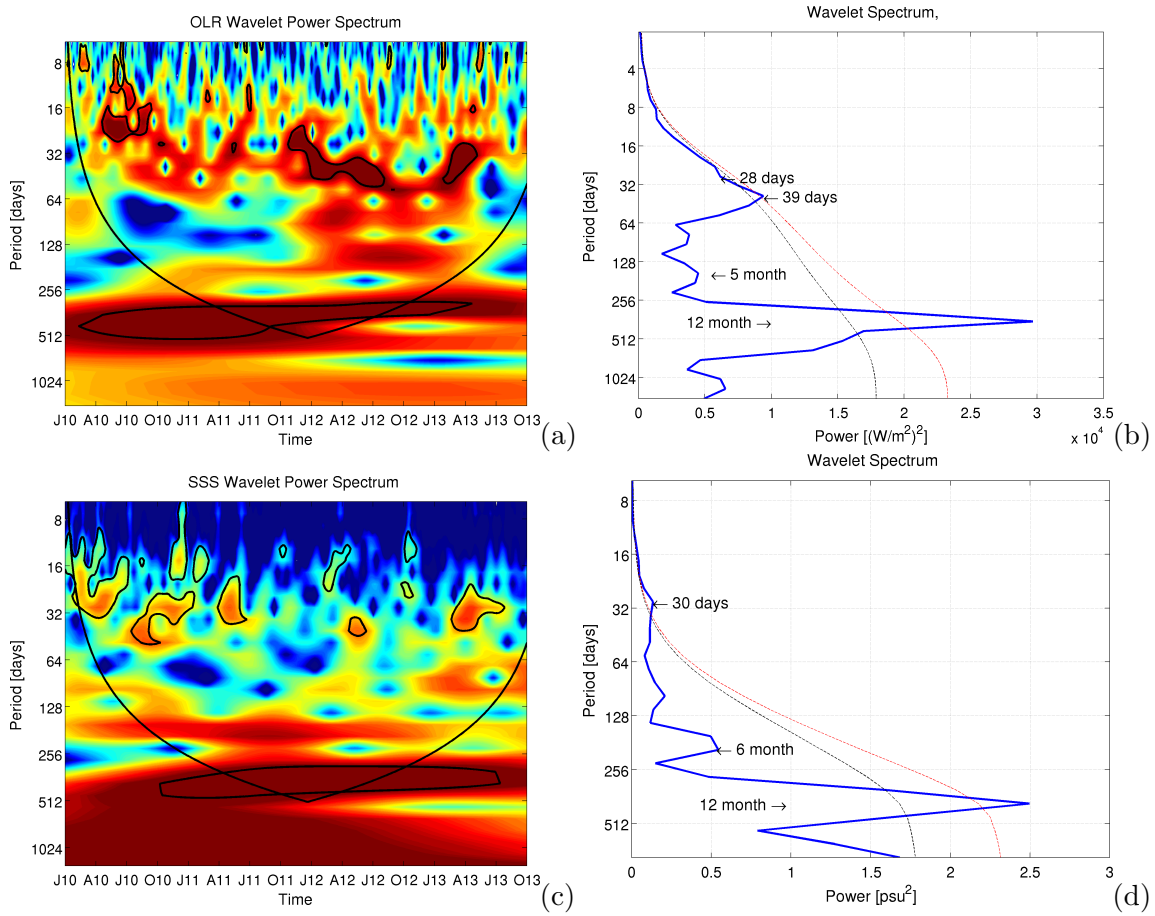


Figure 4.18: Wavelet analysis of OLR (top) and SMOS SSS (bottom) averaged over $5^{\circ}S-0^{\circ}$ and $87^{\circ}E-93^{\circ}E$ for the period from January 2010 to December 2013. (left) Wavelet power spectra (importance of a wave period at a given time), The redder the color, the stronger the signal is. The black line represents the cone of influence. Statistically significant signals at the 95% confidence level are indicated with solid contours. (right) The global wavelet power (the importance of the wave period over the time series). Red and black dashed lines represent the 95% and 90% confidence level for a background red noise process with anything above being significant.

Both OLR and SSS have a strong annual signal. These maxima can clearly be identified in the global wavelet spectra (Fig.4.18b,d). The 95% and 90% confidence levels for a background noise process are shown as a red and black line, respectively. SMOS shows a strong interannual SSS signal that starts to develop at the beginning of the time series and remains strong until the summer of 2012. The interannual signal lies in the cone of influence and has to be treated with caution, since the time series encompasses only

4 years. In the higher frequency range, the OLR signal is strong during the period from April to July 2010 with a centered period of 20 days. Another strong OLR signal is present between October 2011 and July 2012 and appears to have a period centered at 39 days. A strong OLR signal with this period can be observed from January to March 2013. Strong, but not significant OLR signals with periods between 60 and 90 days are present during the second half of 2010 and around April 2012.

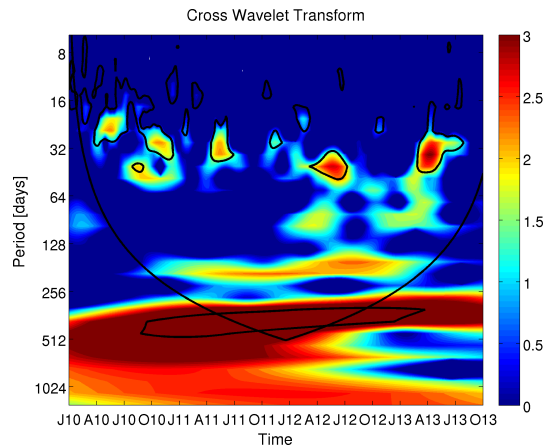


Figure 4.19: Cross wavelet transform of standardized OLR and SMOS SSS averaged over $5^{\circ}S-0^{\circ}$ and $87^{\circ}E-93^{\circ}E$ for the period from January 2010 to December 2013. The black line represents the cone of influence. Statistically significant signals at the 95% confidence level are indicated with solid contours.

SMOS SSS signal has a high power in the first half of 2010 and in April/May 2011 with a period less than 30 days. The SSS signal is strong between July and December 2010, spring 2012 and spring 2013 for periods between 32 and 64 days (see Fig. 4.18c, 2010, April-June 2012, March-June 2013). Stronger SSS signals between 60 and 90 days are present between January 2012 and May 2012 and in the first half of 2013 and show coherent patterns to OLR wavelet amplitudes.

The MJO-related impacts appearing in SSS peak later than in OLR (compare 2012), something also shown by *Grunseich et al. (2011b)*. Here, the MJO was active from October 2011 until July 2012 and SSS peaks in April 2012. Figure 4.19 presents the cross wavelet transform of the standardized OLR and SMOS SSS time series, displaying areas in the frequency-time space where the two time series have high common power (*Grinsted et al., 2004*). The common features found in the individual wavelet transforms are significant at the 95% confidence level with high common power in the second half of 2010, between April and June 2012 and in the spring of 2013, for periods between 32 and 62 days. High,

but not significant common power for periods >60 days are present in the spring of 2012 and in the winter of 2012/spring of 2013.

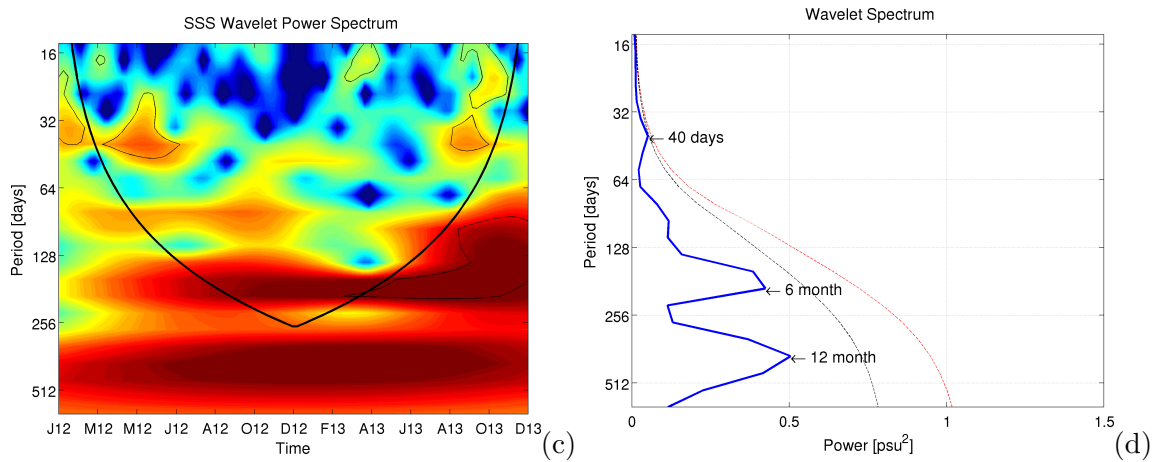


Figure 4.20: Wavelet analysis of Aquarius SSS averaged over $5^{\circ}S-0^{\circ}$ and $87^{\circ}E-93^{\circ}E$ for the period from January 2012 to December 2013. (left) Wavelet power spectrum (importance of a wave period at a given time). The black line represents the cone of influence. Statistically significant signals at the 95% confidence level are indicated with solid contours. (right) The global wavelet power (the importance of the wave period over the time series). Red and black dashed lines represent the 95% and 90% confidence level with anything above being significant.

Figure 4.20 presents the Aquarius SSS wavelet power spectrum for the period from January 2012 to December 2013 conducted from Aquarius L3 data with a temporal resolution of 7 days. Aquarius shows a signal (90% confidence level for a red noise process with lag-1 autocorrelation of 0.73) in the intraseasonal frequency range with a centered frequency of 40 days. This signal is pronounced in the boreal spring of 2010 and in the fall of 2013. Stronger signals for periods >60 days are present in 2012. Aquarius has an annual and interannual signal. Both are statistically not significant as they lie in the cone of influence due to the time series length of only two years.

To conclude, significant common power of OLR and SSS with MJO-related periods occurs during the peak N-IOD 2010 and during the developing phase of the P-IOD in 2012. Westerly wind anomalies, present in March 2012 (compare Fig. 4.16e,f) are associated with the MJO and occur near the eastern and western side of active convection. Anomalous westerlies in the ITF region and off Sumatra and Java deepen the thermocline, thereby inhibiting the upwelling of colder and high-salinity water to the surface. This delays

the development of the positive SST dipole during that time and modulates the P-IOD characteristics in 2012. MJO and IOD-related salinity stratification also have an influence on numerous oceanic processes by forming a barrier layer (*Grunseich et al., 2011a*). This will be explained in the following.

4.4 Barrier layer dynamics

Section 2.3 described the calculation of MLD and ILD. In regions of weak upper ocean haline stratification, temperature stratification determines the base of the MLD. Then, the MLD is equal to the ILD. When salinity dominates the upper ocean stratification, the MLD may be shallower than the ILD, and a layer well mixed in temperature, but not in salinity, can lie between the MLD and the ILD (*Drushka et al., 2014*). This layer is called barrier layer (BL) and its thickness (BLT) is defined as:

$$\text{BLT} = \text{ILD} - \text{MLD} \quad (4.9)$$

The BL acts as a barrier between the well-mixed ocean surface and the thermocline, that restricts turbulent entrainment of cold sub-thermocline water into the ML as well as the impact of surface fluxes on the thermocline (*Drushka et al. (2014)* and *Qiu et al. (2012)*). Various studies (e.g. *Drushka et al. (2014)*, *Felton et al. (2014)* and *Qiu et al. (2012)*) show the development of the IOD due to BL dynamics. Figure 4.21 shows the temporal development of Argo salinity and temperature for various depths as well as MLD, ILD and BLT for the SEIO and ITF region.

The large freshwater influx during the winter monsoon season into the SEIO region due to precipitation and freshwater from the BOB and ITF leads to a haline stratification, resulting in a MLD shallower than the ILD. Driven by the monsoon cycle, the BLT varies seasonally. It is largest in winter due to the increased freshwater flux, and lowest in summer when high-salinity waters arrive, reducing stratification.

Anomalies can be observed between the summer of 2010 and the summer of 2011. The MLS is increased due to the eastward high-salinity water mass transport. The MLD is shallower at the peak of the N-IOD (approximately 25 m) until the spring of 2011 when compared to the following boreal winter season (approximately 40-50 m). During this period, also the temperature in the SEIO region is reduced. The ILD decreases and the BLT favors the upwelling of colder and more saline subsurface waters. This was already shown in Fig. 4.11 and confirms the results of enhanced SUB discussed before.

During 2011 and the P-IOD in 2012, the BLT gets thicker due to the westward ADV

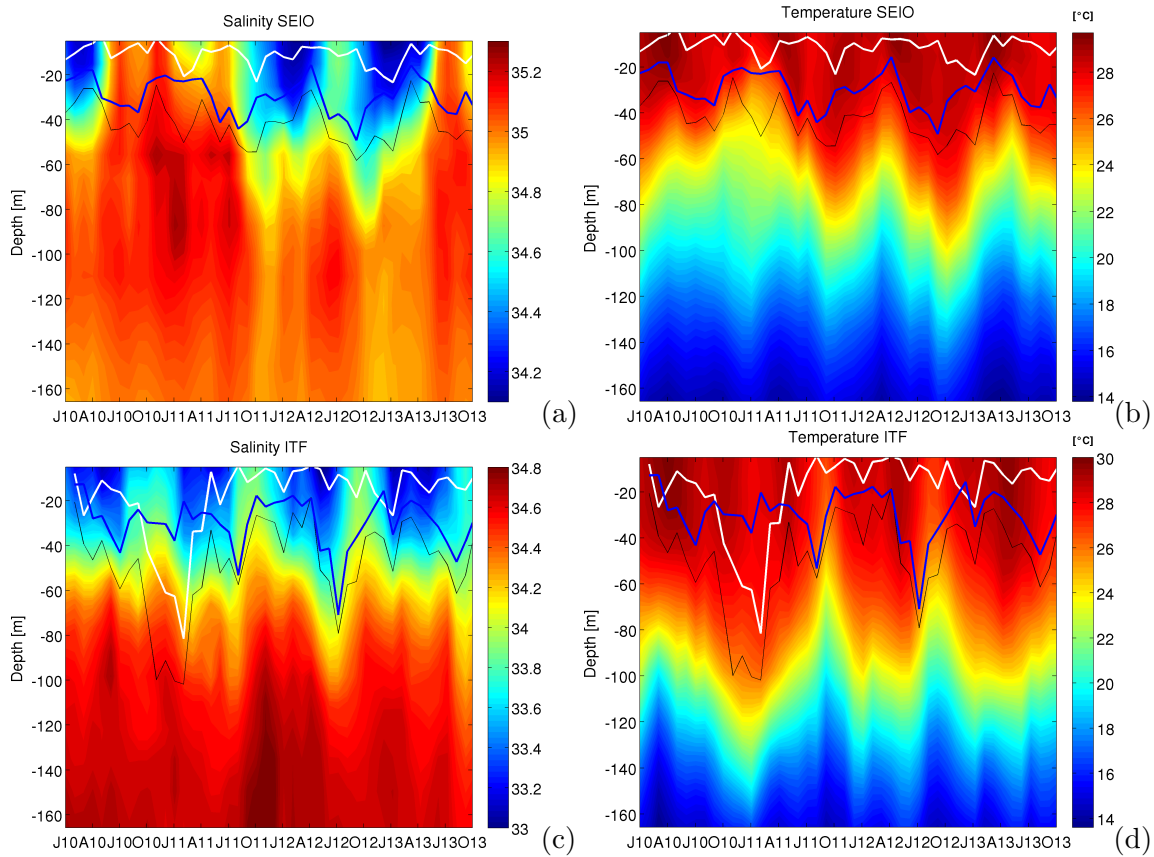


Figure 4.21: Time-depth plot of Argo salinity (left) and temperature (right) for (a,b) SEIO and (c,d) ITF for January 2010 to December 2013. The blue line is the mixed layer depth, the black line represents the isothermal layer depth and the barrier layer thickness is represented by the white line.

of low-salinity waters and, therefore, enhanced haline stratification. Between July and October 2012 MLS increases slightly, which again reflects the monsoon cycle with high-salinity water entering the region.

In the ITF region, the BLT increases during the N-IOD in 2010. The ILD is located in approximately 100 m depth and the BLT reaches values up to 80 m. At this time the MLS is lower than in the following season, too. The negative salinity anomaly is also well presented in the comparison of the time series in Fig. 4.7. MLD and ILD increase during summer monsoon and reach a maximum in the summer of 2012.

The deep ILD in 2010 and the shallower MLD disable vertical mixing, leading to an increase in SST.

The development of the P-IOD in 2011 starts with decreasing SST during the upwelling

season in May-June. In Fig.4.21d, a slightly lower temperature in the upper meters and also a shoaler ILD and MLD is shown. The Ekman pumping, linked to the anomalous easterlies shoals, the ILD and brings colder and high-salinity waters off Sumatra and Java to the surface. Figure 4.21c displays the temporal development of the salinity in the ITF region. The MLS is increased from the beginning of the upwelling season until the end of the year, indicating the transport of the high-salinity Sumatra-Java upwelling waters into the ITF region. MLD and ILD start to increase in the spring of 2012 due to the anomalous westerlies in this region. The deep thermocline in spring/summer 2012 limits the amount of cold and high-salinity waters entering the mixed layer during the upwelling process. The temperature anomaly is negative, which explains the distinct SST dipole, but this is not attributable to enhanced upwelling. As already discussed, the transition period from summer to winter monsoon is associated with westerlies. As described by *Lan (2012)* the deep thermocline during summer 2012 takes a shorter time to sink as a response to these westerlies, which may be the reason for the earlier decay of the P-IOD in 2012.

4.5 Concluding remarks

The signature of SSS variability on different timescales as seen by SMOS was analyzed with regard to its driving mechanisms. The annual cycle of salinity is mainly driven by surface fluxes and advection. Ekman upwelling is of importance in coastal areas and south of the equator directly north of the southeast trade winds. Comparisons with other datasets show that SMOS captures the variability in the interior but does not resolve the annual amplitudes in coastal areas. Approximately 50% of the total variability is explained by the annual and semiannual cycle (70% of total Argo SSS variability). SSS variability in SMOS results in a larger extent from year-to-year, intraseasonal variability and small-scale fluctuations in coastal areas.

During the study period from 2010 to 2013, a strong N-IOD occurred in 2010, while a weak and a moderate P-IOD occurred in 2011 and 2012, respectively. IOD events occur on interannual timescales with N-IOD events characterized by positive SST anomalies in the eastern Indian Ocean, negative SST anomalies in the western Indian Ocean and an opposite pattern during P-IOD events. IOD-related anomalies can also be found in SSS. During the N-IOD in 2010, positive SSS anomalies were observed south of the equator in the SEIO region between 70°E and 90°E, while negative anomalies were present in the ITF region near Sumatra and Java. Negative SSS anomalies can be found in the SEIO region, while positive SSS anomalies occurred near Sumatra and Java during the P-IOD events in

2011 and 2012.

The high spatial-temporal resolution of SMOS SSS allows the identification of driving mechanisms for the observed anomalies. Results confirm the findings of *Nyadjro and Subrahmanyam (2014)* and *Durand et al. (2013)* and show that horizontal advection and Ekman pumping are the main drivers for the salinity tendency observed in the SEIO region during the N-IOD in 2010. The former is dominated by the enhanced geostrophic flow due to the strengthening of the Yoshida-Wyrtki Jets that transport high-salinity waters into the SEIO region. The unusually strong westerlies lead to an intensified convergence at the equator and divergence south of it. The thermocline and pycnocline shoal during the N-IOD, bringing colder and high-salinity waters to the surface.

Enhanced precipitation drives the negative salinity tendency near Sumatra and Java. In the ITF region, zonal salinity advection is reduced during the N-IOD event. This is due to the weakened trade winds that usually transport upwelled water off Sumatra and Java (upwelling season from June to September) to the west. The deep thermocline and shallow pycnocline inhibit upwelling of cold and high-salinity waters during the N-IOD, resulting in a further increase of SST. This process is known as Bjerknes feedback.

The analysis of the interannual variability of the salinity budget shows large differences in the characteristics of the P-IOD events in 2011 and 2012. An intercomparison shows that despite the strong SST dipole during the peak phase in 2012, the SSS-related P-IOD characteristics are less distinct than in 2011. SSS dynamics during the P-IOD events are mainly driven by surface fluxes and horizontal advection. During the P-IOD in 2012, the horizontal salinity advection of high-salinity upwelled waters off Sumatra and Java is reduced, and, therefore, the amplitude of salinity tendency is less than in 2011. The modulation of the P-IOD characteristics is attributable to the influence of intraseasonal variability with timescales less than 3 months.

Active MJO phases are associated with enhanced precipitation and anomalous zonal winds to the east and west of the convective center that are present during the spring of 2012. The anomalous westerlies lead to a deepening of the thermocline in the southeastern Indian Ocean, suppressing the upwelling of colder and high-salinity waters off Sumatra and Java. The wavelet analysis of MJO-related variables with a temporal resolution between 1 and 7 days shows coherent patterns of variability with periods between 30-90 days and demonstrates the importance of the MJO in the Indian Ocean.

The intraseasonal variability of the zonal wind velocities for the SEIO and ITF region is also increased during active MJO phases. Stronger westerlies transport high-salinity waters into regions south of the equator, which counteracts the development of negative

SSS anomalies in the SEIO region despite enhanced rainfall. The MJO-related processes modulate the characteristics of the P-IOD in 2012.

These results show the importance of further and detailed studies, taking into account the variable wind regime and barrier layer dynamics. I concentrated on the influences on the variability in the IOD-relevant boxes, but MJO-related variations happen also north of the equator with different effects on local dynamics.

Guan et al. (2014) analyzed Aquarius SSS anomalies under the MJO with the result that MJO-related SSS changes cannot solely be explained by E-P but also by ocean dynamics, especially in the eastern Indian Ocean. They furthermore disagree with the interpretation by *Grunseich et al. (2013)*, that the SSS anomalies in the eastern Indian Ocean are consistent with E-P.

Wilson et al. (2013) investigated the effect of the IOD on the MJO, focusing on events between August and November with the result that the eastern Indian Ocean appears less favorable for the development of the MJO during P-IOD events than during N-IOD events. The wavelet analysis presented here confirms this, indicating high OLR power during the N-IOD in 2010 and less power during the second half of 2012.

In summary, it can be said that satellite-retrieved SSS is a reliable tracer for analyzing the SSS variability in the Indian Ocean on interannual and intraseasonal timescales. SMOS SSS is noisy in coastal areas and does not allow the analysis of IOD-related SSS variabilities in the Bay of Bengal or Arabian Sea. *Saji et al. (1999)* showed that freshwater flux anomalies during IOD events in the Bay of Bengal can also be observed. During P-IOD events, anomalous convergence patterns over the Bay of Bengal lead to enhanced rainfall (*Qiu et al. (2014)* and *Ashok et al. (2004)*). Aquarius shows negative SSS anomalies between July and October 2012 which can be caused by the P-IOD.

Aquarius and Argo show large SSS anomalies during March 2012 which may be due to the influence of the active MJO.

The intercomparison between interannual SSS variability of Argo, SMOS and STORM indicated that the model underestimates the variability (compare Fig. 4.12) in the central Indian Ocean. Therefore it was not considered for further analyses. The underestimation of interannual variability is most likely due to the relaxation of SSS to the monthly climatology, leading to a damping of the interannual variability.

Chapter 5

Summary and Outlook

In this thesis, the sea surface salinity variability and its underlying mechanisms were investigated using satellite data. First, the quality of spaceborne SSS measurements in less continuously sampled ocean areas was examined. The quality assessment was based on time series of satellite-retrieved, *in situ* and simulated SSS, that are often well correlated. Average differences between SMOS SSS and *in situ* data range between 1.2 in the high latitudes and <0.1 in the tropical regions far away from coasts. The main error sources of these large differences are the limited radiometer accuracy, coastal effects, geophysical biases, inaccuracies in the sea surface roughness assumption, RFI and SST-related biases. The validation study focuses on the northern North Atlantic and shows for the first time that relative to ship-based *in situ* salinity measurements, SMOS and Aquarius SSS fields reproduce well the spatial and temporal variations of the SSS during the period from May 2012 to April 2013. Data before May 2012 were corrupted by RFI in this region. The average difference to independent ship-based thermosalinograph (TSG) data can be reduced substantially from 1.2 to 0.1 by an SST-dependent bias correction inferred empirically as a relation between satellite and Argo data in the North Atlantic between 20°N and 80°N . The average root-mean-square difference can be reduced from 1.5 to 0.9 through the bias correction. The remaining root-mean-square difference between *in situ* and satellite data can be attributed to short-term and small-scale (<30 days, $<1^{\circ}$) ocean processes and may represent associated sampling errors, large near strong currents and near the outflow of major rivers. The bias-corrected satellite SSS retrievals are reasonably suitable for observing SSS changes on annual timescales.

The second region under investigation, is the Indian Ocean. It is one of the least sampled oceans with large SSS variability on different timescales (*Nyadjro and Subrahmanyam,*

2014). Here, the data quality of satellite-retrieved SSS is encouraging, thus contributing to the second major aspect of this thesis: the investigation of SSS dynamics in the low- and high-frequency range and its driving mechanisms. Here, the focus is on the Indian Ocean Dipole (IOD) which varies on interannual timescales and interacts with the intraseasonal Madden-Julian Oscillation (MJO). The analysis is based on a number of observational, reanalysis and model datasets including satellite-retrieved SSS and *in situ* SSS, SST, E-P, wind velocity and OLR for the period from January 2010 to December 2013. During this period, a strong N-IOD occurred in 2010, while a weak and a moderate P-IOD occurred in 2011 and 2012, respectively. Analyses of monthly SSS anomalies show that SMOS and Aquarius capture the large anomalous IOD-related signals in the central Indian Ocean. Combined with the auxiliary data, the interannual variability of the salinity budget terms was quantified. During the N-IOD in 2010, horizontal advection and subsurface processes are the main drivers for the positive salinity tendency in the central Indian Ocean, whereas enhanced precipitation and advection drive the negative SSS anomalies found in the eastern Indian Ocean.

The strength of the P-IOD events as well as the processes driving the observed salinity tendency vary between 2011 and 2012. P-IOD events are accompanied by a cooling off Sumatra-Java and a warming off Somalia in combination with anomalous easterlies along the equator during the boreal fall. The easterly alongshore winds off Sumatra and Java favor the upwelling in the eastern Indian Ocean (*Sakova, 2010*).

The upwelling of cold, high-salinity waters off Sumatra and Java is reduced during the P-IOD in 2012 and, therefore, the amplitude of salinity tendency is less than in 2011 despite the strong SST dipole during the peak phase. The modulation of the P-IOD characteristics may be attributable to the influence of the active MJO phase propagation in spring 2012. The associated anomalous westerlies lead to a deeper thermocline in the east, which inhibits the upwelling and leads to an earlier decay of the SST dipole due to increasing SST. Confirmed here is that subsurface processes and barrier layer dynamics play an important role for the development and the decay of IOD events in the Indian Ocean.

The wavelet analysis of OLR and SSS indicate, that the IOD and MJO interact with each other. Not only the active MJO in spring 2012 modulates the P-IOD characteristics, but also the conditions during the N-IOD seem to be favorable for MJO activity, thus confirming the findings of *Wilson et al. (2013)*.

The salinity budget based on SMOS and Argo SSS is nearly closed during the N-IOD in 2010, and the averaged residual is <0.05 over the 4-year period. Residuals are due to mixing processes and diffusion, which are not considered. Data errors are also included in

the residual. Huge errors can be found during the generation of the Yoshida-Wyrtki Jets in spring, indicating an underestimation of the advection term in the salinity budget. SMOS captures the SSS variability on different timescales and helps to analyze the relationship between different mvariability modes.

Beside the first-time validation of satellite-retrieved SSS data obtained in high northern latitudes and the development of a SST-dependent correction method, this study shows for the first time the development of IOD events under the influence of MJO events using satellite-retrieved SSS data.

MJO and IOD events affect the weather of neighboring regions, such as Australia, India and East Africa. During P-IOD events drier conditions occur over Australia and Indonesia and induce droughts, bushfires and coral reef death across western Sumatra while conditions over East Africa and India are unusually wet, triggering floods that may lead to epidemic outbreaks (e.g. malaria) in eastern Africa (*Hashizume et al., 2012*). As described by *Hashizume et al. (2012)*, the consequences of the extreme P-IOD event in 1997 caused a death toll of several thousands and hundreds of thousands of displaced people during floods in eastern Africa. At the same time, the neighboring regions of the eastern Indian Ocean suffered from droughts and bushfires, and the associated smoke led to severe health problems for tens of millions of people (*Cai et al., 2014*).

During N-IOD events, wetter conditions are present over Australia and Indonesia. The Queensland floods in 2010 and 2011 can be attributed to the strong N-IOD in 2010, which concurred with a moderate La Niña. Climate models suggest that with future climate change, the number of extreme P-IOD events is likely to increase (*Ng et al. (2015)* and *Cai et al. (2014)*). The amplitude of positive events is generally greater than that of negative events (*Ng et al., 2015*). Global warming is expected to lead to stronger easterlies in the boreal fall and faster warming of SST in the western Indian Ocean, compared to the eastern Indian Ocean, where the shoaling thermocline brings colder water to the surface, leading to a further decrease of SST. The associated wind and ocean current anomalies are likely to turn moderate P-IODs more extreme, all with tremendous impact on surrounding regions (*Ng et al., 2015*).

The ENSO cycle influences the IOD and MJO cycle. Strong MJO phases are observed during weaker La Niña or neutral years, whereas weaker phases are often associated with strong El Niño years (*Zhang, 2005*). A weak La Niña was present during the first three months of 2012. It was replaced by ENSO-neutral conditions for the remainder of the year (*NOAA, 2013*). The strengthening of the Pacific trade winds during La Niña enhances the pressure gradient between the Pacific and the Indian Ocean (*Lee et al., 2015*). The

pressure gradient drives the Indonesian Throughflow bringing warm, low-salinity waters from the Pacific into the Indian Ocean (*Schiller et al., 2006*), and it may also affect the SSS distribution.

During the end of the analyses in the fall of 2015, a strong P-IOD develops concurrently with a strong El Niño. A main point for future work is to figure out how these modes (ENSO, IOD) interact with the MJO and how sensitive SSS is to these influences. Despite of the P-IOD, the summer monsoon over the southern Indian subcontinent in 2012 was one of the driest in the last 65 years (*Wenqing Tang, personal communication*). As described by *Ordonez et al. (2013)*, the MJO modulates the intraseasonal variability of the Indian summer monsoon rainfall. Dependent on the MJO phase, rainfall anomalies can be shifted from the southern Indian subcontinent to the northern Indian subcontinent (*Ordonez et al., 2013*). To investigate the role of the ocean in modulating the summer monsoon characteristics of 2012 could also be of interest in future works. Another open question is to what extent SST variability affects MJO, should be analyzed in detail with regard to barrier layer dynamics.

The influence of the Indian Ocean subtropical dipole (IOSD) on the IOD characteristics should also be investigated. The IOSD is described by a SST dipole between the southwestern Indian Ocean (south of Madagascar) and the eastern Indian Ocean (i.e. off Australia). IOSD is suspected to impact the position of the Mascarene high, and thus, to influence the Indian summer monsoon and also may trigger the IOD (*Feng et al., 2014*).

SSS remote sensing is still at the beginning. However, after 5 years of SSS monitoring from space, variability from the high- to the low-frequency range with periods of up to two years can be seen. The disagreement between previous studies on the driving mechanisms for the MJO-related SSS variability shows that our understanding of the relationships between the various modes and their interaction is still limited. Here, more studies are required. Satellite-retrieved SSS reflects the processes at the surface. Fast processes are resolvable, which are not as easy to detect with *in situ* measurements at a depth of 5 m. An extension of this study constitutes the investigation of longer time series including the Pacific Ocean. The influence of mixing and diffusion should also be implemented in the analysis to close the salinity budget and clarify the origin of data errors. With longer time series and better SSS retrieval quality, it would be possible to analyze the functioning of the coupled ocean-atmosphere system. A more thorough understanding of the relationship of these modes and extreme weather events as well as the variability induced by climate change will help to provide greater confidence in predicting extreme weather events. In addition, it will enable society, industry and governments to prepare for the increased risk

of droughts, bushfires and other natural disasters in the Indian Ocean region.

Appendix A

Frequency analyses

A.1 Fourier transform

A time series can be represented by a linear combination of sines and cosines of the form:

$$y(t) = \sum_{k=0}^{\infty} [A_k \cos(\omega_k t + B_k(\omega_k T))], \quad (1.1)$$

with the frequency ω_k of k-th harmonic and the total length T of the time series of the signal:

$$\omega_k = \frac{2\pi k}{T}. \quad (1.2)$$

A transformation of Eqn. 1.1 leads to

$$y(t) = \sum_{k=0}^{\infty} C_k \cos(\omega_k t - \varphi_k), \quad C_k = \sqrt{A_k^2 + B_k^2} \quad (1.3)$$

C_k and φ_k are amplitude and phase of the harmonic. In the case of a time series with N samples sampled at equal time intervals dt a Fourier transform can be modified to the discrete Fourier transform (DFT), which takes advantage of the discrete form of the signal (*Sakova, 2010*). The DFT of a signal x of length n is:

$$X_m = dt \sum_{n=0}^{N-1} x_n \cdot e^{-j2\pi \frac{nm}{N}} \quad (1.4)$$

For the inverse DFT it holds:

$$x_n = \sum_{m=0}^{N-1} X_m \cdot e^{j2\pi \frac{nm}{N}} \quad (1.5)$$

An exact reconstruction of the signal without any loss of information is only possible when a continuous time signal has frequencies lower than half of the sampling rate (Shannon theorem). "The critical sampling rate equal to twice the highest frequency present in the signal is referred to as the Nyquist sampling rate $F_N = 2f_{max}$. For meaningful results of the DFT it is necessary to ensure a sampling rate greater than the Nyquist frequency." –*Sakova (2010)*. The fast Fourier transform performs DFT of samples containing certain numbers of points. Fast Fourier transform (FFT) algorithms have computational complexity $O(n \log n)$ instead of $O(n^2)$, where n is the data size. The data analysis was conducted using Matlab based on the Fast Fourier transform (FFT) and the Inverse Fast Fourier transform (IFFT) functions.

A.2 Wavelet transform

For studying the temporal behavior of a signal, one can apply wavelet transform to the time series of a signal. For this purpose, software provided by C. Torrence and G. Compo (<http://paos.colorado.edu/research/wavelets>) was used and adjusted. For calculating the cross wavelet transform of two signals, cross wavelet and wavelet coherence software provided by A. Grinsted was used. A practical guide to Wavelet analysis is given by *Torrence and Compo (1997)* as well as *Grinsted et al. (2004)* and will be shortly summarized in the following: A wavelet is a basis function that is isolated with respect to time Δt and frequency $\Delta \omega$. Each wavelet has a characteristic location and scale. A father wavelet characterizes the basic wavelet scale, the mother wavelet characterizes the basic wavelet shape. One particular mother wavelet – Morlet – is defined as:

$$\psi_0(\eta) = \pi^{-1/4} e^{i\omega_0\eta} e^{-1/2\eta^2} \quad (1.6)$$

with the dimensionless frequency ω_0 and the dimensionless time η_0 . A wavelet transform is the representation of a function in real space as a linear combination of wavelet basis functions. "The wavelet is applied as a band pass filter to the time series. The wavelet is stretched in time by varying its scale s so that $\eta = s \cdot t$." –*Grinsted et al. (2004)*. The continuous wavelet of a signal with discrete time steps dt is defined as the convolution of the signal with scaled and normalized wavelet.

$$W_n^X = \sqrt{\frac{dt}{s}} \sum_{n'=1}^N x_n \psi_0 \left[(n' - n) \frac{dt}{s} \right] \quad (1.7)$$

Following *Grinsted et al. (2004)* the wavelet power is defined as the power of two from W_n^X with the complex argument as the local phase. A continuous wavelet transform has

boundary artifacts because of the incomplete localization in time. Therefore, the cone of influence (COI) is introduced. In it, boundary effects can be ignored. The COI is defined as the area of wavelet power that has dropped to e^{-2} by the discontinuity at the boundary. "The statistical significance of wavelet power can be expressed relative to the null hypothesis that the signal is generated by a stationary process with a given background power spectrum" – *Torrence and Compo (1997)*. The background spectrum is modeled by a first order autoregressive (AR1 or Marcov) process. The Fourier power spectrum is given by *Torrence and Compo (1997)*:

$$P_k = \frac{1 - \alpha^2}{|1 - \alpha e^{-2i\pi k}|^2} \quad (1.8)$$

with the lag-1 autocorrelation α and the Fourier frequency index k . With $\alpha = 0$ Eqn. 1.8 gives white noise. As described by *Torrence and Compo (1997)*, the wavelet transform is a series of band pass filters of a time series where the wavelet scale is linearly related to the characteristic period of the filter. From the wavelet transform of two time series the cross wavelet transform can be constructed, which exposes regions with high common power. The cross wavelet transform of two time series is defined as $W^{xy} = W^X W^{Y*}$, where $*$ denotes complex conjugation. Following *Torrence and Compo (1997)* and *Grinsted et al. (2004)*, the cross wavelet power of two time series with the specific background spectra P_k^X and P_k^Y is given as:

$$D \left(\frac{W_n^X(s) W_n^{Y*}(s)}{\sigma_X \sigma_Y} < p \right) = \frac{Z_\nu(p)}{\nu} \sqrt{P_k^X P_k^Y}. \quad (1.9)$$

$Z_\nu(p)$ is the confidence level associated with the probability. A detailed description of the cross wavelet transform and wavelet coherence to geophysical time series is given in *Grinsted et al. (2004)*

Appendix B

Salinity budget in the tropical Indian Ocean during the 4-year period 2010 to 2013

Figure B.1a,c shows the horizontal distribution of E-P and P during the N-IOD event in 2010. An intercomparison between the E-P and P patterns with the horizontal distribution of SEF (compare Fig.4.11) indicates that P contributes most to SEF. The same can be seen in Fig. B.1b,d, which shows the horizontal distribution of E-P and P during the weak P-IOD in 2011 (August-October).

Figure B.2a,b presents the temporal development of the box-averaged salinity budget components for the SEIO and ITF region. In both regions, the terms show high variability but the annual variation of different terms due to the monsoon cycle can be observed. On an annual timescale the ST is mainly driven by ADV and SEF. This was already discussed in Sect. 4.1.1 and is illustrated by the corresponding amplitude of ST, ADV and SEF in the SEIO region (see Fig. B.2a). In the SEIO region, ST is maximal during the summer season due to the advection of high-saline waters (compare black curve) from the Arabian Sea towards equatorial regions, starting in the summer monsoon.

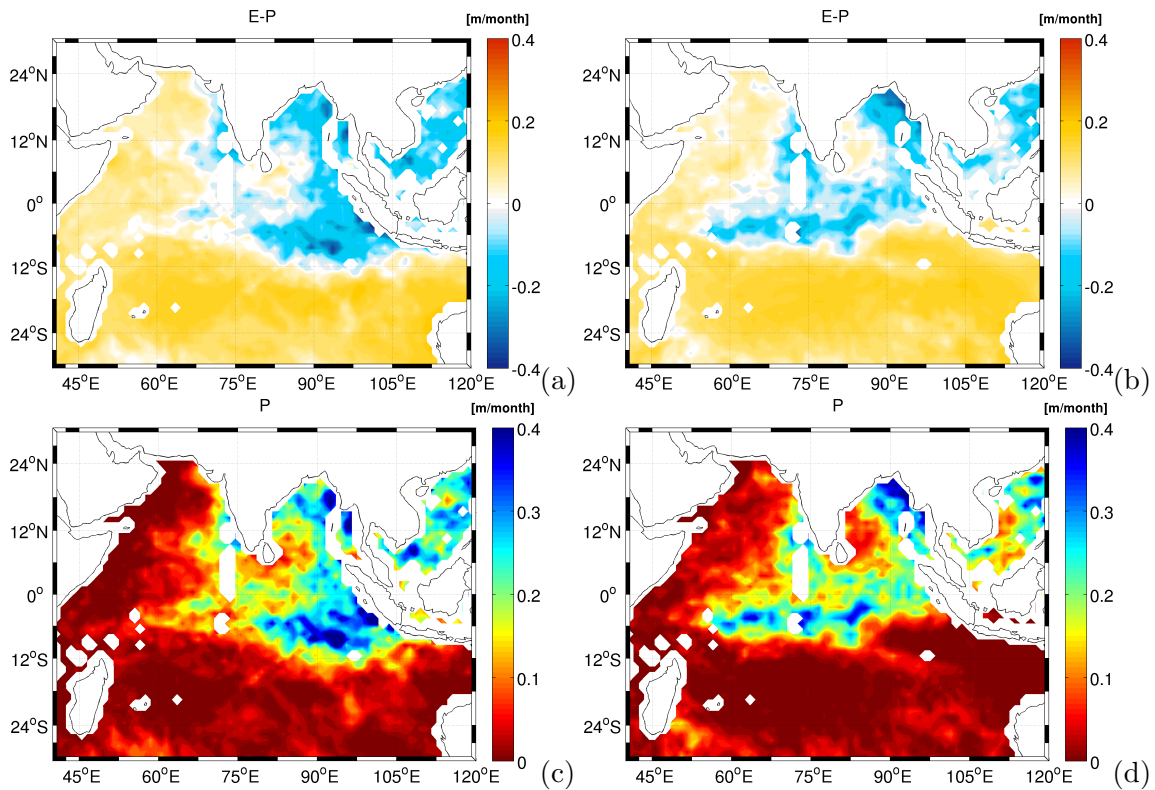


Figure B.1: Horizontal distribution of (a,b) evaporation minus precipitation ($E-P$) and (c,d) precipitation (P) for the period from August to October (left) 2010 and (right) 2011

SEF (blue) is negative in the fall and corresponds to negative ST amplitudes. In the SEIO region, vertical processes, including entrainment and Ekman pumping, are of importance as well. SUB is positive during the N-IOD in 2010, indicating upwelling, and negative during the P-IODs in 2011 and 2012, which indicating downwelling.

In the ITF region, ST is negative during the boreal spring season. ADV has larger amplitudes between April and October except in 2010. SEF peaks in January 2011 and 2012, which indicates enhanced precipitation. SUB has a minor influence on the ST in the ITF region. In August, ST decreases again due to the westward advection of low-saline waters from the Pacific Ocean.

As ADV showed to be of major influence for the ST, ADV is decomposed in its zonal and meridional components (Fig. B.2c,d). Figure B.2c,d illustrate that both meridional and zonal components are important, but the meridional component is better correlated with the total ADV (COR=0.8 in the SEIO region and 0.7 in the ITF region, >95% confidence level). Listed in Table B.1 is the correlation of the zonal and meridional components of ADV to the total ADV.



Figure B.2: Variation of box-averaged salinity budget components for (left) SEIO region and (right) ITF region. Top: Salinity tendency (ST, red), surface external forces (SEF, blue), advection (ADV, black) and subsurface influences (SUB, green). Center: Components of ADV: Sum of horizontal salinity ADV (black) decomposed into mean zonal geostrophic flow (-uG, magenta) and zonal Ekman ADV (-uEK, green) and meridional mean geostrophic flow (-vG, magenta dashed) and meridional Ekman ADV (-vEK, green dashed). Bottom: sum of the components (blue), observed salinity tendency from Argo MLS (black) and from SMOS (red)

Table B.1: Correlation of mean zonal geostrophic flow ($-uG$), mean meridional geostrophic flow ($-vG$), zonal Ekman component ($-uEK$) and meridional Ekman component ($-vEK$) to total ADV for the SEIO and ITF region. The correlations are significant at the 95% confidence level. Significance was calculated using student t test.

region	-uG	-vG	-uEK	-vEK
SEIO	0.6	0.1	0.41	0.73
ITF	0.6	0.1	0.16	0.57

The meridional ADV can mostly be explained by the meridional Ekman transport (green dashed line) which shows a correlation to total ADV of 0.73 in the SEIO region and 0.57 in the ITF region. The zonal mean geostrophic flow has a higher impact to zonal ADV and shows a correlation of 0.6 to total ADV in the SEIO and ITF region. Starting in the SEIO region (see Fig. B.2c), the meridional Ekman component of ADV increases during the summer months, describing the southward Ekman transport of less saline waters. The meridional Ekman component of ADV peaks in the fall and starts to decrease in November, which describes the northward Ekman transport during the winter monsoon. During the N-IOD in 2010, the meridional Ekman component of ADV is less pronounced. At this time, the zonal and meridional geostrophic component of ADV is increased, which describes the transport of high-saline waters due to the strengthening of the Yoshida-Wyrtki Jets in the region. Further southeast in the ITF region, the meridional Ekman component of horizontal ADV shows a clear annual cycle with maximum ADV in April/May (see Fig. B.2d). In October 2010, meridional ADV (vG and vEK) is higher than in October 2011 and October 2012. In 2011 the maximum in ADV is less pronounced. Meridional Ekman transport is reduced, too, due to anomalous Ekman transport induced by the weak trade winds.

Figure B.2e,f shows the sum of the salinity budget components (SUM) and the ST for SMOS SSS and Argo MLS for the different regions. In the SEIO region, the MLS budget is nearly closed during the N-IOD event in 2010 and the P-IOD event in 2012. Here, the residual R is $<0.03 \text{ month}^{-1}$. This R may result from enhanced mixing processes, diffusion and estimation errors in the process terms. In contrast, the discrepancies between the SUM and the ST are large during April-May/June, the generation of the Yoshida-Wyrtki Jet in spring, reaching amplitudes $>0.2 \text{ month}^{-1}$. This may be attributable to the underestimation of horizontal ADV. Overall, the box-averaged R over the 4-year period is 0.03 month^{-1} for the SEIO box and 0.07 month^{-1} for the ITF box.

Bibliography

- Akhil, V. P., F. Durand, M. Lengaigne, J. Vialard, M. G. Keerthi, V. V. Gopalakrishna, C. Deltel, F. Papa, and C. de Boyer Montégut (2014), A modeling study of the processes of surface salinity seasonal cycle in the Bay of Bengal, *J. Geophys. Res.: Oceans*, *119*, 3926–3947, doi:10.1002/2013JC009632.
- Allen, M. R., and W. J. Ingram (2002), Constraints on future changes in climate and the hydrologic cycle, *Nature*, *419*, 224–232, doi:10.1038/nature01092.
- Aretxabaleta, A., J. Gourrion, J. Ballabrera, R. Sabia, A. Turiel, J. Font, and R. W. Schmitt (2010), Bridging the gap between surface salinity satellites: SMOS and Aquarius, *Proc. ESA Living Planet Symposium, Bergen, Norway, ESA SP-686*, 5 pp.
- Ashok, K., Z. Guan, and T. Yamagata (2003), A look at the relationship between the ENSO and the Indian Ocean Dipole, *J. Meteorol Soc. Jpn.*, *81*(1), 41–56.
- Ashok, K., Z. Guan, N. H. Saji, and T. Yamagata (2004), Individual and combined influences of ENSO and the Indian Ocean Dipole on the Indian Summer Monsoon, *Journal of Climate*, *17*, 3141–3155, doi:10.1175/1520-0442(2004)017<3141:IACIOE>2.0.CO;2.
- Aslebagh, S. (2013), *Development of an oceanic rain accumulation product in support of sea surface salinity measurements from Aquarius/SAC-D*, MA thesis, University of Central Florida, Orlando, Florida.
- Banks, C., C. Gommenginger, M. Srokosz, and H. Snaith (2012), Validating SMOS ocean surface salinity in the Atlantic with Argo and operational ocean model data, *IEEE T. Geosci. Remote*, *50*(5), 1688–1702, doi:10.1109/TGRS.2011.2167340.
- Benshila, R., F. Durand, S. Masson, R. Bourdalle-Badie, C. de Boyer Montegut, F. Papa, and G. Madec (2014), The upper Bay of Bengal salinity structure in a high-resolution model, *Ocean Modelling*, *74*, 36–52, doi:10.1016/j.ocemod.2013.12.001.

- Boutin, J., N. Martin, G. Reverdin, X. Yin, and F. Gaillard (2013), Sea surface freshening inferred from SMOS and ARGO salinity: impact of rain, *Ocean Sci.*, *9*(1), 183–192, doi:10.5194/os-9-183-2013.
- Boutin, J., N. Martin, G. Reverdin, S. Morisset, X. Yin, L. Centurioni, and N. Reul (2014), Sea surface salinity under rain cells: SMOS satellite and in situ drifter observations, *J. Geophys. Res.: Oceans*, doi:10.1002/2014JC010070.
- Boyer, T. P., and S. Levitus (2002a), Harmonic Analysis of climatological sea surface salinity., *J. Geophys. Res.*, *107*, doi:10.1029/2001JC000829.
- Brandt, P., L. Stramma, F. Schott, J. Fischer, M. Dengler, and D. Quadfasel (2002), Annual Rossby waves in the Arabian Sea from TOPEX/POSEIDON altimeter and in situ data, *Deep-Sea Res. Pt. 2*, *42*, 1197–1210.
- Cai, W., G. Santoso, E. Weller, L. Wu, K. Ashok, Y. Masumoto, and T. Yamagata (2014), Increased frequency of extreme Indian Ocean Dipole events due to greenhouse warming, *Nature*, *510*, doi:10.1038/nature13327.
- Corbella, I., N. Duffo, M. C. A. Vall-llossera, and F. Torres (2004), The visibility function in interferometric aperture synthesis radiometry, *IEEE T. Geosci. Remote*, *42*(8), 1677–1682.
- Corbella, I., F. Torres, A. Camps, N. Duffo, and Vall-llossera (2009), Brightness-temperature retrieval methods in synthetic aperture radiometers, *IEEE T. Geosci. Remote*, *47*(1), 285–294.
- Cushman-Roisin, B., and J.-M. Beckers (2011), *Introduction to geophysical fluid dynamics*, 2 ed., Dartmouth College, New Hampshire, USA: Academic Press.
- Daganzo-Eusebio, E., R. Oliva, Y. H. Kerr, S. Nieto, P. Richaume, and S. Mecklenburg (2013), SMOS radiometer in the 1400-1427-MHz passive band: Impact of the RFI environment and approach to its mitigation and cancellation, *IEEE T. Geosci. Remote*, *51*(10), 4999–5007.
- de Boyer Montégut, C., G. Madec, A. S. Fischer, A. Lazar, and D. Iudicone (2004), Mixed layer depth over the global ocean: An examination of profile data and a profile-based climatology, *J. Geophys. Res.: Oceans*, *109*, doi:10.1029/2004JC002378
- Dee, D. P., et al. (2011), The ERA-Interim reanalysis: configuration and performance of the data assimilation system, *Q. R. Meteor. Soc.*, *137*(656), 553–597, doi:10.1002/qj.828.

- Donguy, J.-R., and G. Meyers (1996), Seasonal variation of sea surface salinity and temperature in the tropical Indian Ocean, *Deep-Sea Res. Pt. 1*, *43*(2), doi:10.1016/0967-0637(96)00009-X.
- Donlon, C. J., M. Martin, J. Stark, J. Roberts-Jones, E. Fiedler, and W. Wimmer (2012), The operational sea surface temperature and sea ice analysis (OSTIA) system, *Remote Sens. Environ.*, *116*, 140–158, doi:10.1016/j.rse.2010.10.017.
- Drucker, R., and S. C. Riser (2014), Validation of Aquarius sea surface salinity with Argo: Analysis of error due to depth of measurement and vertical salinity stratification, *J. Geophys. Res.: Oceans*, doi:10.1002/2014JC010045.
- Drushka, K., J. Sprintall, and S. T. Gille (2014), Subseasonal variations in salinity and barrier-layer thickness in the eastern equatorial Indian Ocean, *J. Geophys. Res.: Oceans*, *119*, 805–823, doi:10.1002/2013JC009422.
- Ducet, N., P. Y. Le Traon, and G. Reverdin (2000), Global high-resolution mapping of ocean circulation from TOPEX/POSEIDON and ERS-1 and -2, *J. Geophys. Res.: Oceans*, *105*(C8), 19,477–19,498, doi:10.1029/2000JC900063.
- Durack, P. J. (2011), Global ocean salinity: a climate change diagnostic, Ph.D. thesis, University of Tasmania, Australia.
- Durack, P. J., and S. E. Wijffels (2010), Fifty-year trends in global ocean salinities and their relationship to broad-scale warming., *J. Climate*, *23*, 4342–4362, doi:10.1175/2010JCLI3377.1.
- Durand, F., F. Papa, A. Rahman, and S. K. Bala (2011), Impact of Ganges-Brahmaputra interannual discharge variations on Bay of Bengal salinity and temperature during 1992–1999 period, *J. Earth Syst. Sci.*, *120*(5), 859–872.
- Durand, F., G. Alory, R. Dussin, and N. Reul (2013), SMOS reveals the signature of Indian Ocean Dipole events, *Ocean Dynam.*, *63*(11-12), 1203–1212, doi:10.1007/s10236-013-0660-y.
- ESA (2010), SMOS Mission - Operating Principles, Website, online, October 2015: http://m.esa.int/Our_Activities/Observing_the_Earth/The_Living_Planet_Programme/Earth_Explorers/SMOS/Overview3.
- ESA (2012), SMOS satellite measurements improve as ground radars switch off, Website,

- online, October 2015: http://www.esa.int/Our_Activities/Observing_the_Earth/SMOS_satellite_measurements_improve_as_ground_radars_switch_off.
- Earth and Space Research (2015), Mixed layer: definition., Website, online, October 2015: https://www.esr.org/outreach/glossary/mixed_layer.html.
- Felton, C. S., B. Subrahmanyam, V. S. N. Murty, and J. F. Shriver (2014), Estimation of the barrier layer thickness in the Indian Ocean using Aquarius Salinity, *J. Geophys. Res.: Oceans*, 119, 4200–4213, doi:10.1002/2013JC009759.
- Feng, J., D. Hu, and L. Yu (2014), How does the Indian Ocean subtropical dipole trigger the tropical Indian Ocean dipole via the Mascarene high, *Acta Ocanol. Sin*, 33(1), 64–76, doi:10.1007/s13131-014-0425-6.
- Feng, M., and G. Meyers (2003), Interannual variability in the tropical Indian Ocean: a two-year time-scale of Indian Ocean Dipole, *Deep-Sea Res. Pt 2*, 50(12), 2263–2284.
- Font, J., G. S. E. Lagerloef, D. L. Vine, A. Camps, and O. Zanife (2004), The determination of surface salinity with the European SMOS space mission, *IEEE T. Geosci. Remote*, 42, 2196–2205.
- Font, J., et al. (2013), SMOS first data analysis for sea surface salinity determination, *Int. J. Remote Sens.*, 34(9-10), 3654–3670, doi:10.1080/01431161.2012.716541.
- Gabarro, C., M. Portabella, M. Talone, and J. Font (2009), Toward an optimal SMOS ocean salinity inversion algorithm, *IEEE Geosci. Remote S.*, 6(3), 509–513, doi:10.1109/LGRS.2009.2018490.
- Gabarro, C., J. Martinez, and J. Font (2012), Impact of the Land-Sea contamination on SMOS retrieved salinity., *Tech. Rep. 1.0*, SMOS Barcelona Expert Centre.
- Gambau, V. G. (2012), *Contribution to the characterization of interferometric radiometers devoted to Earth observation: application to the MIRAS/SMOS payload*, Ph.D. thesis, Universitat Politecnica de Catalunya, Barcelona, Spain.
- Good, S. A., M. J. Martin, and N. A. Rayner (2013), EN4: Quality controlled ocean temperature and salinity profiles and monthly objective analyses with uncertainty estimates, *J. of Geophys. Res.: Oceans*, 118(12), 6704–6716, doi:10.1002/2013JC009067.
- Grinsted, A., J. C. Moore, and S. Jevrejeva (2004), Application of the cross wavelet transform and wavelet coherence to geophysical time series, *Nonlin. Processes Geophys.*, 11, 561–566, doi:10.5194/npg-11-561-2004.

- Grunseich, G., B. Subrahmanyam, V. S. N. Murty, and B. S. Giese (2011a), Sea surface salinity variability during the Indian Ocean Dipole and ENSO events in the tropical Indian Ocean, *J. Geophys. Res.: Oceans*, *116*(C11), doi:10.1029/2011JC007456.
- Grunseich, G., B. Subrahmanyam, and A. Arguez (2011b), Influence of the Madden-Julian Oscillation on sea surface salinity in the Indian Ocean, *Geophys. Res. Lett.*, *38*(L17605), doi:10.1029/2011GL049047.
- Grunseich, G., B. Subrahmanyam, and B. Wang (2013), The Madden-Julian oscillation detected in Aquarius salinity observations, *Geophys. Res. Lett.*, *40*, 5461–5466, doi:10.1002/2013GL058173.
- Guan, B., T. Lee, D. J. Halkides, and D. E. Waliser (2014), Aquarius surface salinity and the Madden-Julian Oscillation: The role of salinity in surface layer density and potential energy, *Geophys. Res. Lett.*, *41*, 2858–2869, doi:10.1002/2014GL059704.
- Guillou, C., W. Ellison, L. Eymard, K. Lamkaouchi, C. Prigent, G. Delbos, G. Balana, and S. A. Boukabara (1998), Impact of new permittivity measurements on sea surface emissivity modeling in microwaves, *Radio Sci.*, *33*(3), 649–667.
- Hashizume, M., L. F. Chaves, and N. Minakawa (2012), Indian Ocean Dipole drives malaria resurgence in East African highlands, *Scientific Reports*, *Macmillan Publishers Limited*, *2*, doi:10.1038/srep00269.
- Helm, K. P., N. L. Bindoff, and J. A. Church (2010), Changes in the global hydrological-cycle inferred from ocean salinity, *Geophys. Res. Lett.*, *37*, doi:doi:10.1029/2010GL044222.
- Henocq, C., J. Boutin, F. Petitcolin, G. Reverdin, S. Arnault, and P. Lattes (2010), Vertical variability of near-surface salinity in the tropics: Consequences for L-band radiometer calibration and validation, *J. Atmos. Ocean. Tech.*, *27*, 192–203.
- Hosoda, S., T. Suga, N. Shikama, et al. (2009), Global surface layer salinity change detected by Argo and its implication for hydrological cycle intensification., *J. Oceanogr.*, *65*, 579–586.
- Isern-Fontanet, J., A. Turiel, E. García-Ladona, and J. Font (2007), Microcanonical multifractal formalism: Application to the estimation of ocean surface velocities, *J. Geophys. Res.: Oceans*, *112*(C5), doi:10.1029/2006JC003878, c05024.

- Johnson, E. S., F. Bonjean, G. S. E. Lagerloef, and J. T. Gunn (2006), Validation and error analysis of OSCAR sea-surface currents, *J. Atmos. Ocean. Tech.*.
- Kainulainen, J., A. Colliander, J. Closa, M. Martin-Neira, R. Oliva, G. Buenadicha, P. Rubiales Alcaine, A. Hakkarainen, and M. T. Hallikainen (2012), Radiometric performance of the SMOS reference radiometers—assessment after one year of operation, *IEEE T. Geosci. Remote*, *50*(5), 1367–1383.
- Kalnay, E., et al. (1996), The NCEP/NCAR 40-Year Reanalysis Project, *B. Am. Meteorol. Soc.*, *77*(3), 437–471, doi:10.1175/1520-0477(1996)077<0437:TNYRP>2.0.CO;2.
- Kara, A. B., P. A. Rochford, and H. E. Hurlburt (2000), An optimal definition for ocean mixed layer depth, *J. Geophys. Res.*, *105*(C7), 16,803–16,821.
- Kim, S., J. H. Lee, P. de Matthaeis, S. Yueh, C.-S. Hong, J.-H. Lee, and G. Lagerloef (2014), Sea surface salinity variability in the East China Sea observed by the Aquarius instrument, *J. Geophys. Res.: Oceans*, doi:10.1002/2014JC009983.
- Köhl, A., D. Stammer, and M. S. Martins (2014), Impact of assimilating surface salinity from SMOS on ocean circulation estimates, *J. Geophys. Res.: Oceans*, doi:10.1002/2014JC010040.
- Lagerloef, G., et al. (2008), The Aquarius/SAC-D Mission: Designed to meet the salinity remote-sensing challenge, *Oceanography*, *21*(1), 68–81.
- Lagerloef, G. S. E., C. T. Swift, and D. M. Le Vine (1995), Sea surface salinity: The next remote sensing challenge, *Oceanography*, *8*(2), 44–50.
- Lan, M. (2012), Analysis of 2012 Indian Ocean Dipole Behaviour, National University of Singapore, Department of Earth and Planetary Science, University of Tokyo PDF, online, October 2015: <https://www.s.u-tokyo.ac.jp/en/utrip/archive/2013/pdf/05MoLan.pdf>
- Large, W., and Pond (1981), Open Ocean momentum flux measurements in moderate to strong winds, *J. Phys. Oceanog.*, *11*, 324–336.
- Large, W., J. McWilliams and S. Doney (1994), Oceanic vertical mixing: A review and a model with nonlocal boundary layer parameterization, *Rev. Geophys.*, *32*, 363–403.
- Lee, T., G. S. E. Lagerloef, M. M. Gierach, H. Kao, S. Yueh, and K. Dohan (2012), Aquarius reveals salinity structure of tropical instability waves, *Geophys. Res. Lett.*, *39*, 1–6, doi:10.1029/2012GL052232.

- Lee, S.-K., W. Park, M. O. Baringer, A. L. Gordon, B. Huber, and Y. Liu (2015), Pacific origin of the abrupt increase in Indian Ocean heat content during the warming hiatus, *Nature Geosci.*, *8*, 445–449, doi:0.1038/ngeo2438.
- Li, Y., F. Wang, and W. Han (2013), Interannual sea surface salinity variations observed in the tropical North Pacific Ocean, *Geophys. Res. Lett.*, *40*(10), 2194–2199, doi:10.1002/grl.50429.
- Liebmann, B., and C. A. Smith (1996), Description of a complete (interpolated) outgoing longwave radiation dataset, *B. Am. Meteorol. Soc.*, *77*, 1275–1277.
- Liu, C., and R. P. Allan (2013), Observed and simulated precipitation responses in wet and dry regions 1850–2100, *Environ. Res. Lett.*, *8*(3), doi:10.1088/1748-9326/8/3/034002.
- Madden, R. A., and P. R. Julian (1972), Description of global-scale circulation cells in the tropics with a 40–50 day period, *J. Atmos. Sci.*, *29*.
- Marshall, A. G., and H. H. Hendon (2013), Impacts of the MJO in the Indian Ocean and on the Western Australian coast, *Clim. Dyn.*, doi:10.1007/s00382-012-1643-2.
- Marshall, J., A. Adcroft, C. Hill, L. Perelman, and C. Heisey (1997b), A finite-volume, incompressible Navier Stokes model for studies of the ocean on parallel computers, *J. Geophys. Res.*, *102*, 5753–5766.
- Martinez, J. (2013), Ocean RFI distribution, *Tech. Rep. 1.0*, SMOS Barcelona Expert Centre, Barcelona, Spain
- Martins, M. S., N. Serra, and D. Stammer (2014), Spatial and temporal scales of sea surface salinity variability in the Atlantic Ocean, *J. Geophys. Res.*, doi:10.1002/2015JC010895.
- Masumoto, Y., and G. Meyers (1998), Forced Rossby waves in the southern tropical Indian Ocean, *J. Geophys. Res.*, *103*(C12), 27.589–27.602.
- McMullan, K. D., M. Brown, M. Martin-Neira, W. Rits, S. Ekholm, J. Marti, and J. Lemanczyk (2008), SMOS: The payload, *IEEE T. Geosci. Remote*, *46*(3), 594–605, doi: 10.1109/TGRS.2007.914809.
- Meissner, T., F. Wentz, D. L. Vine, and J. Scott (2014), Aquarius salinity retrieval algorithm theoretical basis document (ATBD), Addendum 3, *Tech. rep.*, report number 060414, Remote Sensing Systems, Santa Rosa, CA.
- Morisset, S., et al. (2012), Surface salinity drifters for SMOS validation, *Mercator Ocean – CORIOLIS Quarterly Newsletter*, *45*, 33–37.

- Ng, B., W. Cai, K. Walsh, and A. Santoso (2015), Nonlinear processes reinforce extreme Indian Ocean Dipole events, *Sci. Rep.*, *5*(11697), doi:10.1038/srep11697.
- NOAA (2013), Global Analysis - Annual 2012, Website online: <https://www.ncdc.noaa.gov/sotc/global/201213>
- Nyadjro, E., and B. Subrahmanyam (2014), SMOS mission reveals the salinity structure of the Indian Ocean Dipole, *IEEE Geosci. Remote S.*, *11*(9), 1564–1568, doi:10.1109/LGRS.2014.2301594.
- O’Gorman, P. A., and T. Schneider (2009), The physical basis for increases in precipitation extremes in simulations of 21st-century climate change, *Proc. Natl Acad. Sci. USA*, *106*, 14,773–14,777, doi:10.1073/pnas.0907610106.
- Oliva, R., E. Daganzo, Y. Kerr, S. Mecklenburg, S. Nieto, P. Richaume, and C. Gruhier (2012), SMOS radio frequency interference scenario: Status and actions taken to improve the RFI environment in the 1400–1427 Mhz passive band, *IEEE T. Geosci. Remote*, *50*(5), 1427–1439, doi:10.1109/TGRS.2012.2182775.
- Oliva, R., M. Martin-Neira, I. Corbella, F. Torres, J. Kainulainen, J. Tenerelli, F. Cabot, and F. Martin-Porqueras (2013), SMOS calibration and instrument performance after one year in orbit, *IEEE T. Geosci. Remote*, *51*(1), 654–670, doi:10.1109/TGRS.2012.2198827.
- Ordonez, P., P. Ribera, D. Gallego, and C. Pena-Ortiz (2013), Influence of Madden-Julian Oscillation on water budget transported by Somali low-level jet and the associated Indian Summer Monsoon rainfall, *Water Resour. Res.*, *49*, 6474–6485, doi:10.1002/wrcr.20515.
- Parry, M. L., O. F. Canziani, J. Palutikof, P. van der Linden, and C. Hanson (2007), *Contribution of Working Group II to the Fourth Assessment Report of the Intergovernmental Panel on Climate Change*, Cambridge University Press, Cambridge, United Kingdom and New York, NY, USA.
- Qiu, Y., W. Cai, L. Li, and X. Guo (2012), Argo profiles variability of barrier layer in the tropical Indian Ocean and its relationship with the Indian Ocean Dipole, *Geophys. Res. Lett.*, *39*(L08605), doi:10.1029/2012GL051441.
- Qiu, Y., W. Cai, X. Guo, and B. Ng (2014), The asymmetric influence of the positive and negative IOD events on China, *Scientific Reports, Macmillan Publishers Limited*, *4*(4943), doi:10.1038/srep04943.

- Qu, T., S. Gao, and I. Fukumori (2011), What governs the North Atlantic salinity maximum in a global GCM, *Geophys. Res. Lett.*, *38*, doi:10.1029/2011GL046757.
- Rahmstorf, S. (2006), Thermohaline Ocean Circulation, *Encyclopedia of Quaternary Sciences*, Edited by S. A. Elias. Elsevier, Amsterdam 2006.
- Rao, R. R., and R. Sivakumar (2003), Seasonal variability of sea surface salinity and salt budget of the mixed layer of the north Indian Ocean, *J. Geophys. Res.*, *108*(C1), doi:10.1029/2001JC000907.
- Rao, S. A., V. V. Gopalakrishna, S. R. Shetye, and T. Yamagata (2002), Why were cool SST anomalies absent in the Bay of Bengal during the 1997 Indian Ocean Dipole Event, *Geophys. Res. Lett.*, *29*(11), doi:10.1029/2001GL014645.
- Reba, M. N. M., A. Z. Rosli, and N. A. Rahim (2014), Soil moisture ocean salinity (SMOS) salinity data validation over Malaysia coastal water, *IOP C. Ser.: Earth Env.*, *18*, doi:10.1088/1755-1315/18/1/012112.
- Reul, N., et al. (2013), Sea Surface Salinity Observations from Space with the SMOS Satellite: A New Means to Monitor the Marine Branch of the Water Cycle, *Surv. Geophys.*, pp. 1–42, doi:10.1007/s10712-013-9244-0.
- Saji, N. H., B. N. Goswami, P. N. Vinayachandran, and T. Yamagata (1999), A dipole mode in the tropical Indian Ocean, *Nature*, *401*, 360–363.
- Sakova, I. V. (2010), *Low-frequency modes of variability of the Indian Ocean and their connection with the Indian Ocean Dipole*, Ph.D. thesis, School of Geography and Environmental Studies, University of Tasmania, Tasmania.
- Schiller, A., S. E. Wijffels, and J. Sprintall (2006), *Variability of the Indonesian Throughflow: A review and model-to-data comparison*, p. 175ff, Elsevier Oceanography Series 73, Amsterdam, Netherlands.
- Schlundt, M. (2014), *Mixed layer heat and salinity variability in the equatorial Atlantic*, Ph.D. thesis, Christian-Albrechts-Universität zu Kiel, Kiel, Germany.
- Schott, F. A., and J. P. McCreary (2001), The monsoon circulation of the Indian Ocean, *Prog. Oceanogr.*, *51*, 1–123, doi:10.1.1.389.7796.
- Schott, F. A., S.-P. Xie, and J. P. M. Jr. (2009), Indian Ocean circulation and climate variability, *Rev. Geophys.*, *47*(1), doi:10.1029/2007RG000245.

- Seidov, D., T. P. Boyer, R. A. Locarnini, A. V. Mishonov, and H. E. Garcia (2010), *World Ocean Atlas 2009 Volume 2: Salinity*, p. 184 ff., NOAA Atlas NESDIS 69, U.S. Government Printing Office, Washington, D.C., USA
- Serra, N., R. H. Käse, A. Köhl, D. Stammer, and D. Quadfasel (2010), On the low-frequency phase relation between the Denmark Strait and the Faroe-Bank Channel overflows, *Tellus A*, *62*(4), 530–550, doi:10.1111/j.1600-0870.2010.00445.x.
- Shankar, D. (2004), Observational evidence for westward propagation of temperature inversions in the southeastern Arabian Sea, *Geophys. Res. Lett.*, *31*.
- SMOS-BEC Team (2014), SMOS-BEC ocean and land products description, *Tech. Rep. 1.2*, SMOS Barcelona Expert Centre, Barcelona, Spain-
- Steele, M., R. Morley, and W. Ermold (2001), Phc: A global ocean hydrography with a high quality Arctic Ocean., *J. Climate*, *14*, 2079–2087.
- Swift, C. T., and R. E. McIntosh (1983), Considerations from microwave remote sensing of ocean-surface salinity, *IEEE Trans. Geosci. Electron.*, *GE-21*(4), 480–491.
- Talley, L. D. (2002), *Salinity patterns. Encyclopedia of Global Environmental Change*, vol. 1, M. C. MacCracken and J. S. Perry, Edited by John Wiley and Sons, 11 pages.
- Talley, L. D., G. L. Pickard, W. J. Emery, and J. H. Swift (2011), *Descriptive physical oceanography, an introduction*, 6 ed., Elsevier, Boston, 560 pp.
- Talone, M. (2010), *Contribution to the Improvement of the Soil Moisture and Ocean Salinity (SMOS) Mission Sea Surface Salinity Retrieval Algorithm*, Ph.D. thesis, Universitat Politècnica de Catalunya, UPC. BarcelonaTech, Jordi Girona, 31, 08034 Barcelona, Spain.
- Tang, W., S. H. Yueh, A. G. Fore, and A. Hayashi (2014), Validation of Aquarius sea surface salinity with in situ measurements from Argo floats and moored buoys, *J. Geophys. Res.: Oceans*, doi:10.1002/2014JC010101.
- Tomczak, M., and J. S. Godfrey (2003), *Regional oceanography: an introduction*, 2 ed., Daya Publishing House, Delhi.
- Torrence, C., and G. P. Compo (1997), A practical guide to Wavelet analysis, *B. Am. Meteorol. Soc.*, 61–78.
- Trenberth, K. E., A. Dai, R. M. Rasmussen, and D. B. Parsons (2003), The Changing

- Character of Precipitation, *Bull. Amer. Meteor. Soc.*, 84(9), 1205–1217, doi:10.1175/BAMS-84-9-1205.
- Turiel, A., V. Nieves, E. Garcia-Ladona, J. Font, M.-H. Rio, and G. Larnicol (2009), The multifractal structure of satellite sea surface temperature maps can be used to obtain global maps of streamlines, *Ocean Sci.*, 5, 447–460.
- Ulaby, F., R. Moore, and F. A.K. (1986), *Microwave remote sensing: active and passive*, vol. 3, 1412 pp., Artech House, Inc., Dedham.
- Umbert, M., N. Hoareau, A. Turiel, and J. Ballabrera-Poy (2014), New blending algorithm to synergize ocean variables: The case of SMOS sea surface salinity maps, *Remote Sens. Environ.*, 146, 172–187, doi:10.1016/j.rse.2013.09.018.
- Ummenhofer, C. C., M. H. England, P. C. McIntosh, et al. (2009), What causes southeast Australia’s worst droughts?, *Geophys. Res. Lett.*, 36(L04706), doi:10.1029/2008GL036801.
- Vinayachandran, P. N., and T. Yamagata (1999), Response of the equatorial Indian Ocean to an unusual wind event during 1994, *Geophys. Res. Lett.*, 26(11), 1613–1617.
- Vinogradova, N. T., and R. M. Ponte (2013), Small-scale variability in sea surface salinity and implications for satellite-derived measurements, *J. Atmos. Ocean. Tech.*, 2689–2694, doi:10.1175/JTECH-D-13-00110.1.
- von Storch, J.-S., C. Eden, I. Fast, H. Haak, D. Hernandez-Deckers, E. Maier-Reimer, J. Marotzke, and D. Stammer (2012), An estimate of the Lorenz energy cycle for the world ocean based on the 1/10 STORM/NCEP simulation, *J. Phys. Oceanogr.*, doi:10.1175/JPO-D-12-079.1.
- Walczowski, W. (2014), *Atlantic Water in the Nordic Seas*, Edited by P. Rowinski, Springer, doi:10.1007/978-3-319-01279-7.
- Wetzel, P., H. Haak, J. Jungclaus, and E. Maier-Reimer (2007), The Max-Planck-Institute Global Ocean/Sea-Ice Model MPIOM, *Tech. rep.*, MPI for Meteorology, Hamburg, Germany.
- Wilson, E. A., A. L. Gordon, and D. Kim (2013), Observations of the Madden-Julian oscillation during Indian Ocean Dipole events, *J. Geophys. Res.: Atmospheres*, 118(6), 2588–2599, doi:10.1002/jgrd.50241.

- Wu, P., N. Christidis, and P. Stott (2013), Anthropogenic impact on Earth's hydrological cycle, *Nature Climate Change*, *3*, 807–810, doi:10.1038/nclimate1932.
- Yin, X., J. Boutin, and P. Spurgeon (2013), Biases between measured and simulated SMOS brightness temperatures over ocean: influence of sun, *IEEE J. Sel. Top. Appl.*, *6*(3), 1341–1350, doi:10.1109/JSTARS.2013.2252602.
- Yu, L. (2011), A global relationship between the ocean water cycle and near-surface salinity, *J. Geophys. Res.: Oceans*, *116*(C10), n/a–n/a, doi:10.1029/2010JC006937.
- Yu, L. (2014), Coherent evidence from Aquarius and Argo for the existence of a shallow low-salinity convergence zone beneath the Pacific ITCZ, *J. Geophys. Res.: Oceans*, *119*, 7625–7644, doi:10.1002/2014JC010030.
- Yueh, S. H. (1997), Modeling of Wind Direction Signals in polarimetric Sea Surface Brightness Temperature, *IEEE T. Geosci. Remote*, *35*, 1400–1418.
- Zhang, C. (2005), Madden-Julian oscillation, *Rev. Geophys.*, *43*(2), doi:10.1029/2004RG000158.
- Zhang, H., G. Chen, C. Qian, and H. Jiang (2013), Assessment of two SMOS sea surface salinity level 3 products against Argo upper salinity measurements, *IEEE Geosci. Remote S.*, *10*(6), 1434–1438, doi:10.1109/LGRS.2013.2259792.
- Zine, S., et al. (2008), Overview of the SMOS sea surface salinity prototype processor, *IEEE T. Geosci. Remote*, *46*(3), 621–645.

List of Figures

1.1	Hydrological cycle	2
1.2	Global salinity distribution	4
2.1	Passive remote sensing scenario	11
2.2	Visibility sample	14
2.3	TSG cruise tracks	19
2.4	Salinity along cruise track	20
3.1	SSS distribution, global	28
3.2	SSS differences, global	29
3.3	Taylor diagram, global	31
3.4	Current System, North Atlantic	33
3.5	Data availability, North Atlantic	34
3.6	Satellite-retrieved SSS distribution, North Atlantic	35
3.7	Standard deviation of SSS, North Atlantic	36
3.8	SSS differences, North Atlantic	38
3.9	SSS differences as a function of SST, North Atlantic	40
3.10	Small-scale variability, vertical gradients and sample error, North Atlantic	42
3.11	Differences between bias-corrected SMOS SSS and TSG SSS, North Atlantic	46
3.12	Monthly salinity anomalies, North Atlantic	49
3.13	Indian Ocean	53
3.14	Current System, Indian Ocean	54
3.15	SSS distribution, Indian Ocean	56
3.16	Standard deviation of SSS, Indian Ocean	58
3.17	SSS differences, Indian Ocean	60
3.18	SSS differences as a function of the distance to coast, Indian Ocean	61
3.19	Taylor diagram for the annual cycle, Indian Ocean	62

4.1	Annual amplitude and phase, Indian Ocean	66
4.2	Annual amplitude of E-P and current velocity, Indian Ocean	67
4.3	Percentage of total variance contained in the annual and semiannual cycle .	69
4.4	Positive and negative IOD phase	70
4.5	Dipole Mode Index	72
4.6	Standard deviation with the annual and semiannual cycle removed, Indian Ocean	73
4.7	Temporal development of box-averaged SSS anomalies	74
4.8	Month-year plot of monthly SSS anomalies	76
4.9	Average zonal SMOS SSS flux for July-September and October-December 2010, 2011 and 2012	79
4.10	Temporal development of the volume transport through lateral boundaries .	80
4.11	Horizontal distribution of the SMOS salinity budget during the N-IOD event in 2010	83
4.12	Interannual variation of box-averaged SMOS salinity budget terms	85
4.13	Atmospheric structure of the Madden-Julian Oscillation	89
4.14	High-pass filtered OLR, SSS and P anomalies for February, March and April 2012	90
4.15	High-pass filtered OLR, SSS and P anomalies for February, March and April 2013	91
4.16	Intraseasonal variation of box-averaged SSS, OLR, E,P, and wind velocity .	93
4.17	Monthly SST and wind anomaly for February, March and April 2012	94
4.18	Wavelet analysis of OLR and SMOS SSS.	96
4.19	Cross wavelet transform of OLR and SMOS SSS	97
4.20	Wavelet analysis of Aquarius SSS	98
4.21	Hovmoeller diagram of Argo salinity and temperature with MLD, ILD and BLT	100
B.1	Horizontal Distribution of E-P during IOD events	116
B.2	Variation of box-averaged SMOS salinity budget components	117

List of Tables

2.1	SMOS and Aquarius mission characteristics	18
3.1	Statistics of satellite-retrieved SSS minus TSG salinities before and after bias correction.	47
4.1	Correlation of intraseasonal OLR and P anomalies to SSS anomalies	92
B.1	Correlation coefficients of total advection	118

List of Abbreviations

BEC	Barcelona Expert Centre
BLT	Barrier Layer Thickness
ECMWF	European Centre for Medium-Range Weather Forecasts
ESA	European Space Agency
FOV	Field of View
HYCOM	HYbrid Coordinate Ocean Model
ILD	Isothermal Layer Thickness
MIRAS	Microwave Imaging Radiometer using Aperture Synthesis
MLD	Mixed Layer Depth
MLS	Mixed Layer Salinity
NASA	National Aeronautics and Space Administration
OLR	Outgoing Longwave Radiation
RFI	Radio Frequency Interference
SMOS	Soil Moisture and Ocean Salinity
SSH	Sea Surface Height
SSS	Sea Surface Salinity
SST	Sea Surface Temperature
TSG	Thermosalinograph
WOA	World Ocean Atlas

Software overview

The data analysis and visualization has been done by using Matlab scripts written by the author. The Fourier analysis was based on the Matlab library functions FFT and IFFT. The scripts used for wavelet analysis based on the Matlab code provided by C. Torrence and G. Compo (<http://paos.colorado.edu/research/wavelets>) and was modified for the thesis needs.

Text processing was carried out with LaTeX.

Acknowledgements

I am very grateful to Prof. Dr. Detlef Stammer for the supervision of my work.

I would like to thank Prof. Dr. Detlef Quadfasel for reviewing this work.

Thanks goes to the IMPRS for Maritime Affairs and the University of Hamburg for the funding of my PhD studies and the support during the last 3 years.

I would like to thank the institutions that provided the data used in this study:

I thank Detlef Quadfasel (Institut für Meereskunde, Universität Hamburg) and Katrin Latarius (Alfred Wegener Institut für Polarforschung, Bremerhaven), Allan Cembella (Alfred Wegener Institut für Polarforschung, Bremerhaven), Dagmar Kieke (Institut für Umweltphysik, Bremen) and Johannes Karstensen (GEOMAR Helmholtz Centre for Ocean Research, Kiel) for providing the thermosalinograph data obtained during cruises of the German R/V "Poseidon" and R/V "Maria S. Merian". I also wish to thank the Norwegian Marine Data Centre (NMD) at the Institute of Marine Research, Norway, for providing TSG measurements from aboard of the Norwegian R/V "Johan Hjort" and R/V "G.O. Sars".

The Argo EN4.1.1 data were provided by the Met Office Hadley Centre for Climate Change, which was supported by the Joint DECC/Defra Met Office Hadley Centre Climate Programme (GA01101) and by ERA-CLIM, a collaborative project (2011-2013) funded by the European Union under the 7th Framework Programme.

The Aquarius satellite SSS data were supplied through the NASA/CONAE Aquarius/SAC-D Project and can be downloaded from <http://podaac.jpl.nasa.gov>.

The SMOS SSS L4 product was available at <http://cp34-bec.cmima.csic.es/ocean-reprocessed-dataset>. These data were produced by the Barcelona Expert Center (<http://www.smos-bec.icm.csic.es>), a joint initiative of the Spanish Research Council (CSIC) and the Technical University of Catalonia (UPC), mainly funded by the Spanish National Program on Space.

The evaporation product were provided by the WHOI OAFlux project (<http://oaflux.who.edu>) funded by the NOAA Climate Observations and Monitoring (COM) program.

TMI data are produced by Remote Sensing Systems and sponsored by the NASA Earth Sciences Program. Data are available at www.remss.com.

WindSat data are produced by Remote Sensing Systems and sponsored by the NASA Earth Science MEaSUREs DISCOVER Project and the NASA Earth Science Physical Oceanography Program. RSS WindSat data are available at www.remss.com.

The altimeter products were produced by Ssalto/Duacs and distributed by Aviso, with support from Cnes (<http://www.aviso.altimetry.fr/duacs/>). OSCAR surface current velocities are freely available through the NOAA (www.oscar.noaa.gov).

Interpolated OLR data are provided by the NOAA/OAR/ESRL PSD, Boulder, Colorado, USA, from their Web site at <http://www.esrl.noaa.gov/psd/>

The numerical simulation was conducted at the German Climate Computing Center (DKRZ), Hamburg, Germany, in the frame of project 704.

I thank my office roommate Meike Sena Martins for the nice time we had and lots of constructive remarks.

Many thanks go to Kerstin Jochumsen, Fabian Große, Manfred Brath and my brother for proof-reading. Thank you for your helpful comments.

My heartfelt thanks go to the UniEltern e.V. I couldn't have done it without you.

My sincere thanks go to my parents, especially for their support and patience.

I want to express my deep gratitude to Alex and to our lovely son Emil for continuing support and tolerance and thank you for always covering my back!

On a final note, I would like to thank my friends for everything beyond work.

Fabian, it bears repeating: je te remercie pour les 6 dernières années. Tu es mon meilleur ami et tu as été toujours comme un frère pour moi. Je n'oublierai jamais les soirées amusantes avec les histoires de Noël de l'océanographie, Noir Désir, Pupkulies et un bon vin. Wobei, weniger Wein aber wenn, dann richtig.